DOUBLY FED INDUCTION GENERATOR WITH INTEGRATED ENERGY STORAGE SYSTEM FOR SMOOTHENING OF OUTPUT POWER

by

NISHANT SWARAJ CHOUHAN

A THESIS

Presented to the Faculty of the Graduate School of the

MISSOURI UNIVERSITY OF SCIENCE AND TECHNOLOGY

In Partial Fulfillment of the Requirements for the Degree

MASTER OF SCIENCE IN ELECTRICAL ENGINEERING

2010

Approved by

Mehdi Ferdowsi, Co-Advisor
Keith Corzine, Co-Advisor
Badrul H. Chowdhury
Mariesa L. Crow

ABSTRACT

Wind energy is one of the fastest growing renewable energies in the world today. However, integration of wind power into the power system network is still confronting many challenges. One of the main challenges is the suppression of wind power fluctuations. This thesis focuses on integration of wind power with energy storage to overcome the integration challenges. The first part of this thesis investigates the suitability of energy storage systems for transmission, distribution and wind farm applications. A review on the available energy storage systems is performed considering several criteria. Efforts are made to investigate solutions that meet all the power system requirements. In the second part of the thesis, a wind turbine generator with integrated energy storage system is modeled and studied for smoothening of the output power fluctuations due to changes in wind velocity. An ultra-capacitor is used as an energy storage system which is integrated into the doubly-fed induction generator through a bi-directional buck-boost dc-dc converter. Different modes of operation for the integrated system are studied and the simulation results verify the effectiveness of the designed model using the software package MATLAB/Simulink. The last part of the thesis focuses on application of the doubly-fed induction machine. The grid-side converter of the machine is used to supply harmonics for nearby non-linear loads. A multiple reference frame synchronous estimator and controller are used to track and eliminate the dynamically changing $6k \pm 1$ harmonics on the power system network. This complete system is developed and tested using the software package PSCAD/EMTDC. The simulation results and the harmonic analysis verify the correct operation of the system.

ACKNOWLEDGMENTS

I am heartily thankful to my advisors Dr. Mehdi Ferdowsi and Dr. Keith Corzine for all their support and invaluable guidance. This thesis would not have been possible without their patience and belief they have shown in me.

I also would like to thank Dr. Badrul Chowdhury and Dr. Mariesa L. Crow for serving on my graduate committee. I am grateful to all my friends and power group who have made my stay in Rolla a pleasant one.

Finally, I would like to dedicate this thesis to my loving parents and affectionate brother, who have always been great source of inspiration and encouragement for higher education.

TABLE OF CONTENTS

LIST OF ILLUSTRATIONS

Page

LIST OF TABLES

NOMENCLATURE

Symbol	Description
i_{abcs}	Stator side currents
i_{abcr}	Rotor side currents
λ_{abcs}	Stator side flux
λ_{abcr}	Rotor side flux
v_{abcs}	Stator side voltage
v_{abcr}	Rotor side voltage
r_s and r_r	Internal resistance of stator and rotor respectively
N_s and N_r	Stator and Rotor equivalent turns
$\mathbf{L}_s$ and $\mathbf{L}_r$	Stator and Rotor inductances respectively
L_{ls} and L_{ms}	Stator leakage and magnetizing inductance
L_{lr} and L_{mr}	Rotor leakage and magnetizing inductance
L_{sr}	Mutual inductance between stator and rotor
θ_r	Rotor position
T_e	Electromagnetic torque
J	Inertia of the rotor and connected load
P	No. of poles
p	derivative, $\frac{d}{dt}$
T_L	Load torque
ω_r	Rotor angular velocity
v_{qd0s}	Stator side q-and d-axis voltage
v'_{qd0r}	Rotor side q-and d-axis voltages referred to stator side
i_{qd0s}	Stator side q-and d-axis current
i'_{qd0r}	Rotor side q-and d-axis currents referred to stator side
λ_{abcs}	Stator side flux linkage
λ'_{abcr}	Rotor side flux linkage referred to stator side
ψ_{qd0s}	Stator side flux linkages per second

ψ'_{qd0r}	Rotor side flux linkages per second referred to stator side
ω_b	Base electrical angular frequency
P	Real power
Q	Reactive power
P_s & Q_s	Stator real and reactive power
P_r & Q_r	Rotor real and reactive power
P_g & Q_g	Total real and reactive power
i_{dcr}	DC current injected into RSC
i_{dcu}	DC current injected into GSC
i_{abcu}	GSC currents entering into grid
i_{dca}	Charging/discharging current of energy storage system
C	dc link capacitor
β	Arbitrary angle ($\theta - \theta_r$)
R	Rotor resistance
V_{dc}	dc link voltage
L_u	Utility side inductor
V_s	Line to neutral voltage of the grid
ρ	Air density
R	Radius of the wind turbine blade
v_{wind}	Wind velocity
C_p	Performance coefficient of wind turbine
λ	Tip speed ratio
β	Blade pitch angle
V_{UC}	UC voltage
P_{UC}	Charging/discharging power of UC
i_L	Non-linear load current
G_e & G_c	Integral gain for estimator and controller respectively

1. INTRODUCTION

1.1. INTRODUCTION

A recent report by the World Wind Energy Association (WWEA) shows the total growth of the wind power around the globe. It is seen that installed wind capacity is doubling every three years [1]. Figure 1.1 illustrates the exponential growth in the total wind power installation around the globe in the last ten years.

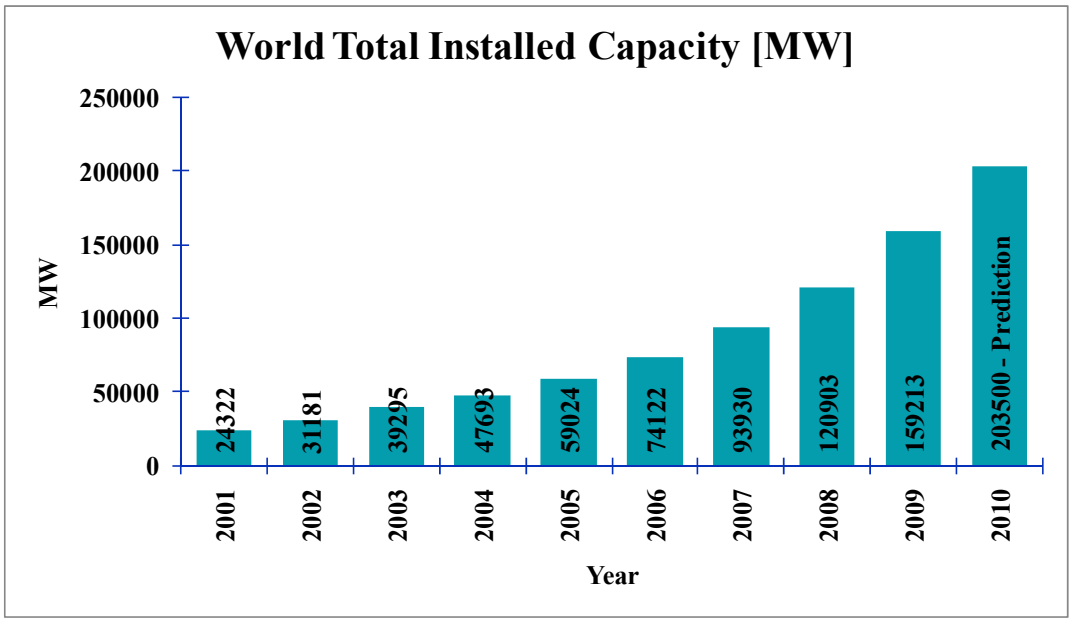

Figure 1.1. Growth of wind power installation in the last ten years [1].

The United States alone has added 9.92 Gigawatts (GWs) in 2009 making its total installation 35.16 GWs at the end of the year. This accounts for 1.9% of the electricity generated in the United States as compared to 1.3% in 2008. At recent penetration levels of 1% - 2%, the regulation of the irregular stream of wind power does not seem to be necessary. According to the U.S. Department of Energy, it is feasible for wind energy to

make up 20% of U.S. electricity needs by year 2030 [2]. With the pace at which wind farms and wind industries are growing it is possible that a 20% wind scenario will be achieved much earlier than the expected time. At such high penetration levels, it is required by the wind turbines/farms to participate in grid frequency regulation, unit commitment, or to supply a constant amount of active power as required by grid operators.

It is becoming important to regulate the output power of the wind turbine generators (WTG's) with respect to changes in the wind speed. The four main types of wind turbine generators available in the market are illustrated in Figure 1.2 [3].

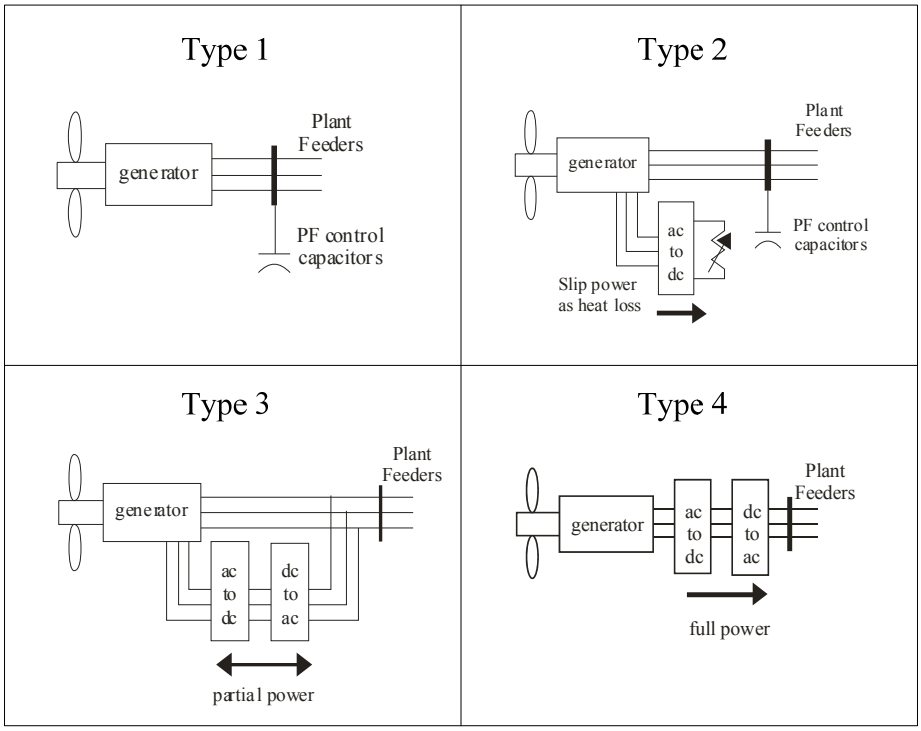

Figure 1.2. Type of wind turbine generators.

Type 1 and 2 are the simplest topology in which the turbine is directly connected to the grid. This type of machine needs a switch to prevent motoring operation during low wind speeds and also suffers a major drawback of reactive power consumption as there is no reactive power control. Type 2 uses an electronically modulated rotor resistance to affect dynamic changes in the machine torque speed characteristics. Type 4 uses a full rated converter with either a synchronous or an asynchronous machine. This type of topology has full control of the reactive power and speed. Type 3 is the most common for high power applications (1.5 MWs and above). For this purpose a doubly-fed induction generator (DFIG) wind turbines are considered in this thesis.

The schematic for DFIG is illustrated in Figure 1.3 [4]. Here the total output grid power (P_g & Q_g) is the summation of stator power (P_s & Q_s) and rotor power (P_r & Q_r) since no energy is being stored in the dc-link capacitor. The prime purpose of the dc-link is to maintain the constant voltage.

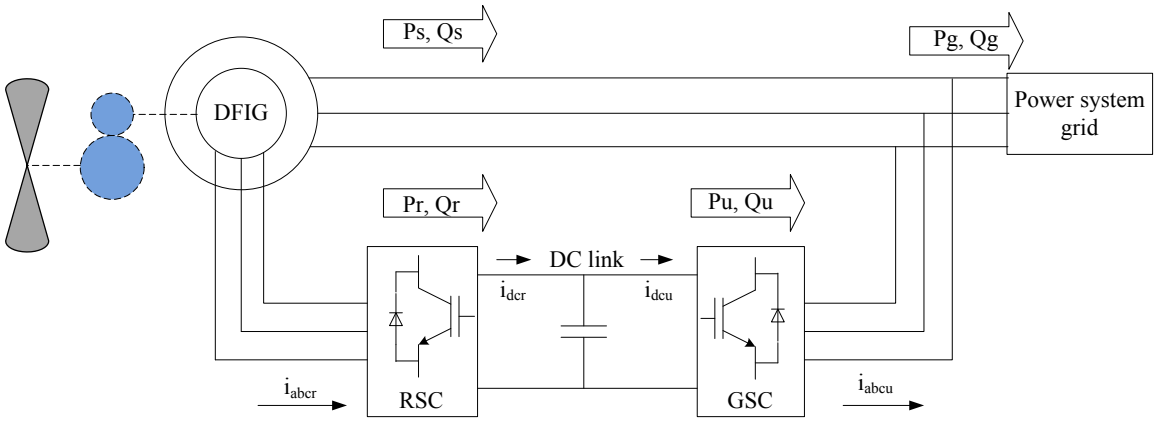

Figure 1.3. Doubly-fed induction generator system diagram.

DFIG are getting more and more popular for high power applications due to their inherent advantages such as [4]:

- ✓ complete control of the reactive power using rotor side converter (RSC) and the grid side converter (GSC);
- ✓ rotor speed can vary ±33% from the synchronous speed of the machine;
- ✓ the converters for this topology need to be rated, at most, around 25% to 30% for supplying slip power to the machine. This reduces the size of power electronic switches as well as the losses in the converter; and
- ✓ four quadrant active and reactive power flow capabilities with constant frequency.

One major concern associated with the wind energy is its inherent intermittent nature. With the increase in the penetration of the wind energy into the power system, it is of utmost importance that fluctuations in the wind speed are not reflected in the output power of the WTG's. A sudden reduction in the wind speed can cause the output power of the wind farms decrease quickly; not leaving enough time for the power system to react. Also, large variations in wind speed can cause the output power to fluctuate which may result in voltage and frequency regulation issues.

Energy storage can be helpful in dealing with the issues of intermittent nature of renewable generation.

1.2. REVIEW OF ENERGY STORAGE SYSTEMS (ESS)

Exhausting natural resources, continuously increasing energy demand, and aging transmission networks are the major problems that the power industry is facing today. Renewable energy sources such as solar and wind power cannot be integrated directly to the grid due to their inherent intermittent nature. Increasing the penetration of distributed generation (DG) in the power system network not only reduces the overall reliability but also increases the complexity of the system. Using renewable generation in combination with storage systems is one way to tackle voltage and frequency regulation issues. Energy storage devices are required in the power system network to:

- ✓ integrate renewable sources with the power system by converting them into a smoother and dispatchable format;
- ✓ provide ride through capability when the distributed generation fails to supply required energy; and

- ✓ manage the amount of power required to supply during peak power demand by storing it during off-peak hours.

Significant research is being done in this area but every ESS has some limitation which makes it suitable for particular application only.

A storage system also provides other advantages such as prompt start up, modularity (easy plug-in), no site restrictions, limited environmental impacts and flexibility when used for power system application. These benefits depend on the type of the storage system under consideration. For this reason it is important to compare all the storage systems in general against the requirements of the power system.

1.3. LITERATURE REVIEW

The existing literature on DFIG with integrated energy storage systems are studied in this section along with the literature focusing on use of DFIG for power conditioning. It is difficult to find literature in this area's since more attention is given to fault ride-through capabilities of the DFIG. A few papers in this area are described subsequently. The most common suggested topology for integrated energy storage system is illustrated in Figure 1.4. In this topology the energy storage system (battery, ultra-capacitor, etc.) is connected in parallel with the existing dc link through a bi-directional dc-dc converter.

Liyan Qu and Wei Qiao [5] propose a scheme in which supercapacitor energy storage is connected in parallel with the DC link of DFIG through bidirectional dc-dc converter. The control for this scheme is designed such that energy storage will supply power during sub-synchronous speeds and will charge during super-synchronous speeds.

Zhenhua Jiang and Xunwei Yu [6] propose a similar scheme except the supercapacitor is replaced by a battery energy storage system. The objective of the battery converter system is to maintain a constant voltage at the DC link, so the ripple in the capacitor voltage is less. Also, the stator side converter can be used to command definite amounts of real and reactive power to the grid.

Aktarujjaman, Haque, Muttaqi, Negnevitsky and Ledwich [7] also suggest a similar scheme with battery energy storage system but the primary purpose of the storage system is to have a smooth transition from one mode of operation to another.

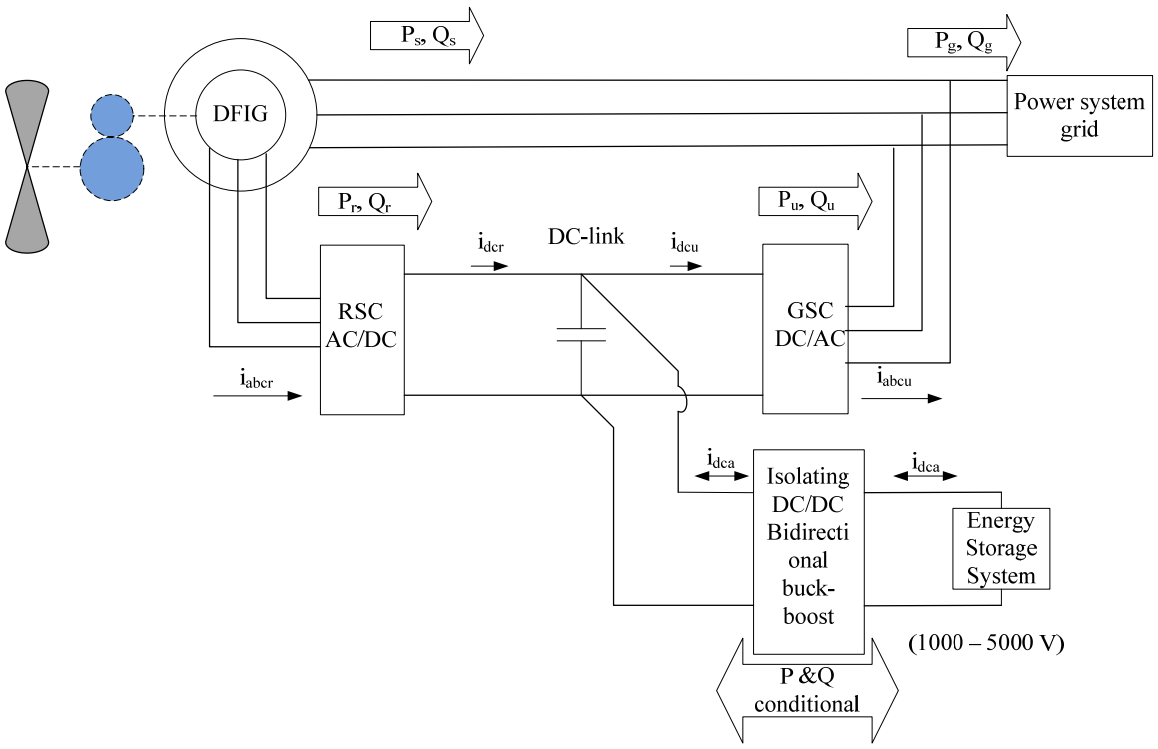

Figure 1.4. DFIG with integrated ESS in parallel with the dc link.

Haihua Liu, Hongzhong Ma, Lin chen, Guanghe Li, Tongkuang Liu and Feng Zhao [8] propose a scheme in which a fuel cell is directly connected in parallel with the DC link capacitor. And then RSC as well as GSC are used to control the real and reactive power independently.

Marinelli, Morini and Silvestro [9] are suggesting a scheme to integrate DFIG and a Lithium Ion energy storage system. But they have not yet integrated both for improving the overall performance.

Abolhassani, Niazi, Toliyat and Enjeti [10] for the first time proposed the idea of using DFIG wind turbine generator for harmonic compensation on the power system grid. They suggested using the RSC of the DFIG for harmonic compensation as well as real and reactive power supply through the stator.

Tremblay, Chandra and Lagace [11] are using the GSC to inject the harmonics required by non-linear loads. The controls for injecting harmonics through the GSC involves low pass filter to eliminate fundamental component from grid current and command all the required harmonics by the non-linear load.

Gaillard, Poure and Saadate [12] are proposing a scheme similar to the previous literature except they have a self tuning filter to extract the fundamental component from the grid currents and inject the harmonics using the RSC.

However, the authors do not discuss the long term consequences on the generator when RSC is used for injecting high frequency harmonics on the stator and rotor side. Also they do not take into account that the harmonics of interest are only $6k\pm1$[13], use of the proposed methods increases the filtering impact on the DFIG.

1.4. THESIS OUTLINE

This section deals with the existing wind turbine generator technologies and how energy storage can help integrating renewable generation such as solar and wind power to the power system grid. After discussing the need for energy storage a brief literature review is done on paper's suggesting integration of WTG's with energy storage as well as on harmonic elimination using a DFIG.

Section two is a complete review on energy storage technologies and their applications in power system. Various storage technologies are discussed in detail and their suitability is evaluated against different fault scenarios on power system. Finally, these technologies are categorized depending upon their characteristics to mitigate different kinds of faults on the power system.

The equations describing the doubly-fed induction machine are described in section three. This section shows complete modeling, operation as well as simulation of the DFIG. The various simulation results are shown to verify the correct operation of the developed models. It describes the average value model developed using software package Matlab/Simulink.

The section four describes the strategy for implementing energy storage in a DFIG. Ultra capacitor (UC) energy storage is used to absorb the energy of wind gusts. An ultra-capacitor and a bidirectional dc-dc converter are placed in between the dc link

capacitor and the rotor-side converter. This enables the independent control of voltages and currents on the rotor side as well as the grid side. Different control strategies are discussed, compared and implemented. Simulation results are compared to those with the conventional DFIG to show the difference. Thus a complete DFIG with integrated energy storage is simulated and verified using software package Matlab/Simulink. Finally it is compared with the topologies suggested by other authors.

Section five introduces a new technique of eliminating harmonics on the power system network with the help of GSC in DFIG. Multiple reference frame synchronous estimator (MRFSE) is used to analyze the system harmonic and feedback integral controller is used to eliminate the dynamic harmonics due to non-linear loads on the system. The entire model is developed using software package PSCAD/EMTDC. The simulation results verify the correct operation of the DFIG as active filter as well as source of real and reactive power.

Finally section six contains the conclusion and the summary of the work done along with the future scope. The appendix presents the loss model developed to compare the performance of the proposed scheme.

1.5. SUMMARY

Wind power as one of the major source of generation seems to be promising. Still, there are some uncertainties associated with wind power such as its intermittent nature of generation. Energy storage can be used to mitigate the problems associated with the fluctuating output power of the wind turbines due to changing wind speed. Integrating an energy storage system within a wind turbine generator system seems to be more practical solution. The available literature in this area is studied. Various energy storage technologies reviewed in section two helps in selecting the optimal storage technology suited for this application.

2. REVIEW OF ENERGY STORAGE SYSTEMS

2.1. INTRODUCTION

Storage systems such as batteries (BESS), flywheels (FES), compressed air (CAES), pumped hydro (PHS), ultra capacitors (UC), super magnetic energy storage (SMES), hydrogen etc. store energy in different forms like electrochemical, kinetic, pressure, potential, electromagnetic, chemical, and thermal [14-17][34].

The following characteristics are considered here for the review of energy storage systems:

- ✓ specific power
- ✓ specific energy
- ✓ response time (maximum ramp up/down time)
- ✓ storage capacity
- ✓ efficiency
- ✓ self discharge rate
- ✓ back up time
- ✓ maturity of technology
- ✓ environmental effects
- ✓ site/location constraints
- ✓ capital/operating cost
- ✓ life time / charging cycles
- ✓ sensitivity to heat/charge-discharge rate
- ✓ maintenance

Based on the analysis the classification of the energy storage system is done to suit the specific power system application.

2.2. ESS REQUIREMENTS

Storage requirements for transmission and distribution can be broadly classified into four categories which include gird stabilization, operational support, power quality, and load shifting [32]. These can be further classified into the following subcategories:

Angular Stability: Sudden change in large load or fault causes the rotor of generator to lose synchronism resulting into electromechanical oscillations. Such oscillations may involve number of generators separated geographically and may appear when system loading is increased over a weak transmission line. If such oscillations are not damped (short term – within seconds) it may result into tripping of one or more generators off the line which may further result into overloading of the other transmission equipments/networks and potential system instability.

Voltage Stability: Voltage instability occurs when demand for reactive power exceeds the available sources in the network, under such a condition any increase in the load is accompanied by drastic voltage drop.

Frequency Excursion Suppression: Frequency excursion occurs when there is significant mismatch in load and generation. In large interconnected power system this type of situation is associated with islanding. Generally problem associated to frequency are due to inadequate equipment response, poor coordination of control and protection and insufficient generation reserve. Frequency excursions may be impacted by fast (short term – few seconds) as well as slow (long term – several minutes) dynamics.

Regulation Control: Under normal operating condition regulation ensures that control area is able to balance generation and load. Regulation is use of online generation or storage that is equipped with Automatic Generation Control (AGC) that can track the instantaneous changes in load and correct the unintended fluctuation in generation.

Conventional Spinning Reserve: Whenever there is a sudden unexpected loss of generator or transmission line contingency, spinning (supplemental/replacement) reserve helps to restore the generation-load balance. In such situation the system frequency suddenly drops and there is no time to react. Frequency sensitive generator governor senses the drop and responds immediately; also these reserves help to get frequency back to 60 *Hz*.

Power Quality (PQ): It is the momentary black out that occur due to either faults (short-term PQ), or due to equipment failures, natural disaster, weather etc (long-term PQ).

Load shifting: Load shifting is storing energy during periods of low demand and supplying it when needed. In this way a portion of customer load is shifted from periods

of high demand to periods of low demand. Therefore, the utility equipment is more uniformly loaded. Load shifting can be done from a few minutes (short-term) to several hours (long-term).

Table 2.1 describes the ESS requirements for the power system network in general.

Table 2.1. Storage requirements for power system [32].

Application / Parameters		Power MW	Voltage KV	Power Discharge Duration	Energy Discharge per Event	Energy Discharge Duty Cycle	System Response time
Grid Stabilization	[A] Angular Stability	10 - 500	4.2 - 750	Few sec	10 MJ – 1 GJ	10 event/yr, 1 event/day, 20 cycle/event	< 20 msec
	[B] Voltage Stability	10- 500	4.2 – 750	Few sec	5 MJ – 30 GJ	10 event/yr, 1 event/day	< 20 msec
	[C] Frequency Excursion Suppression	10 - 500	4.2 – 750	10 – 30 min	0.2 – 25 MWh	10 event/yr, 1 event/day	< 20 msec
Grid Operation Support	[D] Regulation Control	2 - 200	4.2 – 115	3 – 30 min	0.1 – 25 MWh	2 cycles/hr	< 10 min
	[E] Conventional Spinning Reserve	2 - 200	4.2 – 115	2 hrs	2 – 100 MWh	10 event/yr, 1 event/day	< 10 min
Distribution Power Quality	[F] Short Duration PQ	1 - 50	4.2 – 34.5	secs	2 MJ – 3 GJ	100 events/yr, 5 events/day, 1 event/hr	< 20 msec
	[G] Long Duration PQ	1 - 50	4.2 – 34.5	hrs	1 – 400 MWh	1 event/yr	< 20 msec
Load Shifting	[H] Short Duration LS	1 - 200	4.2 – 115	1 – 4 hrs	1 – 200 MWh	50 events/yr, 1 event/day	< 10 min
	[I] Long Duration LS	1 - 200	4.2 – 115	5 – 12 hrs	5 – 600 MWh	250 events/yr, 1 event/day	< 10 min

In addition to the above, the following requirements are more specific to wind power generation:

Transmission Curtailment: There may be a situation that generation by the wind farms is more than the transmission capacity and the farms are located far from the load centers. The mitigation of constraints imposed by insufficient transmission capacity on the utilization of wind generation requires that energy should be stored during periods of insufficient transmission capacity and discharge when capacity becomes available.

Time Shifting: This is similar to load shifting i.e. to store energy when not required and use when needed the most.

Forecast Hedge: When wind generation forecast fails, one can use the stored energy to mitigate the penalties incurred when real-time generation falls short of the amount of generation bid for delivery.

Grid Frequency Support: This is similar to Frequency Excursion i.e. in systems where high fraction of generation is provided by wind, a sudden reduction in wind can cause a disturbance leading to significant imbalance between load and generation.

Fluctuation Suppression: Output from wind farm fluctuates due to fluctuations in the wind velocity. Energy storage systems can be used to stabilize wind farm generation frequency by absorbing and discharging energy counter to high cycle variations in output.

The Table 2.2 describes the ESS requirements for renewable energy systems such as solar or wind.

Table 2.2. Storage requirements for renewable [32].

Application / Parameters		Power MW	Voltage KV	Power Discharge Duration	Discharge Per Event	Discharge Duty Cycle	System Response Time
Wind Generation Support	[J] Transmission Curtailment	2 – 200	4.2 – 34.5	5 – 12 hrs (except CAES) Varies by ES technology	50 – 120 MWh Varies as per ES tech.	Per reference wind profile Optimized for each technology	< 1 min
	[K] Time Shifting	2 – 200	4.2 – 34.5				< 1 min
	[L] Forecast Hedge	2 – 200	4.2 – 34.5				< 20 msec
	[M] Grid Frequency Support	2 – 200	4.2 – 34.5	10 – 30 min	0.2 – 25 MWh	24 events/yr, 1event/day	< 20 msec
	[N] Fluctuation Suppression	2 - 50	4.2 – 34.5	Few secs	10 – 200 MJ	90 cycles/yr, continuous charge and discharge	< 20 msec

Table 2.3 compares all the ESS features/characteristics with the requirements for power system or requirements for renewable energy system. This features/characteristics are summarized in Figure 2.1 which provides better idea for ESS selection.

Table 2.3. Energy storage characteristics [18-21][32]

ESS / Parameters	Battery (BESS)							Flywheel Storage (FES)	Compressed Air Storage (CAES)	Pumped Hydro Storage (PHS)	Super/Ultra Capacitor (UC)	Superconducting Magnetic Energy Storage (SMES)	Hydrogen based Energy Storage - *depends on fuel cell ratings
	$PbSO_4$	Nickel	NaS	Redox	Poly-sulphide	LI-Ion	Metal-Air						
Power Capacity (MW)	50							20	300	1000	3	50	0.05 - 1
Specific Energy (kJ/kg)	350 - 700							450	100	1	19.87	2.78	1600
Start Up/Response time	20 msec							msec	10 -12 min	10 -12 min	msec	msec	-
Storage Capacity (MWh)	60							10 - 15	2500	8000	0.15	0.003	-
Efficiency	60 - 90 %							85 - 95 %	70 - 85 %	70 - 85 %	90 - 95 %	95%	30 - 50 %
Self Discharge Rate	very low							high	very low	low	low (10%/day)	high	low
Back Up time	hours							mins	hours	hours	secs	sec - mins	depends on fuel
Maturity (decade)	2 – 10							4 - 5	3	10 - 12	2	3 - 4	-
Environmental Effects	medium							low	medium	high	Low	high	-
Site requirements	no							no	yes	yes	no	no	no
Capital / Operating Cost	medium							high	high/low	high/low	high/low	high	high
Life time/Cycle (Yrs)	10 - 15 (depends on DOD)							12 - 20	< 50	50	10 – 12	20 - 30	10 - 12
Sensitivity (Heat & Charging/Discharging Rate)	yes - highly							no	medium	no	No	no	medium
Maintenance	high							high	high	low	Low	low - nil	medium
Conventional compatibility	C, D, E, H, I							A,B,F	D, E, H, I	D, E, H, I	A, B, F	A, B, F	
Wind compatibility	J, K, M							N			N	N	

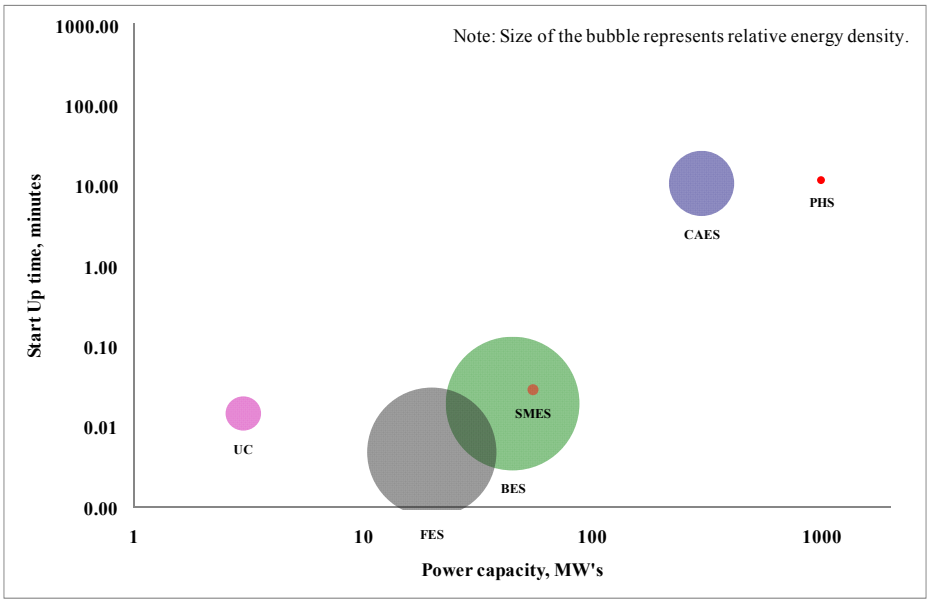

Figure 2.1. Start-up time vs. storage capacity.

2.3. ANALYSIS

To know whether certain technology is suited for certain application, the characteristics of technology should be compared with the requirements of the application. Table 2.3 also checks the suitability for each power system requirement. Table 2.4 shows a summary of the suitability check.

Table 2.4. Summary of suitability check

ESS / Requirements	BESS	FES	CAES	PHS	UC	SMES	BESS + FES
A		√			√	√	√
B		√			√	√	√
C	√						√
D	√		√	√			√
E	√		√	√			√
F		√			√	√	√
G							
H	√		√	√			√
I	√		√	√			√
J	√						√
K	√						√
L							
M	√						√
N		√			√	√	√

From suitability check it is clearly evident that no single storage system is able to suffice all the requirements of power system. So one can only use specific storage for certain applications only.

This review leads to the fact that if one wants storage to suffice all the requirements of power system it has to have the characteristic of two or more storage systems [22-25]. For instance, flywheel and battery can be a good combination to supply power for short response time as well as long back up time [35]. Both of them have

complimentary advantages and so they can form good combination to serve the purpose. Such storage systems can be selected from the review depending on the availability to form a hybrid storage system.

2.4. SUMMARY

In this section ESS requirement of power system and renewable energy systems are listed. The characteristics of different energy storage are listed and compared with the requirements of the power system and renewable system. The suitability check is done for various energy storage technologies. Finally it can be summarized that no single energy storage technology can suffice all the requirements of power system or renewable energy system. A combination of two or more energy storage systems with complementary features can be a possible solution. Section 2 and Section 3 of this thesis focuses on integration of an ultra-capacitor energy storage system with the wind turbine generator (flywheel) system with the help of power electronic converters. The simulation results verify the successful working of the integrated system.

3. DEVELOPMENT AND VALIDATION OF AN AVERAGE VALUE MODEL FOR A DFIG

3.1. MATHEMATICAL REPRESENTATION OF INDUCTION MACHINE

Induction machines are used in a wide variety of applications in industry for converting electrical energy into mechanical and vice versa. The winding arrangement for a 2-pole, 3-phase wye-connected wound rotor induction machine is illustrated in Figure 3.1 [26].

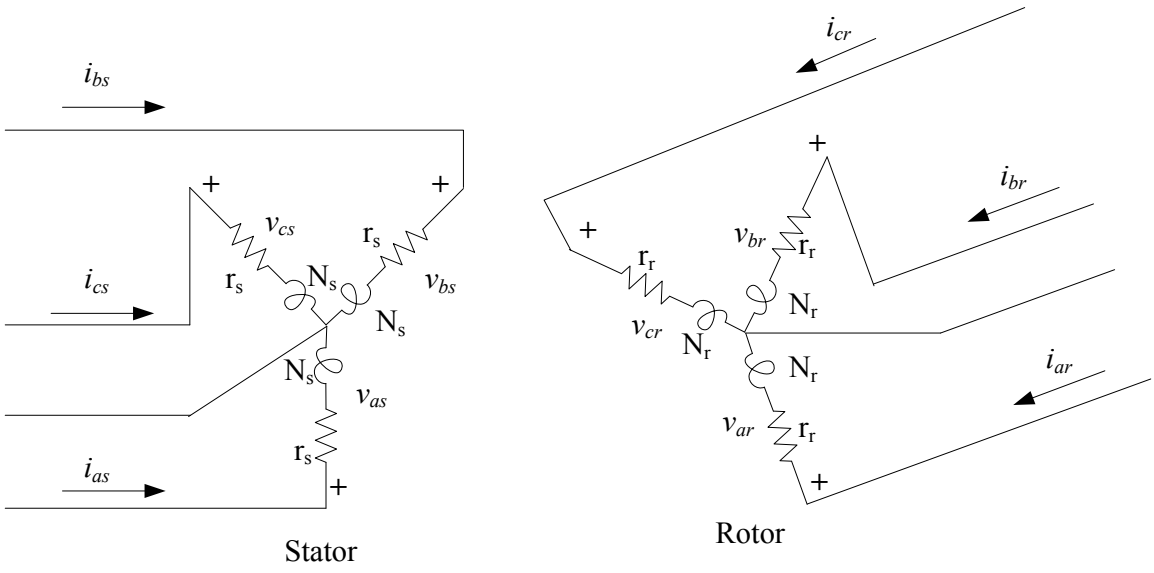

Figure 3.1. Winding diagram of a 2-pole, 3-phase, wye-connected symmetrical induction machine.

3.1.1. Stator and Rotor Equations in abc Variables. The stator windings are identical, sinusoidally distributed windings, displaced 120°, with N_s equivalent turns and internal resistance of r_s. Similarly, the rotor windings are also sinusoidally distributed windings, displaced 120° with N_r equivalent turns and internal resistance r_r. Voltage equations in machine variables can be written as,

$$v_{abcs} = r_s i_{abcs} + \frac{d\lambda_{abcs}}{dt} \tag{1}$$

$$v_{abcr} = r_r i_{abcr} + \frac{d\lambda_{abcr}}{dt} \tag{2}$$

where,

$$(f_{abcs})^T = [f_{as}\ f_{bs}\ f_{cs}] \tag{3}$$

$$(f_{abcr})^T = [f_{ar}\ f_{br}\ f_{cr}] \tag{4}$$

In the above equations, f can represent either voltage, current, flux linkage, or electric charge. Here subscript s and r denote variables and parameters associated with the stator and rotor circuits respectively. For magnetically linear system, the flux linkages may be expressed as,

$$\begin{bmatrix} \lambda_{abcs} \\ \lambda_{abcr} \end{bmatrix} = \begin{bmatrix} \mathbf{L}_s & \mathbf{L}_{sr} \\ (\mathbf{L}_{sr})^T & \mathbf{L}_r \end{bmatrix} \begin{bmatrix} i_{abcs} \\ i_{abcr} \end{bmatrix} \tag{5}$$

where the winding inductances are defined as,

$$\mathbf{L}_s = \begin{bmatrix} L_{ls}+L_{ms} & -\frac{1}{2}L_{ms} & -\frac{1}{2}L_{ms} \\ -\frac{1}{2}L_{ms} & L_{ls}+L_{ms} & -\frac{1}{2}L_{ms} \\ -\frac{1}{2}L_{ms} & -\frac{1}{2}L_{ms} & L_{ls}+L_{ms} \end{bmatrix} \tag{6}$$

$$\mathbf{L}_r = \begin{bmatrix} L_{lr}+L_{mr} & -\frac{1}{2}L_{mr} & -\frac{1}{2}L_{mr} \\ -\frac{1}{2}L_{mr} & L_{lr}+L_{mr} & -\frac{1}{2}L_{mr} \\ -\frac{1}{2}L_{mr} & -\frac{1}{2}L_{mr} & L_{lr}+L_{mr} \end{bmatrix} \tag{7}$$

$$\mathbf{L}_{sr} = L_{sr}\begin{bmatrix} \cos(\theta_r) & \cos\left(\theta_r+\frac{2\pi}{3}\right) & \cos\left(\theta_r-\frac{2\pi}{3}\right) \\ \cos\left(\theta_r-\frac{2\pi}{3}\right) & \cos(\theta_r) & \cos\left(\theta_r+\frac{2\pi}{3}\right) \\ \cos\left(\theta_r+\frac{2\pi}{3}\right) & \cos\left(\theta_r-\frac{2\pi}{3}\right) & \cos(\theta_r) \end{bmatrix} \tag{8}$$

In (6) and (7), L_{ls} and L_{ms} are respectively, the leakage and magnetizing inductances of the stator windings whereas L_{lr} and L_{mr} are for the rotor winding. Inductance L_{sr} is the amplitude of the mutual inductances between stator and rotor windings and θ_r is the rotor position. Referring rotor variables to stator windings by appropriate turn's ratio yields:

$i'_{abcr} = \frac{N_r}{N_s} i_{abcr}$, $v'_{abcr} = \frac{N_r}{N_s} v_{abcr}$ and $\lambda'_{abcr} = \frac{N_r}{N_s} \lambda_{abcr}$.

The magnetizing and mutual inductances are associated with the same magnetic flux path; therefore L_{ms} L_{mr} and L_{sr} are related as $L_{ms} = \frac{N_s}{N_r} L_{sr}$. Thus the mutual inductance between stator and rotor is now defined as below.

$$\mathbf{L}'_{sr} = \frac{N_s}{N_r} L_{sr} = L_{ms} \begin{bmatrix} \cos(\theta_r) & \cos\left(\theta_r + \frac{2\pi}{3}\right) & \cos\left(\theta_r - \frac{2\pi}{3}\right) \\ \cos\left(\theta_r - \frac{2\pi}{3}\right) & \cos(\theta_r) & \cos\left(\theta_r + \frac{2\pi}{3}\right) \\ \cos\left(\theta_r + \frac{2\pi}{3}\right) & \cos\left(\theta_r - \frac{2\pi}{3}\right) & \cos(\theta_r) \end{bmatrix} \tag{9}$$

The relationship between rotor and stator mutual inductance is now defined by $L_{mr} = \left(\frac{N_s}{N_r}\right)^2 L_{ms}$. So now the rotor inductance is as shown in (10).

$$\mathbf{L}'_r = \begin{bmatrix} L'_{lr} + L_{ms} & -\frac{1}{2}L_{ms} & -\frac{1}{2}L_{ms} \\ -\frac{1}{2}L_{ms} & L'_{lr} + L_{ms} & -\frac{1}{2}L_{ms} \\ -\frac{1}{2}L_{ms} & -\frac{1}{2}L_{ms} & L'_{lr} + L_{ms} \end{bmatrix} \tag{10}$$

where, $\mathbf{L}'_r = \left(\frac{N_s}{N_r}\right)^2 \mathbf{L}_r$ & $L'_{lr} = \left(\frac{N_s}{N_r}\right)^2 L_{lr}$. The flux linkages may now be expressed as,

$$\begin{bmatrix} \lambda_{abcs} \\ \lambda'_{abcr} \end{bmatrix} = \begin{bmatrix} \mathbf{L}_s & \mathbf{L}'_{sr} \\ (\mathbf{L}'_{sr})^T & \mathbf{L}_r \end{bmatrix} \begin{bmatrix} i_{abcs} \\ i'_{abcr} \end{bmatrix} \tag{11}$$

The voltage equations expressed in terms of machine variables referred to the stator windings may now be written as:

$$\begin{bmatrix} v_{abcs} \\ v'_{abcr} \end{bmatrix} = \begin{bmatrix} \mathbf{r}_s + p\mathbf{L}_s & p\mathbf{L}'_{sr} \\ p(\mathbf{L}'_{sr})^T & \mathbf{r}_r + p\mathbf{L}'_r \end{bmatrix} \begin{bmatrix} i_{abcs} \\ i'_{abcr} \end{bmatrix} \tag{12}$$

Here $r'_r = \left(\frac{N_s}{N_r}\right)^2 r_r$. The torque and rotor speed are related by the equation:

$$T_e = J\left(\frac{2}{\mathbf{P}}\right)p\omega_r + T_L \tag{13}$$

3.1.2. Equations of Transformation for Stator Circuit. The machine inductances are functions of the rotor speed, whereupon the coefficients of the differential equations (voltage equations) that describe the behavior of these machines are time-varying. A change of variables is required to reduce the complexity of these differential equations. Park's transformation is often used in induction machine analysis that eliminates all time-varying inductances by referring the stator and the rotor variables to a frame of reference that may rotate at any angular velocity or remain stationary. Applying Park's transformation to the stator circuit yields:

$$f_{qd0s} = \mathbf{K}_s f_{abcs} \tag{14}$$

where $(f_{qd0s})^T = [f_{qs}\ f_{ds}\ f_{0s}]$ & $(f_{abcs})^T = [f_{as}\ f_{bs}\ f_{cs}]$. Park's transformation and its inverse transformation is given by,

$$\mathbf{K}_s = \frac{2}{3}\begin{bmatrix} \cos(\theta) & \cos\left(\theta+\frac{2\pi}{3}\right) & \cos\left(\theta-\frac{2\pi}{3}\right) \\ \cos\left(\theta-\frac{2\pi}{3}\right) & \cos(\theta) & \cos\left(\theta+\frac{2\pi}{3}\right) \\ \cos\left(\theta+\frac{2\pi}{3}\right) & \cos\left(\theta-\frac{2\pi}{3}\right) & \cos(\theta) \end{bmatrix} \tag{15}$$

$$(\mathbf{K}_s)^{-1} = \begin{bmatrix} \cos(\theta) & \sin(\theta) & 1 \\ \cos\left(\theta - \frac{2\pi}{3}\right) & \sin\left(\theta - \frac{2\pi}{3}\right) & 1 \\ \cos\left(\theta + \frac{2\pi}{3}\right) & \sin\left(\theta + \frac{2\pi}{3}\right) & 1 \end{bmatrix} \tag{16}$$

where θ is an arbitrary angle. The arbitrary angular velocity ω and the angular displacement, θ are related by,

$$\theta = \int \omega.dt \tag{17}$$

3.1.3. Equation of Transformation for Rotor Circuit. Similarly applying Park's transformation to rotor circuit.

$$f'_{qd0r} = \mathbf{K}_r \, f'_{abcr} \tag{18}$$

Here $(f'_{qd0r})^T = [f'_{qr} \; f'_{dr} \; f'_{0r}]$ & $(f'_{abcr})^T = [f'_{ar} \; f'_{br} \; f'_{cr}]$. Rotor transformation is given by,

$$\mathbf{K}_r = \frac{2}{3}\begin{bmatrix} \cos\beta & \cos\left(\beta - \frac{2\pi}{3}\right) & \cos\left(\beta + \frac{2\pi}{3}\right) \\ \sin\beta & \sin\left(\beta - \frac{2\pi}{3}\right) & \sin\left(\beta + \frac{2\pi}{3}\right) \\ \frac{1}{2} & \frac{1}{2} & \frac{1}{2} \end{bmatrix} \tag{19}$$

Here the arbitrary angle is given by $\beta = \theta - \theta_r$ and the angular displacement θ_r is,

$$\omega_r = \frac{d\theta_r}{dt} \tag{20}$$

3.1.4. Stator and Rotor Equations in Reference Frame Variables. Applying Park's transformation to equation (12) yields,

$$v_{qd0s} = \mathbf{r}_s \mathbf{i}_{qd0s} + \omega\lambda_{dqs} + p\lambda_{qd0s} \tag{21}$$

$$v'_{qd0s} = \mathbf{r}'_r \mathbf{i}'_{qd0r} + (\omega - \omega_r)\lambda'_{dqr} + p\lambda'_{qd0r} \tag{22}$$

Here $(\lambda_{dqs})^T = \begin{bmatrix} \lambda_{ds} & -\lambda_{qs} & 0 \end{bmatrix}$ & $(\lambda'_{dqr})^T = \begin{bmatrix} \lambda'_{dr} & -\lambda'_{qr} & 0 \end{bmatrix}$. Flux linkage equations in qd0 variables is obtained by substituting transformation defined by equation (15) & (16) in equation (11).

$$\begin{bmatrix} \lambda_{qd0s} \\ \lambda'_{qd0r} \end{bmatrix} = \begin{bmatrix} \mathbf{K}_s \mathbf{L}_s (\mathbf{K}_s)^{-1} & \mathbf{K}_s \mathbf{L}'_{sr} (\mathbf{K}_r)^{-1} \\ \mathbf{K}_r (\mathbf{L}'_{sr})^T (\mathbf{K}_s)^{-1} & \mathbf{K}_r \mathbf{L}'_r (\mathbf{K}_r)^{-1} \end{bmatrix} \begin{bmatrix} i_{qd0s} \\ i'_{qd0r} \end{bmatrix} \tag{23}$$

Using the Park's transformation it can be shown that:

$$\mathbf{K}_s \mathbf{L}_s (\mathbf{K}_s)^{-1} = \begin{bmatrix} L_{ls} + L_M & 0 & 0 \\ 0 & L_{ls} + L_M & 0 \\ 0 & 0 & L_{ls} \end{bmatrix} \tag{24}$$

$$\mathbf{K}_r \mathbf{L}'_r (\mathbf{K}_r)^{-1} = \begin{bmatrix} L_{lr} + L_M & 0 & 0 \\ 0 & L_{lr} + L_M & 0 \\ 0 & 0 & L_{lr} \end{bmatrix} \tag{25}$$

$$\mathbf{K}_s \mathbf{L}'_{sr} (\mathbf{K}_r)^{-1} = \mathbf{K}_r \left(\mathbf{L}'_{sr}\right)^T (\mathbf{K}_r)^{-1} = \begin{bmatrix} L_M & 0 & 0 \\ 0 & L_M & 0 \\ 0 & 0 & 0 \end{bmatrix} \tag{26}$$

where,

$$L_M = \frac{3}{2} L_{ms} \tag{27}$$

Substituting (23) into (21-22) yields the voltage equations for stator and rotor in qd0 variables. Voltage equations in expanded form can be written as;

$$\left.\begin{aligned} v_{qs} &= r_s i_{qs} + \omega\lambda_{ds} + p\lambda_{qs} \\ v_{ds} &= r_s i_{ds} - \omega\lambda_{qs} + p\lambda_{ds} \\ v_{0s} &= r_s i_{0s} + p\lambda_{0s} \end{aligned}\right\} \tag{28}$$

$$\left.\begin{aligned} v'_{qr} &= r'_r i'_{qr} + (\omega - \omega_r)\lambda'_{dr} + p\lambda'_{qr} \\ v'_{dr} &= r'_r i'_{dr} - (\omega - \omega_r)\lambda'_{qr} + p\lambda'_{dr} \\ v'_{0r} &= r'_r i'_{0r} + p\lambda'_{0r} \end{aligned}\right\} \tag{29}$$

Similarly flux linkage equations in the expanded form can be written as,

$$\left.\begin{aligned} \lambda_{qs} &= L_{ls} i_{qs} + L_M (i_{qs} + i'_{qr}) \\ \lambda_{ds} &= L_{ls} i_{ds} + L_M (i_{ds} + i'_{dr}) \\ \lambda_{0s} &= L_{ls} i_{0s} \end{aligned}\right\} \tag{30}$$

$$\left.\begin{aligned} \lambda'_{qr} &= L'_{lr} i'_{qr} + L_M (i_{qs} + i'_{qr}) \\ \lambda'_{dr} &= L'_{lr} i'_{dr} + L_M (i_{ds} + i'_{dr}) \\ \lambda'_{0r} &= L'_{lr} i'_{0r} \end{aligned}\right\} \tag{31}$$

Equations (28) to (31) can be re-written in terms of flux linkages per second as,

$$\left.\begin{aligned} v_{qs} &= r_s i_{qs} + \frac{\omega}{\omega_b}\psi_{ds} + \frac{p}{\omega_b}\psi_{qs} \\ v_{ds} &= r_s i_{ds} - \frac{\omega}{\omega_b}\psi_{qs} + \frac{p}{\omega_b}\psi_{ds} \\ v_{0s} &= r_s i_{0s} + \frac{p}{\omega_b}\psi_{0s} \end{aligned}\right\} \tag{32}$$

$$\left.\begin{aligned} v'_{qr} &= r'_r i'_{qr} + \frac{(\omega-\omega_r)}{\omega_b}\psi'_{dr} + \frac{p}{\omega_b}\psi'_{qr} \\ v'_{dr} &= r'_r i'_{dr} - \frac{(\omega-\omega_r)}{\omega_b}\psi'_{qr} + \frac{p}{\omega_b}\psi'_{dr} \\ v'_{0r} &= r'_r i'_{0r} + \frac{p}{\omega_b}\psi'_{0r} \end{aligned}\right\} \tag{33}$$

$$\left.\begin{aligned} \psi_{qs} &= X_{ls} i_{qs} + X_M\left(i_{qs} + i'_{qr}\right) \\ \psi_{ds} &= X_{ls} i_{ds} + X_M\left(i_{ds} + i'_{dr}\right) \\ \psi_{0s} &= X_{ls} i_{0s} \end{aligned}\right\} \tag{34}$$

$$\left.\begin{aligned} \psi'_{qr} &= X'_{lr} i'_{qr} + X_M\left(i_{qs} + i'_{qr}\right) \\ \psi'_{dr} &= X'_{lr} i'_{dr} + X_M\left(i_{ds} + i'_{dr}\right) \\ \psi'_{0r} &= X'_{lr} i'_{0r} \end{aligned}\right\} \tag{35}$$

here ω_b is the base electrical angular velocity and Ψ is flux linkages per second.

3.1.5. Developing Equations for Computer Simulation. After solving voltage equations (32) and (33) for flux linkages per second, the following set of equations are obtained,

$$\left.\begin{aligned}
\psi_{qs} &= \int \omega_b \left[v_{qs} - \frac{\omega}{\omega_b}\psi_{ds} + \frac{r_s}{X_{ls}}\left(\psi_{mq} - \psi_{qs}\right)\right] \\
\psi_{ds} &= \int \omega_b \left[v_{ds} + \frac{\omega}{\omega_b}\psi_{qs} + \frac{r_s}{X_{ls}}\left(\psi_{md} - \psi_{ds}\right)\right] \\
\psi_{0s} &= \int \omega_b \left[v_{0s} - \frac{r_s}{X_{ls}}\psi_{0s}\right]
\end{aligned}\right\} \tag{36}$$

$$\left.\begin{aligned}
\psi'_{qr} &= \int \omega_b \left[v'_{qr} - \frac{\left(\omega - \omega_r\right)}{\omega_b}\psi'_{dr} + \frac{r'_r}{X'_{lr}}\left(\psi_{mq} - \psi'_{qr}\right)\right] \\
\psi'_{dr} &= \int \omega_b \left[v'_{dr} + \frac{\left(\omega - \omega_r\right)}{\omega_b}\psi'_{qr} + \frac{r'_r}{X'_{lr}}\left(\psi_{md} - \psi'_{dr}\right)\right] \\
\psi'_{0r} &= \int \omega_b \left[v'_{0r} - \frac{r'_r}{X'_{lr}}\psi'_{0r}\right]
\end{aligned}\right\} \tag{37}$$

here $\psi_{mq} = X_{aq}\left(\frac{\psi_{qs}}{X_{ls}} - \frac{\psi'_{qr}}{X'_{lr}}\right)$, $\psi_{md} = X_{ad}\left(\frac{\psi_{ds}}{X_{ls}} - \frac{\psi'_{dr}}{X'_{lr}}\right)$ and

$$X_{aq} = X_{ad} = X_{aqd} = \left(\frac{1}{X_M} + \frac{1}{X_{ls}} + \frac{1}{X'_{lr}}\right)^{-1}.$$

Also, solving (34-35) for current yields,

$$\left.\begin{aligned}
i_{qs} &= \frac{1}{X_{ls}}\left(\psi_{qs} - \psi_{mq}\right) \\
i_{ds} &= \frac{1}{X_{ls}}\left(\psi_{ds} - \psi_{md}\right) \\
i_{0s} &= \frac{1}{X_{ls}}\psi_{0s}
\end{aligned}\right\} \tag{38}$$

$$\left.\begin{aligned} i'_{qr} &= \frac{1}{X'_{lr}}\left(\psi'_{qr} - \psi_{mq}\right) \\ i'_{dr} &= \frac{1}{X'_{lr}}\left(\psi'_{dr} - \psi_{md}\right) \\ i'_{0r} &= \frac{1}{X'_{lr}}\psi'_{0r} \end{aligned}\right\} \tag{39}$$

here, $\psi_{mq} = X_M\left(i_{qs} - i'_{qr}\right)$ & $\psi_{md} = X_M\left(i_{ds} - i'_{dr}\right)$. The electromagnetic torque expression in qd0 variables is given by,

$$T_e = \left(\frac{3}{2}\right)\left(\frac{\mathbf{P}}{2}\right)\left(\frac{1}{\omega_b}\right)\left(\psi_{ds} i_{qs} - \psi_{qs} i_{ds}\right) \tag{40}$$

For a given load torque (T_L) the rotor speed (ω_r) can be obtained using equation (13) as,

$$\omega_r = \int \frac{\left(T_e - T_L\right).\mathbf{P}}{2.J}.dt \tag{41}$$

Also the real and reactive power in terms of reference frame variables is given by,

$$P = \left(\frac{3}{2}\right)\left(v_{qs} i_{qs} + v_{ds} i_{ds} + v_{0s} i_{0s}\right) \tag{42}$$

$$Q = \left(\frac{3}{2}\right)\left(v_{qs} i_{ds} - v_{ds} i_{qs}\right) \tag{43}$$

3.2. VALIDATION OF INDUCTION MACHINE MODEL

The 3-phase source, induction machine and converter models were developed in Matlab/Simulink software package. The parameters used for simulating DFIG are mentioned in Table 3.1 [4, 26-27].

Table 3.1. DFIG parameters [26].

hp/kW	$V_{(l\text{-}l)}$	*Poles*	T_B (N.m)	I_B (amps)	DC-link voltage	C (Farads)
2250/1678	2300	4	8.9×10^3	421.2	3700 V	1 F
r_s (Ω)	X_{ls} Ω)	X_M (Ω)	X'_{lr} (Ω)	r_r' (Ω)	J (kg.m^2)	L_u (H)
0.029	0.226	13.04	0.226	0.022	63.87	$250e^{-6}$

3.2.1. Modeling of 3-phase Source. The 3-phase source for the DFIG is modeled and then it is converted to qd0 using the inbuilt transformation in Matlab/Simulink. The schematic for the simulation as well as the simulation results are illustrated in Figure 3.2 and in Figure 3.3 respectively.

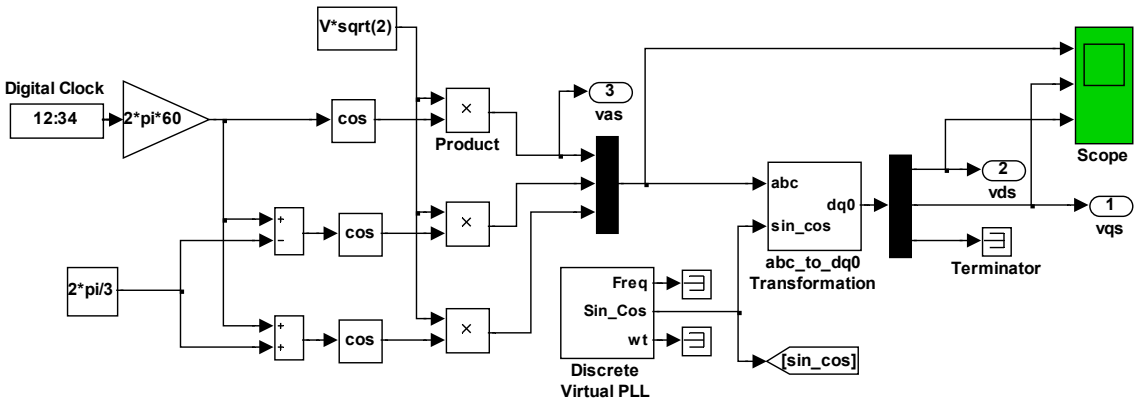

Figure 3.2. 3-phase source schematic.

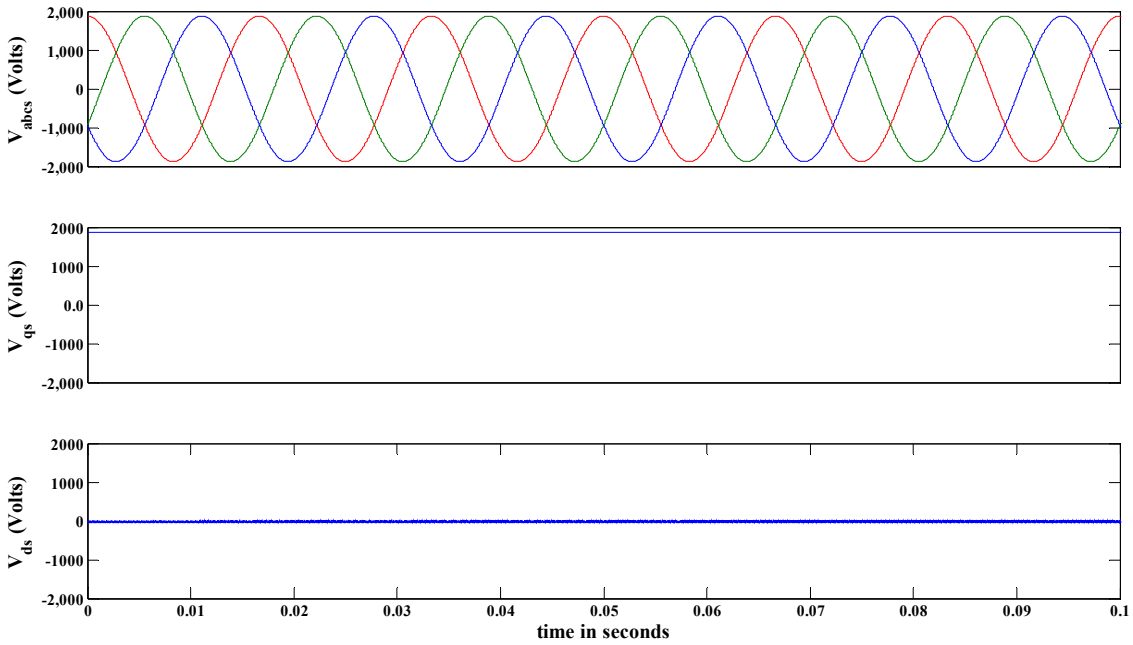

Figure 3.3. Simulation result for 3-phase source.

3.2.2. Modeling of Induction Machine. The induction machine model is developed using (36-43) as shown in Figure 3.4. The free acceleration characteristics (load torque, T_L=0) of the machine are simulated using parameters mentioned in Table 3.1. Figure 3.6 illustrates the simulation results for the machine in synchronous reference frame. During the free acceleration characteristics, the rotor accelerates from stall with zero load torque and, because friction and windage losses are not taken into account, the machine accelerates close to synchronous speed. When the rated voltage is applied during the starting of the machine, it starts consuming high current until the rated speed is reached. Figure 3.7 illustrates the torque and speed characteristics of the squirrel cage induction machine. The decaying, 60-Hz variation in the instantaneous torque is due to the transient offset in the stator currents.

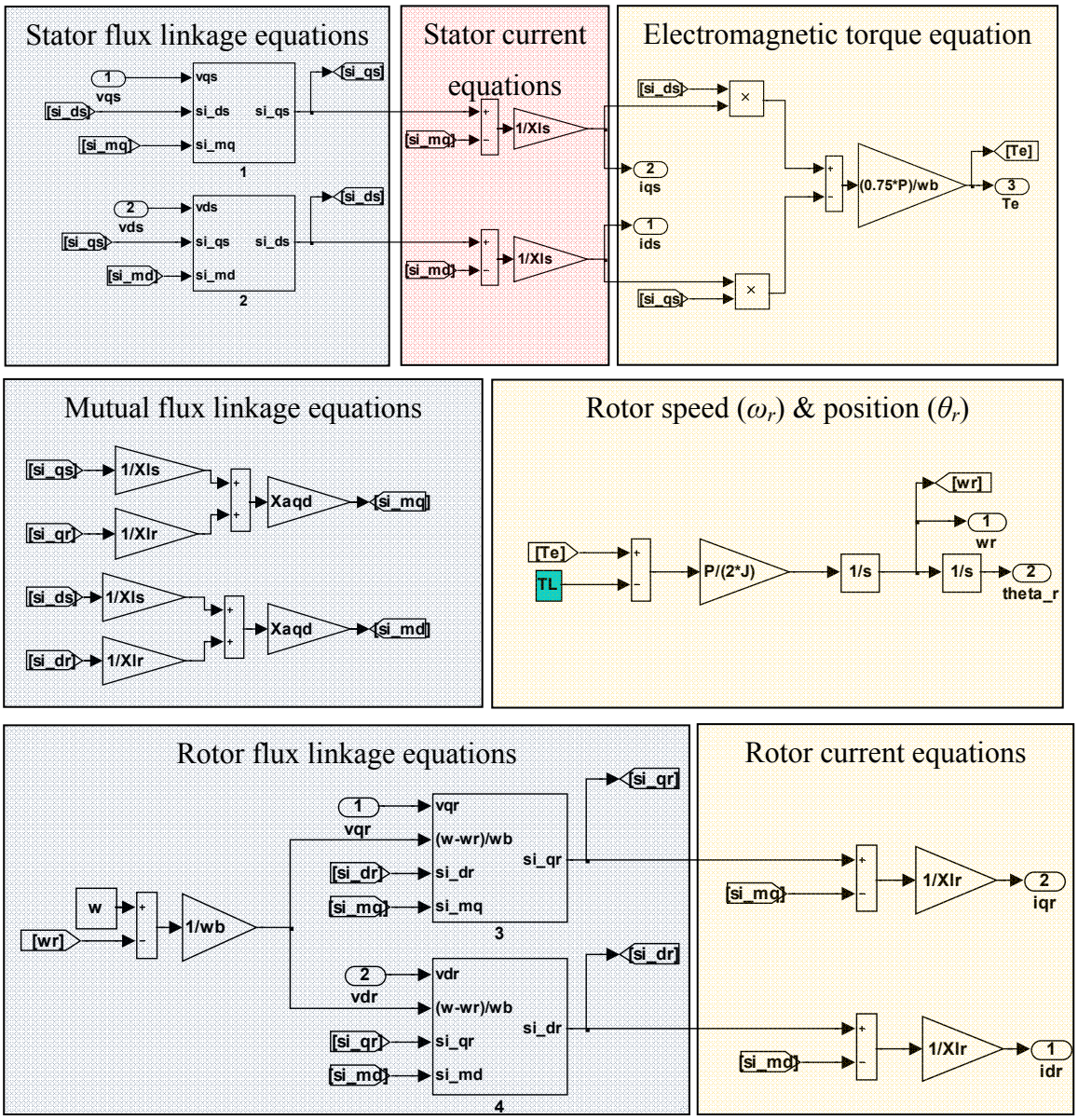

Figure 3.4. Schematic of induction machine

The complete simulation model for squirrel cage induction machine (SCIM) is illustrated in Figure 3.5.

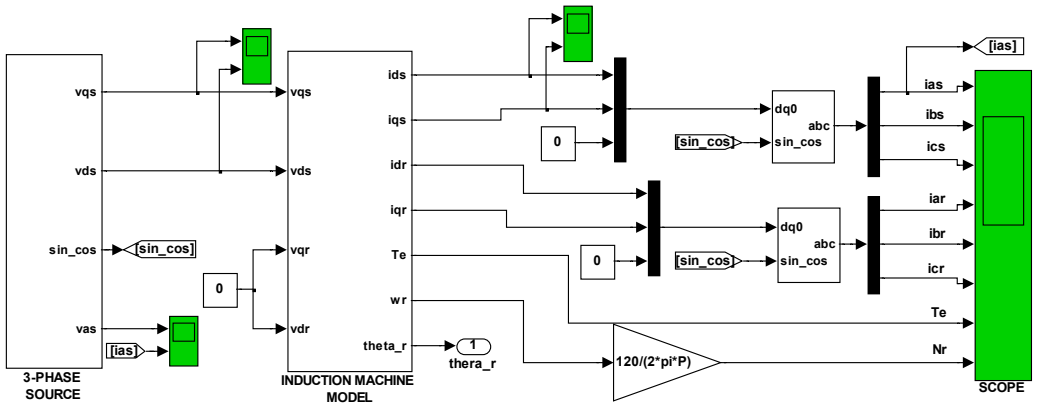

Figure 3.5. SCIM model.

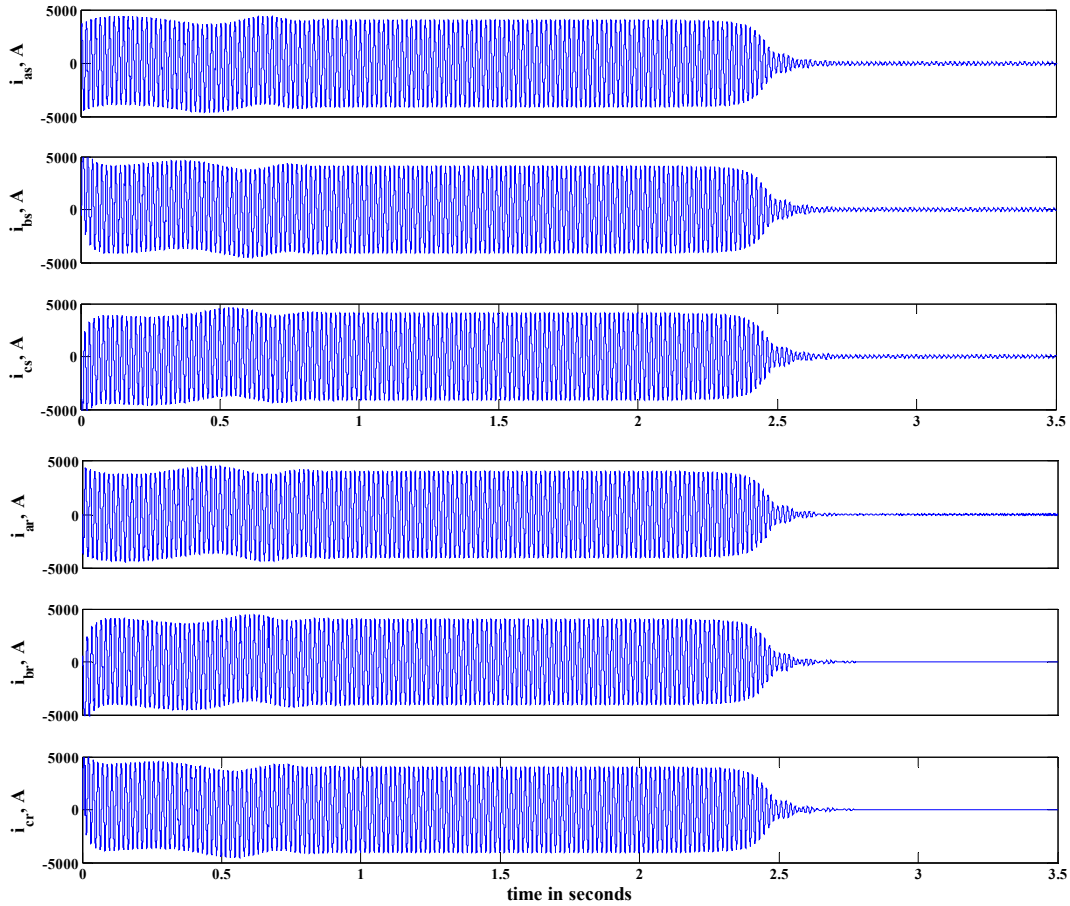

Figure 3.6. Stator and rotor currents for free acceleration characteristics.

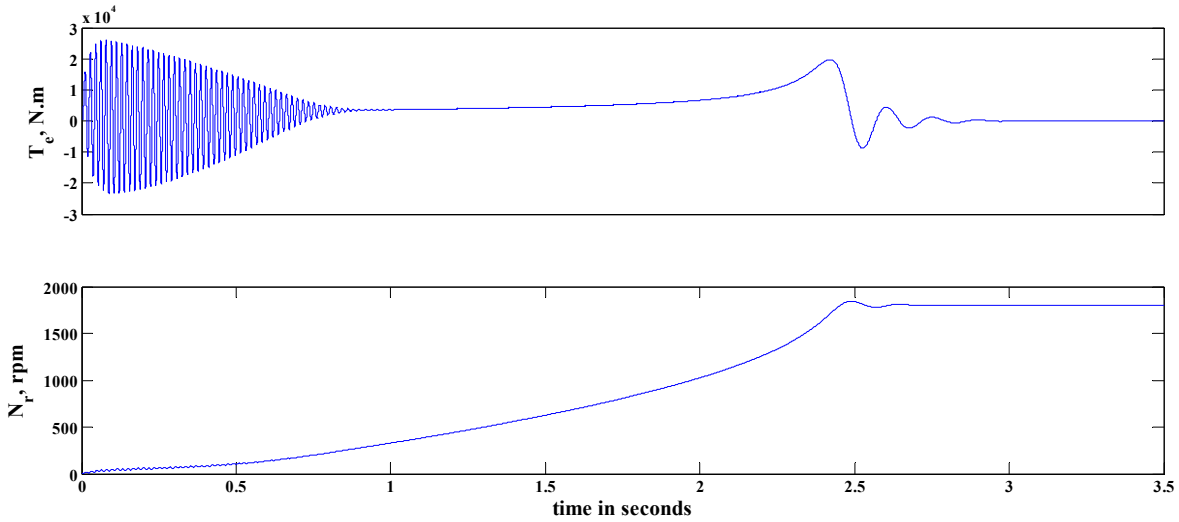

Figure 3.7. Torque and rotor speed for free acceleration characteristics.

3.2.3. Plotting Torque vs. Speed Characteristics of Induction Machine. Torque vs. speed characteristics of Induction machine are plotted by varying the resistance of the slip rings in wound rotor induction machine (WRIM) as illustrated in Figure 3.8. The simulation schematic is shown in Figure 3.9.

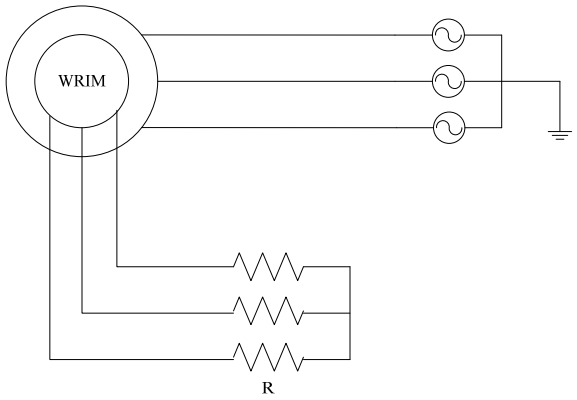

Figure 3.8. Induction machine with slip-ring rotor.

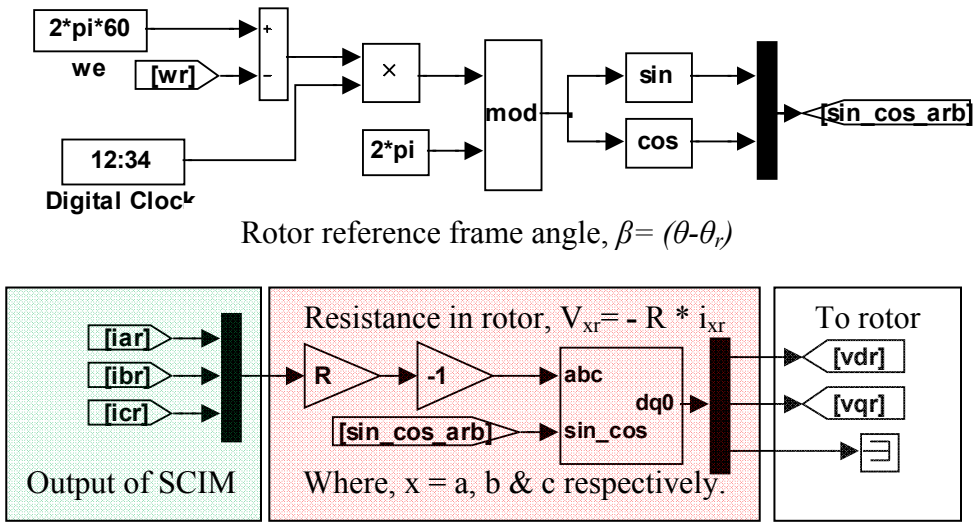

Figure 3.9. Simulation schematic for WRIM.

The simulation results illustrated in Figure 3.10 validates the correct functioning of the induction machine model. It can be seen that as the rotor resistance is increased the maximum torque increases and starts occurring at lower speeds.

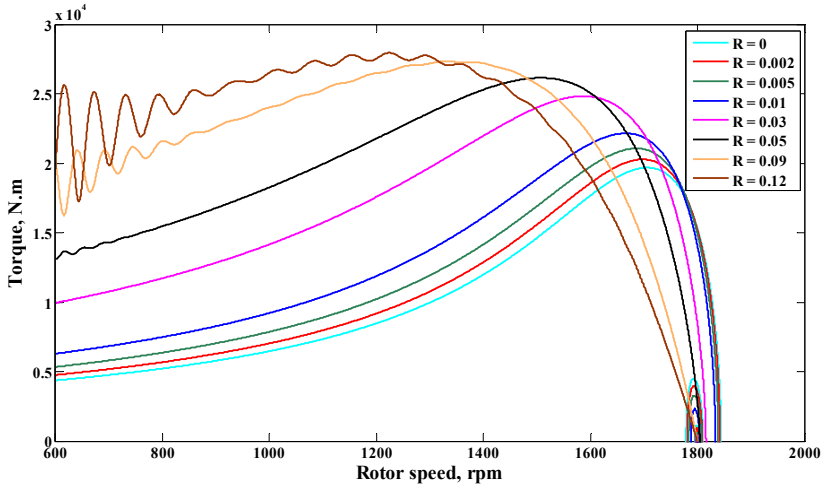

Figure 3.10. Torque vs. rotor speed for different values of rotor resistance.

3.2.4. Operation as Doubly Fed Induction Machine. Hysteresis current control is developed for RSC as illustrated in Figure 3.11. The q-axis and d-axis currents are varied independently to observe the effect on real and reactive power produced by the doubly fed induction machine (DFIM).

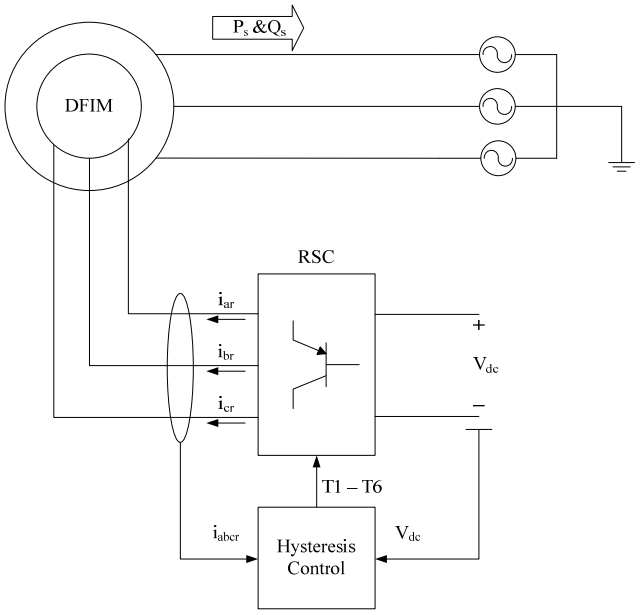

Figure 3.11. Operation as DFIM.

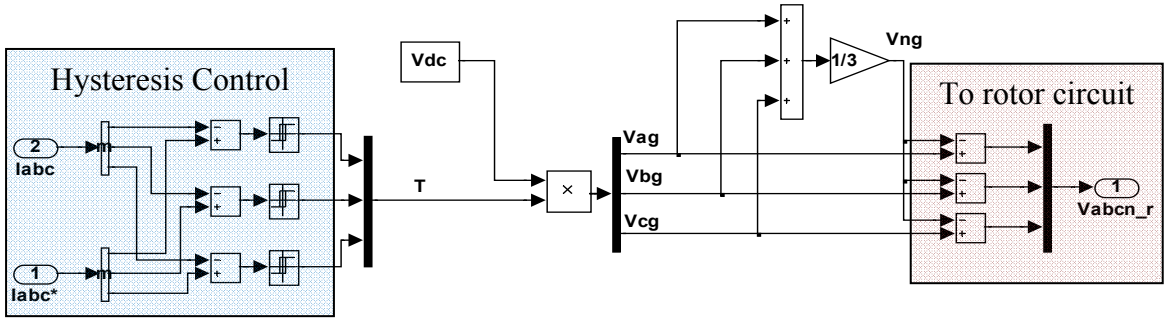

Figure 3.12. Simulation schematic for hysteresis control.

The details of the simulation result are illustrated in Figure 3.13 and Figure 3.14 respectively. The results show that q-axis component of the rotor current controls real power output (P_s) and d-axis component controls reactive power (Q_s) of the machine.

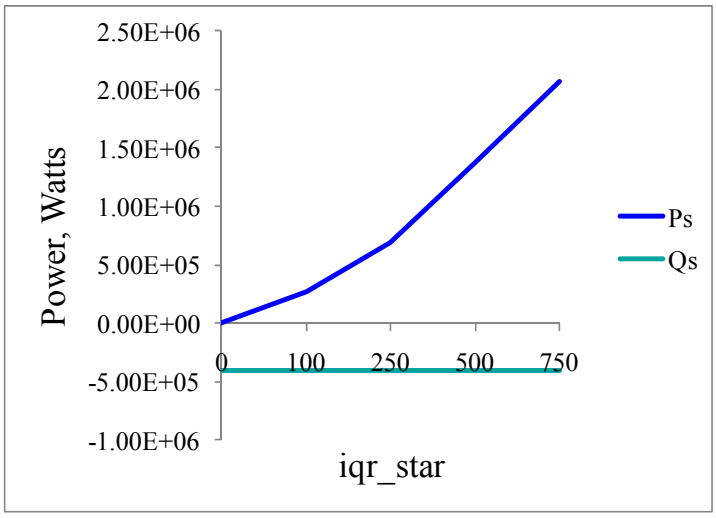

Figure 3.13. P_s & Q_s vs. i_{qr}^*

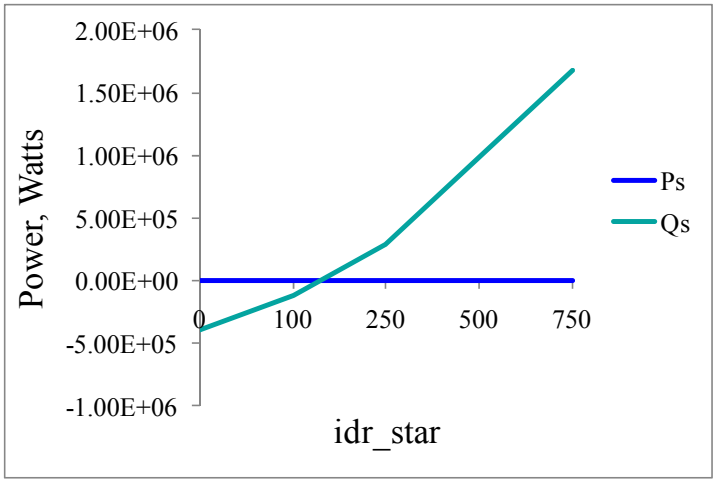

Figure 3.14. P_s & Q_s vs. i_{dr}^*

3.2.5. Real and Reactive Power Characteristics of DFIM. Real and Reactive power control is developed as illustrated in Figure 3.15 to study the power characteristics of DFIM at different speeds of rotor. Here P_{star} is the rated power of the machine whereas Q_{star} is commanded to be zero.

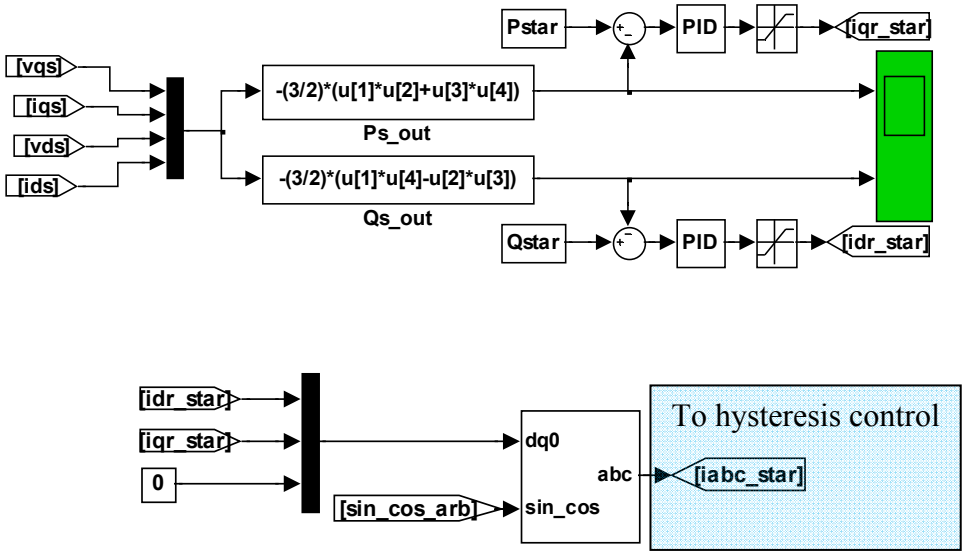

Figure 3.15. Real and Reactive power control.

The results of the simulation are shown in Figure 3.16. It can be seen that the rotor consumes certain amount of real and reactive power during the sub-synchrounous mode of operation while during super-synchronous mode of operation it delivers some amount of real and reactive power to RSC and in synchronous mode of operation rotor consumes only the losses occuring in the machine. Also, it is observed that as the speed increases the amount of power required by the rotor reduces and finally it starts delivering power at super synchronous speed.

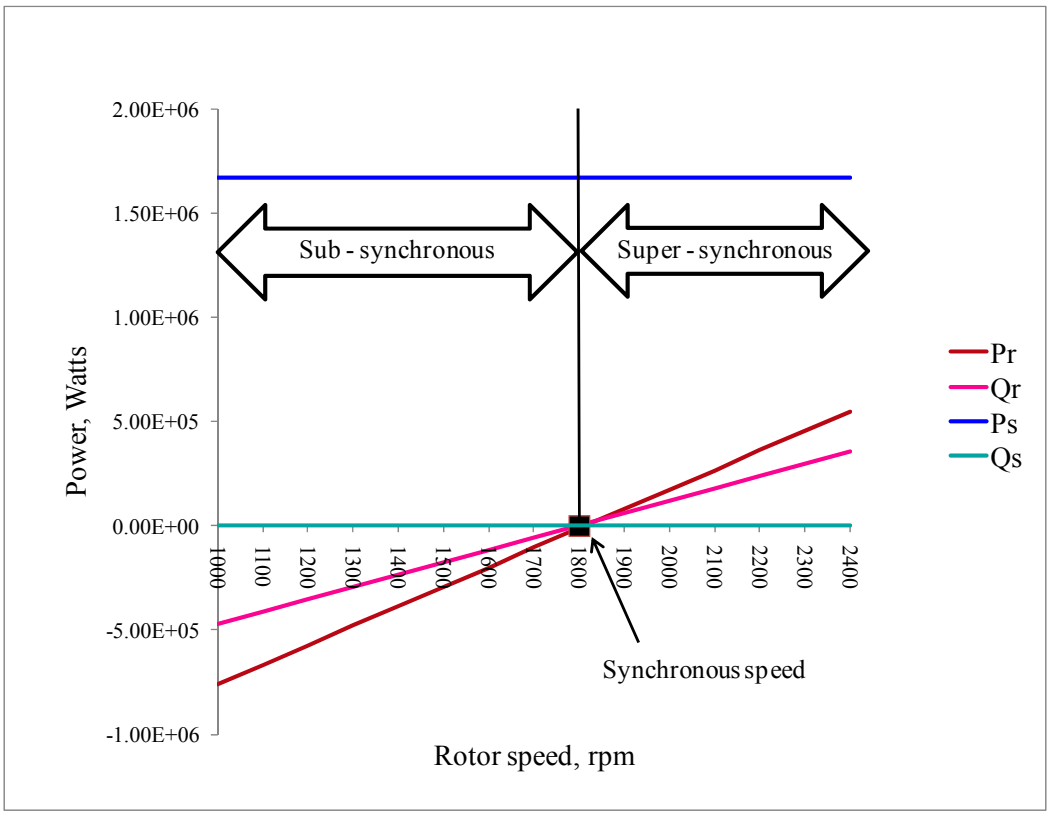

Figure 3.16. Real and Reactive Power characteristics of DFIM.

3.2.6. Developing Control for RSC. The control objective of RSC is to regulate the stator-side active power (P_s) and reactive power (Q_s) independently[37]. From equations (28) and (30) the stator side steady state equations are described as below.

$$v_{qs}^{e} = r_s i_{qs}^{e} + \omega_e \lambda_{ds}^{e} \tag{44}$$

$$v_{ds}^{e} = r_s i_{ds}^{e} - \omega_e \lambda_{qs}^{e} \tag{45}$$

$$\lambda_{qs}^{e} = L_{ss} i_{qs}^{e} + L_M i_{qr}^{'e} \tag{46}$$

$$\lambda_{ds}^{e} = L_{ss} i_{ds}^{e} + L_M i_{dr}^{'e} \tag{47}$$

Here $L_{ss} = L_{ls} + L_M$ and $L_{rr}^{'} = L_{lr}^{'} + L_M$. Substituting flux linkage equations in voltage equation yields following set of equations.

$$v_{qs}^{e} = r_s i_{qs}^{e} + \omega_e L_{ss} i_{ds}^{e} + \omega_e L_M i_{dr}^{'e} \tag{48}$$

$$v_{ds}^{e} = r_s i_{ds}^{e} - \omega_e L_{ss} i_{qs}^{e} - \omega_e L_M i_{qr}^{'e} \tag{49}$$

Re-arranging (48-49) to solve for the stator currents.

$$\begin{bmatrix} i_{qs}^{e} \\ i_{ds}^{e} \end{bmatrix} = \begin{bmatrix} r_s & \omega_e L_{ss} \\ -\omega_e L_{ss} & r_s \end{bmatrix}^{-1} \begin{bmatrix} v_{qs}^{e} - \omega_e L_M i_{dr}^{'e} \\ v_{ds}^{e} + \omega_e L_M i_{qr}^{'e} \end{bmatrix} \tag{50}$$

In the synchronous reference frame $v_{qs}^{e} = \sqrt{2} V_s$ & $v_{ds}^{e} = 0$. Assuming that $\omega_e L_{ss} \gg r_s$ the stator currents can be approximated as,

$$i_{qs}^{e} \approx -\frac{L_M}{L_{ss}} i_{qr}^{'e} \tag{51}$$

$$i_{ds}^{e} \approx \frac{\sqrt{2} V_s}{\omega_e L_{ss}} - \frac{L_M}{L_{ss}} i_{dr}^{'e} \tag{52}$$

The stator power can be derived using (42-43) as below:

$$P_s = -\frac{3}{2}\left(v_{qs}^{e} i_{qs}^{e} + v_{ds}^{e} i_{ds}^{e}\right) = -\frac{3}{2}\sqrt{2} V_s i_{qs}^{e} \approx \frac{3}{2}\frac{\sqrt{2} V_s L_M}{L_{ss}} i_{qr}^{'e} \tag{53}$$

$$Q_s = -\frac{3}{2}\left(v_{qs}^{e} i_{ds}^{e} - v_{ds}^{e} i_{qs}^{e}\right) = -\frac{3}{2}\sqrt{2} V_s i_{ds}^{e} \approx \frac{3}{2}\frac{\sqrt{2} V_s L_M}{L_{ss}} i_{dr}^{'e} - \frac{3 V_s^2}{\omega_e L_{ss}} \tag{54}$$

Figure 3.17 illustrates the vector control scheme of the RSC, in which the independent control of the stator active power (P_s) and reactive power (Q_s) is achieved by means of rotor current regulation in synchronous reference frame. The overall RSC

control scheme consists of two cascaded control loops. The outer control loop regulates the stator active and reactive power independently, generating the reference signals i_{qr}^{e*} and i_{dr}^{e*} respectively. The inner control loop regulates the q-axis and d-axis rotor currents. The output of the two current controllers are compensated by the corresponding cross-coupling terms to form the total voltage signals v_{qr}^{e*} and v_{dr}^{e*}. These voltage control signals are then used by the PWM module to produce gate control signals to drive the RSC. To reduce the size and complexity of the model, commanded signals were assumed to be equal to actual signals and so commanded signals were directly fed to the DFIM rotor circuitry. The rotor to stator turns ratio was assumed to be one.

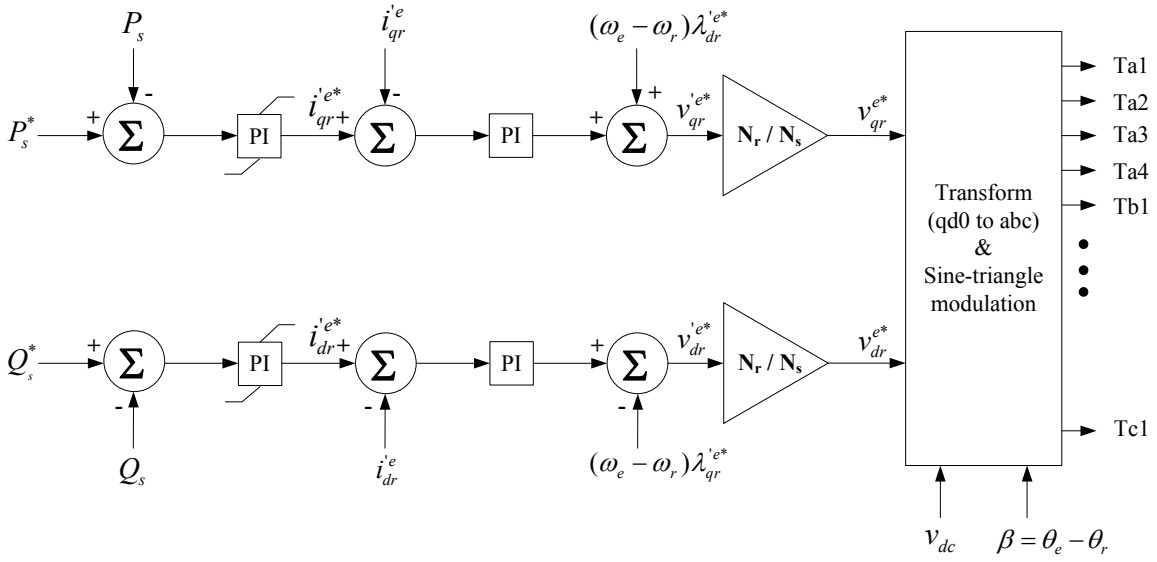

Figure 3.17. Overall vector control scheme for RSC.

The cross-coupling term can be obtained by substituting commanded stator current equations (51-52) in rotor flux linkage equation (31).

$$\lambda_{qr}^{'e*} = \left(L_{rr}^{'} - \frac{L_M^2}{L_{ss}} \right) i_{qr}^{'e*} \tag{55}$$

$$\lambda_{dr}^{'e*} = \left(L_{rr}^{'} - \frac{L_M^2}{L_{ss}} \right) i_{dr}^{'e*} + \frac{L_M \sqrt{2}\, V_s}{\omega_e L_{ss}} \tag{56}$$

3.2.7. Developing Controls and Average Value Model of GSC. The control objective of GSC is to maintain the dc-link voltage (v_{dc}) constant irrespective of the direction of the power flow [26]. Figure 3.18 illustrates the vector control scheme of the GSC. The overall vector control scheme consists of two cascaded control loops. The outer control loop regulates the dc-link voltage (v_{dc}) and generates the reference signal i_{qu}^{e*}. The d-axis current component i_{du}^{e*} is commanded to be zero since no reactive power exchange is desired through the GSC. The inner current loop regulates the q-axis and d-axis components of current. The output of the two current controllers are compensated by the corresponding cross-coupling terms to form the total voltage signals, v_{qu}^{e*} and v_{du}^{e*}. These signals are then used by the PWM module to generate the gate control signals to drive the GSC.

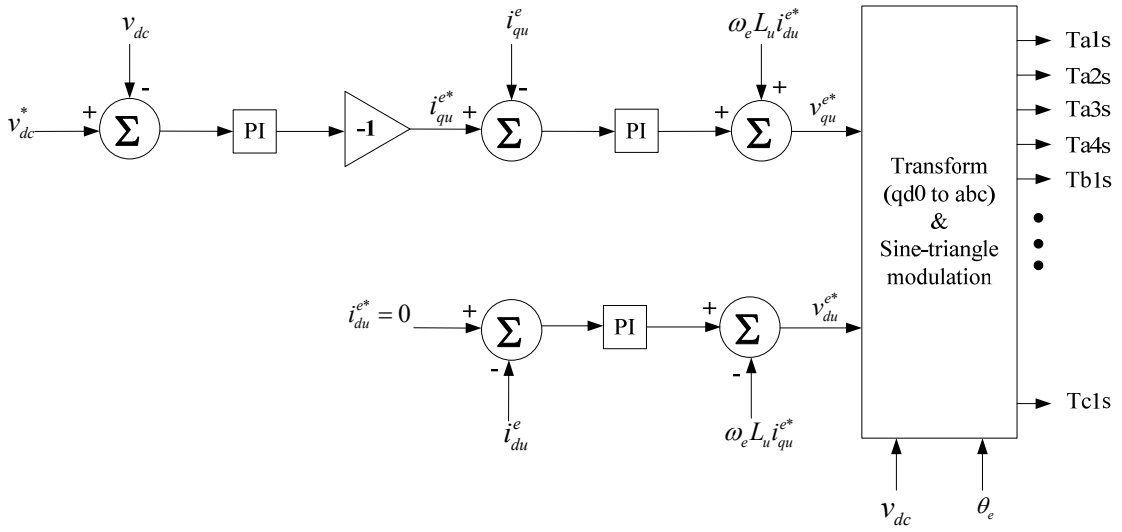

Figure 3.18. Overall vector control scheme for GSC

The GSC is a four-quadrant PWM converter connected to the stator terminals through filter inductors (L_u). The voltage equation in the *d-q* frame rotating at the angular frequency of ω_e are as follows. Here ω_e is the angular frequency of stator voltages.

$$v_{qu}^e = L_u p i_{qu}^e + \omega_e L_u i_{du}^e + v_{qs}^e \tag{57}$$

$$v_{du}^e = L_u p i_{du}^e - \omega_e L_u i_{qu}^e + v_{ds}^e \tag{58}$$

The time average model of GSC can be illustrated as shown in Figure 3.19.

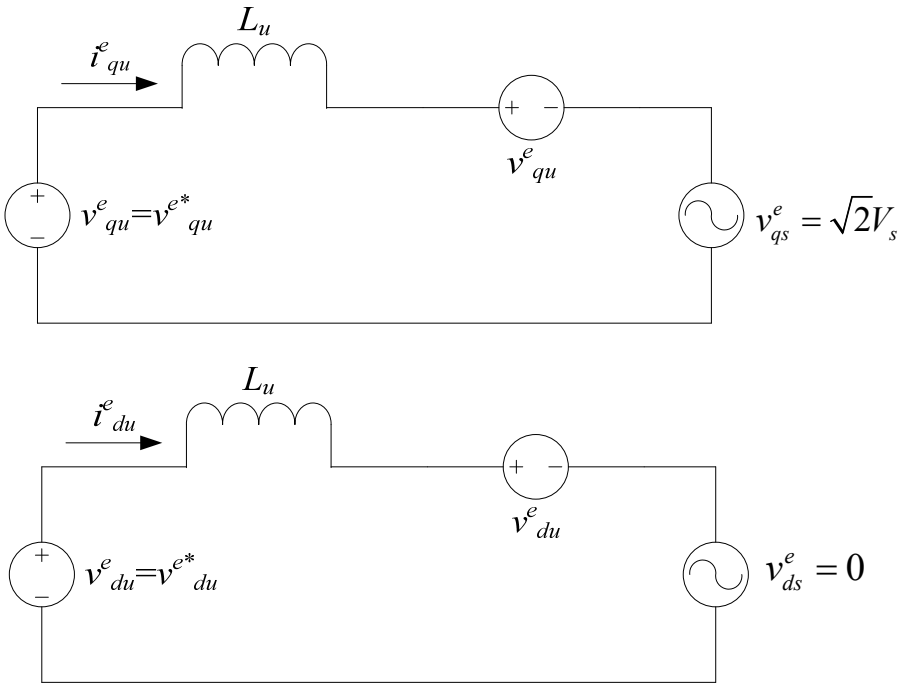

Figure 3.19. Time-average model of the GSC

3.2.8. Simulation Results of the DFIM. Finally the DFIM was simulated under three different operating speeds, i.e., synchronous (1800 *rpm*), sub-synchronous speed (1278 *rpm*), and super-synchronous speed (2348 *rpm*). The simulation results are illustrated in Figures 3.20, 3.21, and 3.22 respectively. It can be inferred from the simulation results that during the synchronous speed, rotor only has to supply the losses occurring in the machine. During the sub-synchronous speed rotor has to supply certain amount of real and reactive power to maintain the stator output power at rated value whereas during the super-synchronous speeds the rotor starts supplying the real and reactive power into the system.

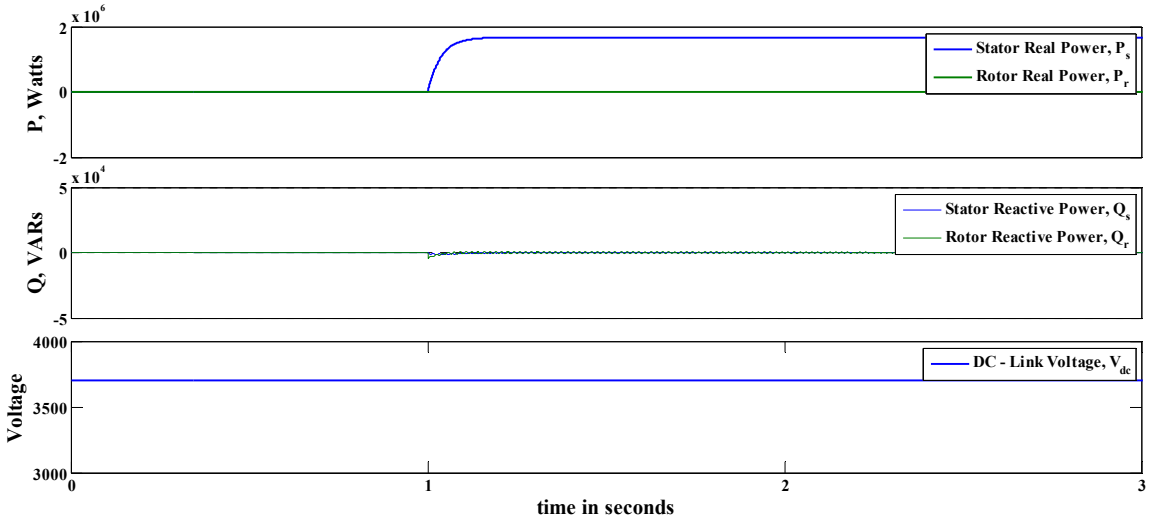

Figure 3.20. Simulation result for synchronous speed ($N_r = 1800\,rpm$)

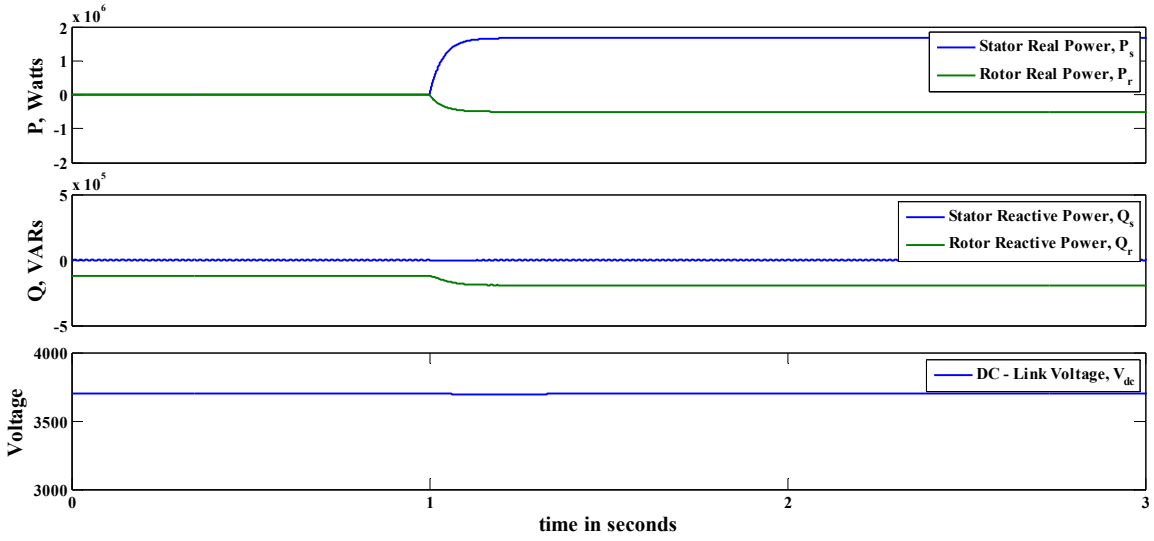

Figure 3.21. Simulation result for sub-synchronous speed ($N_r = 1278\,rpm$)

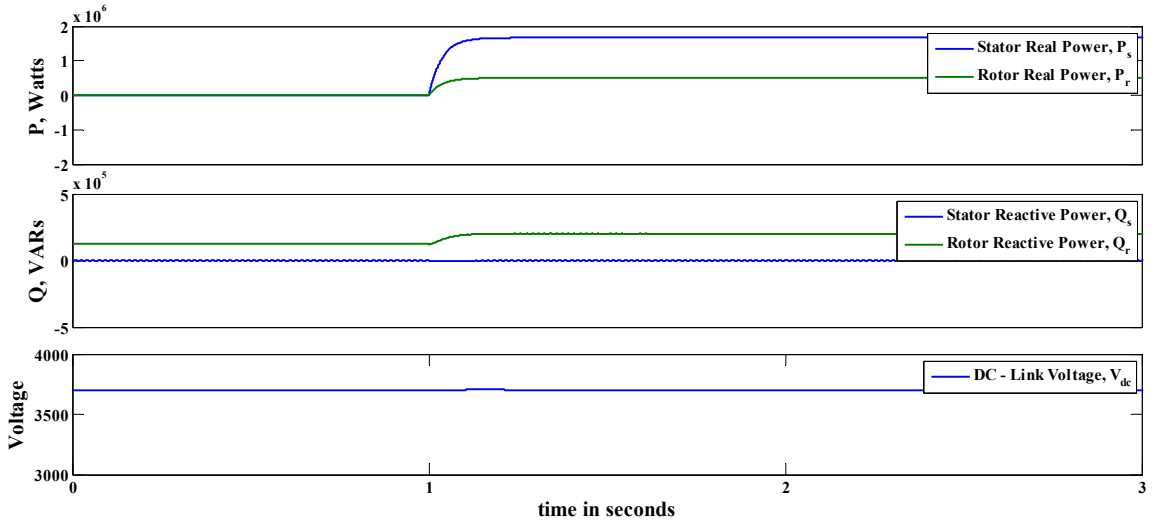

Figure 3.22. Simulation result for super-synchronous speed ($N_r = 2348\,rpm$)

3.3. WIND TURBINE MODELING

The mathematical model of wind turbine comes from the library of SimPowerSystems, Matlab/Simulink. It is a per unit model based on steady state characteristics of the turbine which is further modified as required by the DFIG system [3, 27]. The brief description and characteristics of wind turbine are mentioned in subsequent part of the section.

The power in the air mass that flows at velocity v_{wind} (ms^{-1}) through area A can be defined as:

$$P_{wind} = \frac{1}{2}\rho\pi R^2 v_{wind}^3 \tag{59}$$

Here ρ is the air density and R is the radius of the wind turbine blade. It is not possible to extract all energy from the wind. The fraction of the wind energy extracted is denominated as the performance coefficient of the wind turbine C_P. So the mechanical power of the wind turbine is given by:

$$P_{MECH} = C_P P_{wind} = C_P \frac{1}{2}\rho\pi R^2 v_{wind}^3 \tag{60}$$

The upper limit of C_P is 16/27 (approximately 0.593) which means it is theoretically possible to extract only 59.3% of kinetic energy of wind. This limit is known as Betz limit. The modern three bladed turbines can have C_P value in the range of 0.52-0.55 when measure at the turbine hub. After deducting the losses in the gear box and generator the C_P values comes down to 0.46-0.48. The torque applied to the generator can be easily calculated by using equation:

$$T_{MECH} = \frac{P_{MECH}}{\omega_{turbine}} \tag{61}$$

$\omega_{turbine}$ is the rotational speed of turbine. C_P is a non-linear function of tip speed ratio, λ and blade pitch angle, β. The tip speed ratio is defined as the ratio of blade tip speed to the wind speed.

$$\lambda = \frac{\omega_{turbine} R}{v_{wind}} \tag{62}$$

The general equation for $C_P(\lambda, \beta)$ used to describe the rotor of constant-speed or variable speed wind turbines is:

$$C_P(\lambda, \beta) = c_1 \left(\frac{c_2}{\lambda_i} - c_3 \beta - c_4 \right) e^{\frac{c_5}{\lambda_i}} + c_6 \lambda \tag{63}$$

Here the value of the constants c_1 to c_6 depends on type of wind turbine [3] and manufacturer. The coefficients c_1 to c_6 are: c_1=0.5176, c_2=116, c_3=0.4, c_4=5, c_5=21 and c_6=0.0068. Also,

$$\frac{1}{\lambda_i} = \frac{1}{\lambda + 0.08\beta} - \frac{0.035}{\beta^3 + 1} \tag{64}$$

The $C_P - \lambda$ characteristics are plotted using equations (63-64) for different values of β as illustrated in Figure 3.23. The maximum value of C_P is achieved for $\beta = 0$ at $\lambda = 8.1$. This particular value of λ is defined as the nominal value (λ_{nom}).

The mechanical power P_{MECH} as a function of generator speed, for different wind speeds and for blade pitch angle $\beta = 0°$ is illustrated in Figure 3.24. Based on the turbine power characteristics the power curve for the DFIG is constructed such at the maximum power is tracked at all the wind speeds.

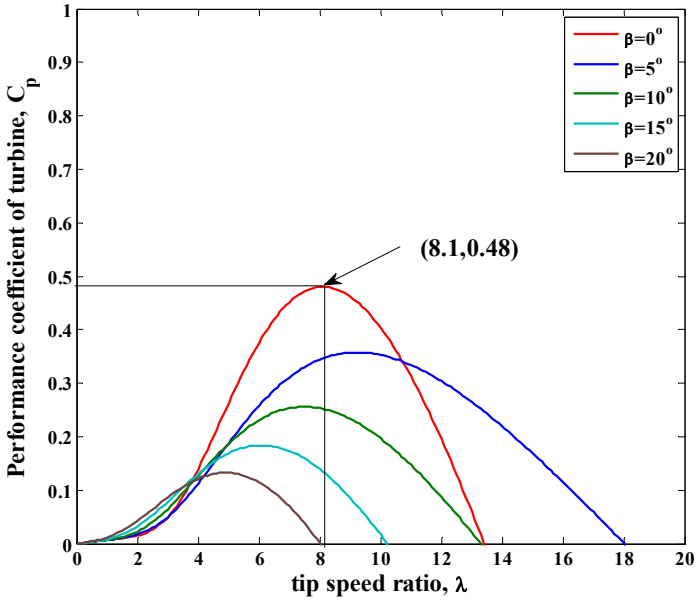

Figure 3.23. $C_P - \lambda$ characteristics.

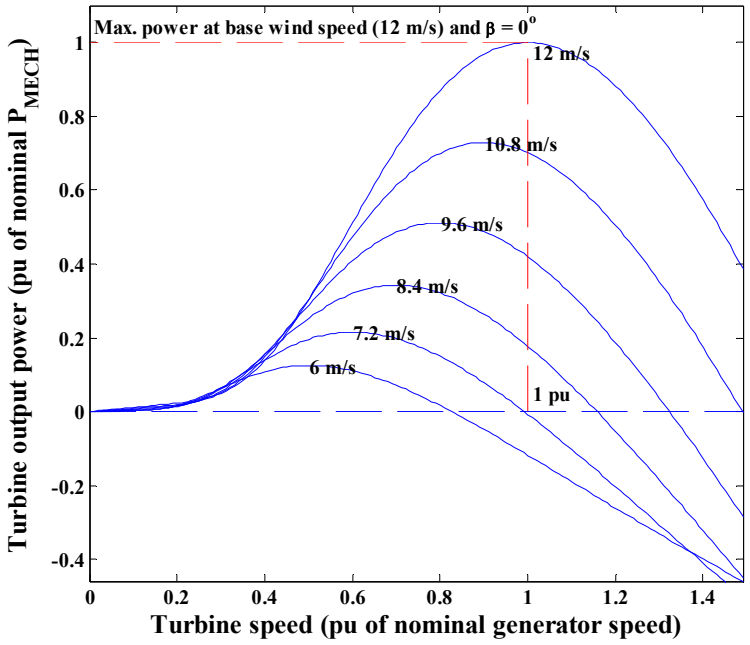

Figure 3.24. Turbine power characteristics for $\beta = 0°$

The power curve for the complete wind turbine generator is illustrated in Figure 3.25. The wind turbine is considered to be fixed pitch ($\beta = 0°$) to take advantage of the wind gusts. The wind turbine and generator are so modeled that even after the base wind speed the generator continues to generate more power through rotor as illustrated in the power curve. The upper limit on the generation is governed by the machine ratings as well as the rating of the power electronic converters.

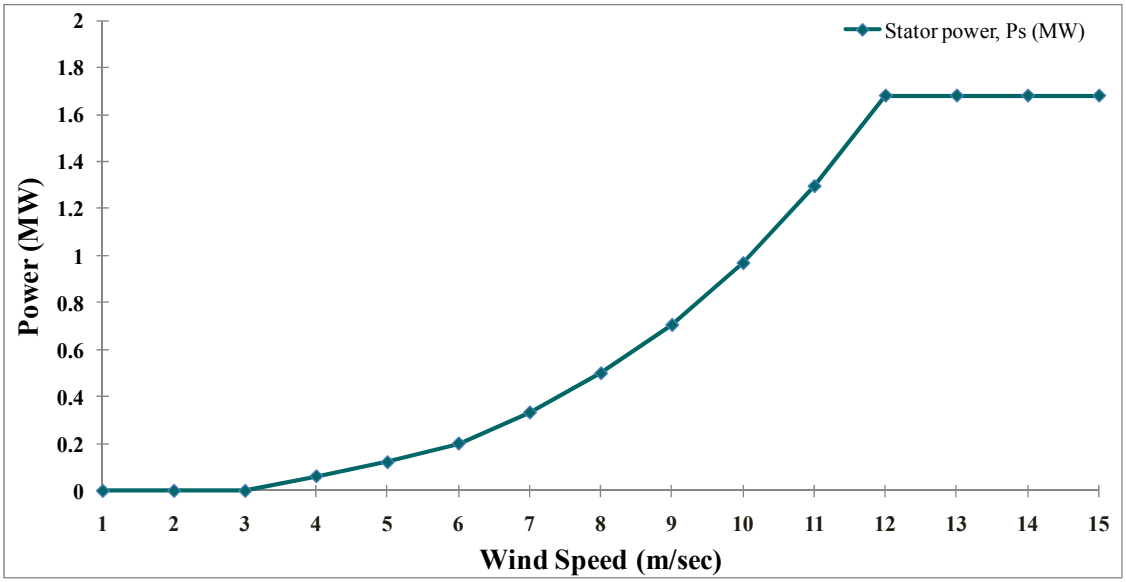

Figure 3.25. Power curve for DFIG wind turbine.

3.4. SUMMARY

This section described the complete mathematical modeling in Matlab/Simulink and operation of the conventional DFIM along with the wind turbine. The rotor side controller uses the stator flux orientation reference frame to control the real and reactive power output from the stator. The grid side controller maintains the dc-link voltage constant with no reactive power share through the converter. The DFIM was simulated

for three possible modes to verify the designed model. Analysis of the developed model was done to study the characteristics of DFIM. In the end the wind turbine model is described using equations. The wind turbine characteristics are displayed along with the maximum power point tracking curve for the DFIG wind turbine under consideration.

4. MODELING, CONTROL AND SIMULATION OF DFIG WTG WITH INTEGRATED ENERGY STORAGE SYSTEM

4.1. INTRODUCTION

A conventional DFIG machine can satisfactorily generate power regardless of the wind speed e.g., the wind speed can be 70% or 130% of the synchronous speed. However, the amount of total power generated precisely depends on the rotor speed of the DFIG. Also the rotor power will be negative (consumed) or positive (delivered) depending upon whether the machine is operating at its sub-synchronous or super-synchronous speeds respectively. Although the DFIG system assists in generating power at most wind speeds, the issue of fluctuating wind power is not yet solved.

In order to study the effectiveness of the proposed method, real wind data is needed. Figure 4.1 illustrates the profile of the wind speed data from Chicago city for 22:30 hrs. The resolution time for the data is 5 minutes. This data has been used in this section.

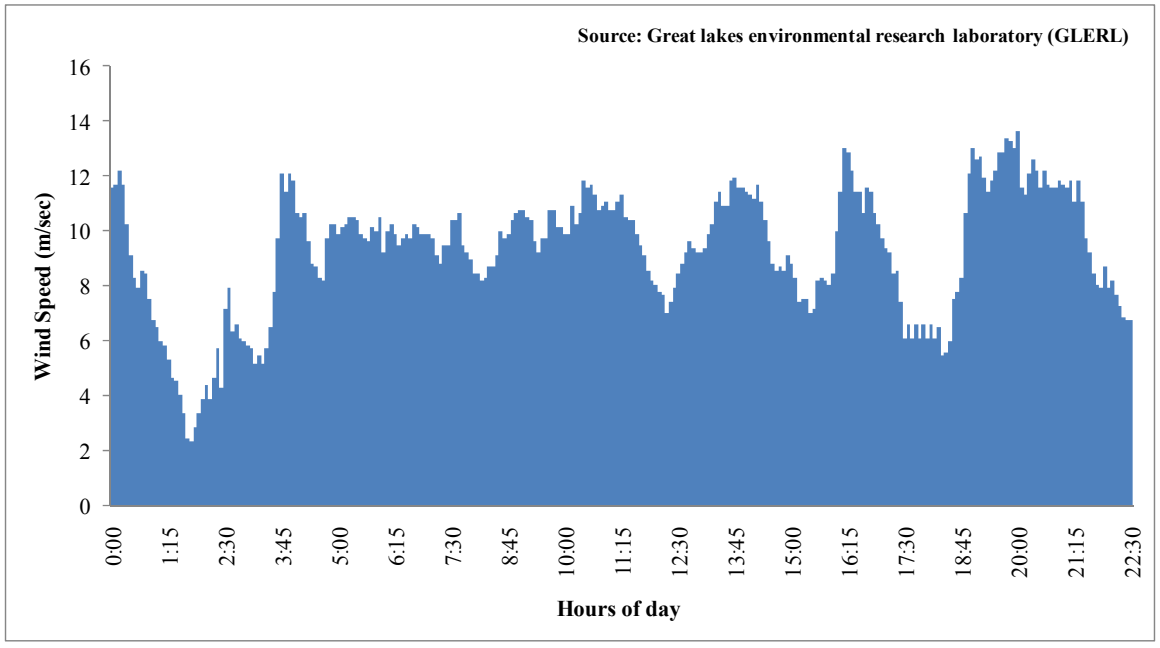

Figure 4.1. Wind speed data for Chicago city for 22:30 hours.

The wind profile shown in Figure 4.1 is fed to the wind turbine attached to a conventional DFIG machine developed in section 3 and its outputs are observed. Figure 4.2 illustrates the simulation results. The first plot is the wind speed (m/s) and the second plot shows the stator power P_s (MW) as well as rotor power P_r (MW) at every instance of the wind speed. Finally, the third plot shows the total or grid power, P_g=P_s+P_r (MW). It can be observed that sudden fluctuations in the wind speed are reflected in the total power (P_g) generated by the wind turbine. This simulation results is only for one 1.67 MW DFIG WTG. Imagine a wind farm consisting of 50 such wind turbines. These sudden variations in the wind speed can cause huge disturbances in terms of voltage and frequency on the power system network. It is not possible for us to change the wind speed; however, the output power can be regulated. This can be accomplished with the help of energy storage systems.

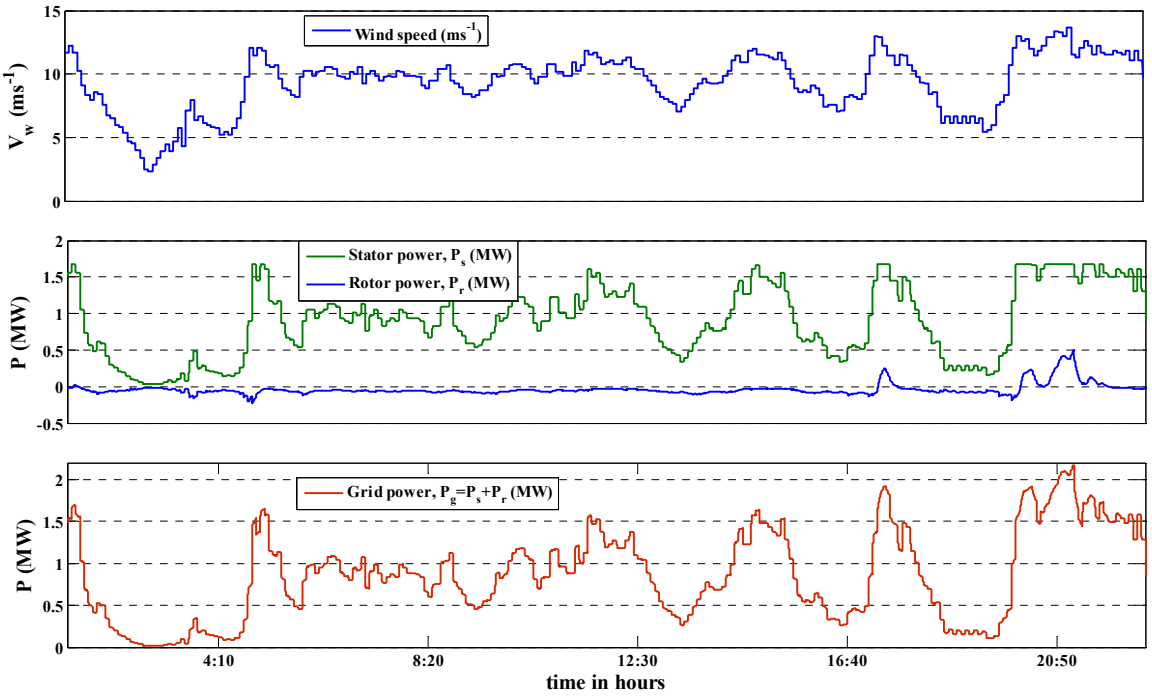

Figure 4.2. Output power of DFIG WTG for a realistic wind profile.

4.2. STUDY ON INTEGRATION OF ULTRA CAPACITOR (UC) ENERGY STORAGE

Since the DFIG system already consists of two integrated converters, it is always preferred to use them as opposed to add a new converter. Ultra-capacitor (UC) energy storage is considered for wind energy storage application in this section due to its several advantages over battery energy storage system.

- ✓ UCs are ideally suited for application needing repeated bursts of power from fraction of a second to several minutes. They are considered efficient as they can quickly store and release electrical energy in the 'physical' form.
- ✓ It can discharge in matters of milliseconds or as long as tens of seconds or several minutes. It can also be charged in seconds to minutes.
- ✓ Very high cycle life in comparison to batteries, making them absolutely suitable for several charge/discharge cycles.
- ✓ There is no danger of overcharging; when fully charged the UC quits charging.
- ✓ Little degradation over hundreds of thousands of cycles. Good reversibility.
- ✓ Low internal resistance in comparison with batteries.
- ✓ UCs have wide operating temperature range from extremely low temperatures (-40^{o} C) to temperatures as high as ($+40^{o}$ C).
- ✓ High power density due to high discharge current.
- ✓ DC-DC round trip efficiency is in the range of 90% to 95%.
- ✓ There is no chemical action in UCs nor do they have any hazardous substances that damage the environment. Environmental friendly.

Despite several advantages, there are certain disadvantages associated with UCs. But they can be taken care of while designing the controls.

- ✓ Amount of energy stored per unit weight in first generation UC is considered lower than that of electrochemical batteries.
- ✓ The voltage varies with the energy stored. In order to efficiently store and recover energy, sophisticated electronic control and switching equipment is required.

At first, a study was done to replace the dc-link capacitor with an ultra-capacitor energy storage device as illustrated in Figure 4.3. The proposed system can store excess energy during increase in the wind speed as well as delivers energy during a sudden reduction in the wind speed. This will smooth out the variations in the generated output power. This smoothening effect ultimately depends on the size of the energy storage unit and variations in the dc-link voltage.

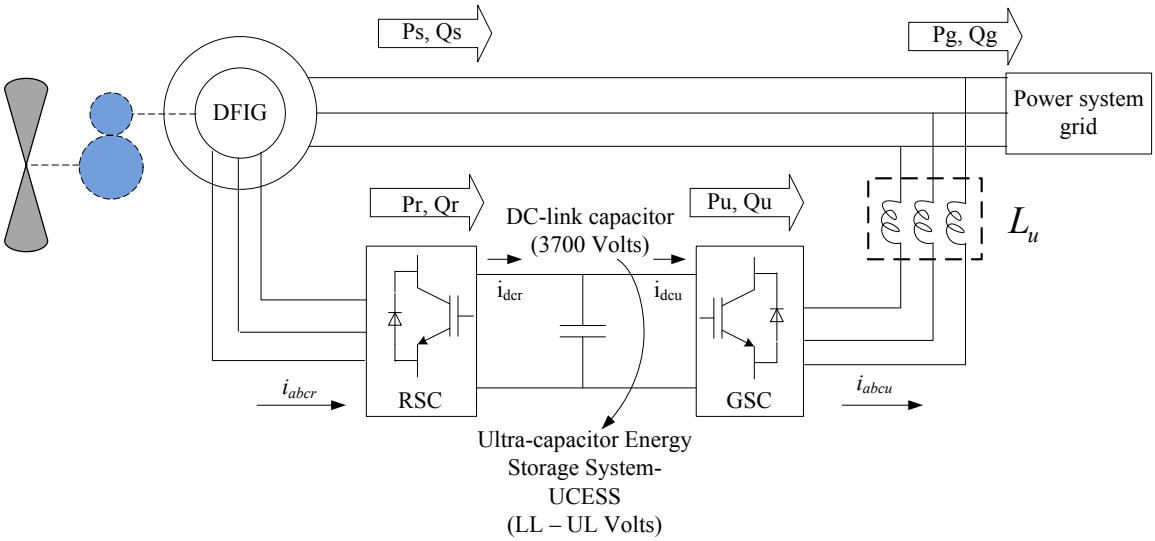

Figure 4.3. DFIG with integrated UC ESS.

In order to replace the dc link capacitor operating at fixed voltage by a variable voltage ultra-capacitor energy storage, it is important to analyze the minimum dc voltage required by the RSC at different wind speed which directly depends on the amount of rotor power required by the system. Figure 4.4 illustrates the modified power curve of the WTG to take maximum advantage of the system. The maximum stator power and grid power is limited to 2.075 MW's and depending upon the commanded stator power the minimum dc link voltage is calculated as shown in the figure. From the graph it can be

determined that the minimum dc link voltage required by the RSC is 1800 Volts during the entire range of the wind speed. Variations in the dc link voltage will not affect the rotor power but it will increase the amount of stress and losses on the utility side inductor (L_u) and hence care is to be taken to make sure that the dc link voltage on GSC is always constant. It can be seen from the modified power curve that the rotor starts generating power once the power generated from the stator side is limited to a specific value. This feature of the WTG can be specifically used to harvest energy from the wind gusts.

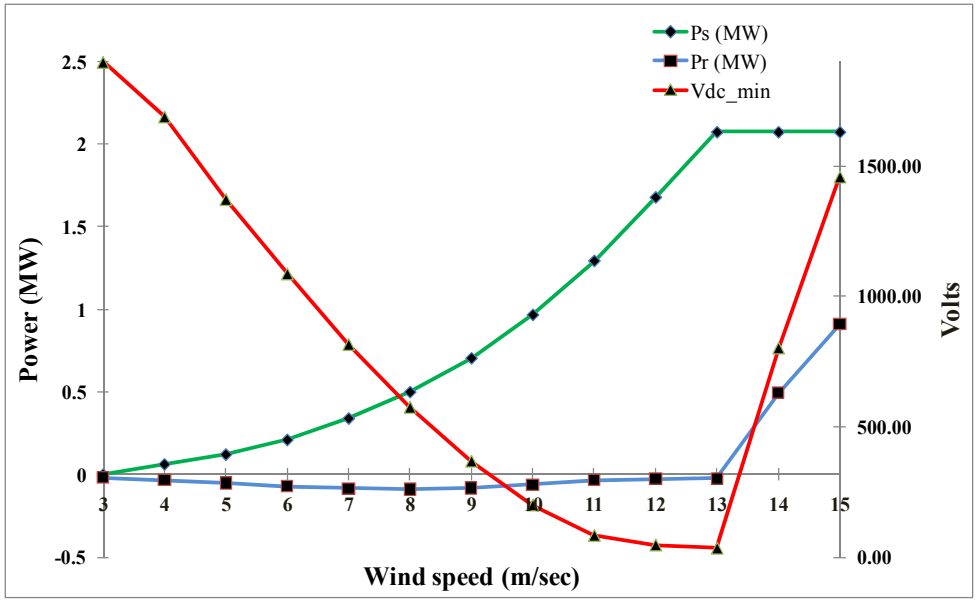

Figure 4.4. Stator power (P_s), rotor power (P_r) & $V_{dc\ min}$ vs. wind speed.

4.3. NEW DFIG SCHEME WITH INTEGRATED ULTRA CAPACITOR ESS

The analysis done in the previous sub-section suggests that RSC can be supplied from a variable dc voltage with a limit on the minimum and maximum voltage whereas the GSC has to be supplied from a fixed dc link voltage. Here, a new DFIG scheme with

integrated ultra-capacitor energy storage system is proposed which takes care of the above limitations.

4.3.1. Proposed System Description. Figure 4.5 illustrates the new DFIG scheme with ultra-capacitor energy storage system (UCESS) which is connected to the RSC. The lower limit and upper limit on the dc voltage of the UC is governed by the minimum voltage required by the RSC and the stress on the power electronic switches respectively. A bi-directional buck-boost dc-dc converter is used to connect the variable voltage which appears across the UC to a fixed-voltage dc link. The fixed voltage dc link is connected to GSC so that the stress on the utility inductor can be limited. The main purpose of the bi-directional dc-dc converter is to isolate the rotor side from the grid side. The size of the UCESS is 3.6 Farads whereas for the dc link capacitor it is 1 Farads. The direction of the arrows is the positive convention of the currents.

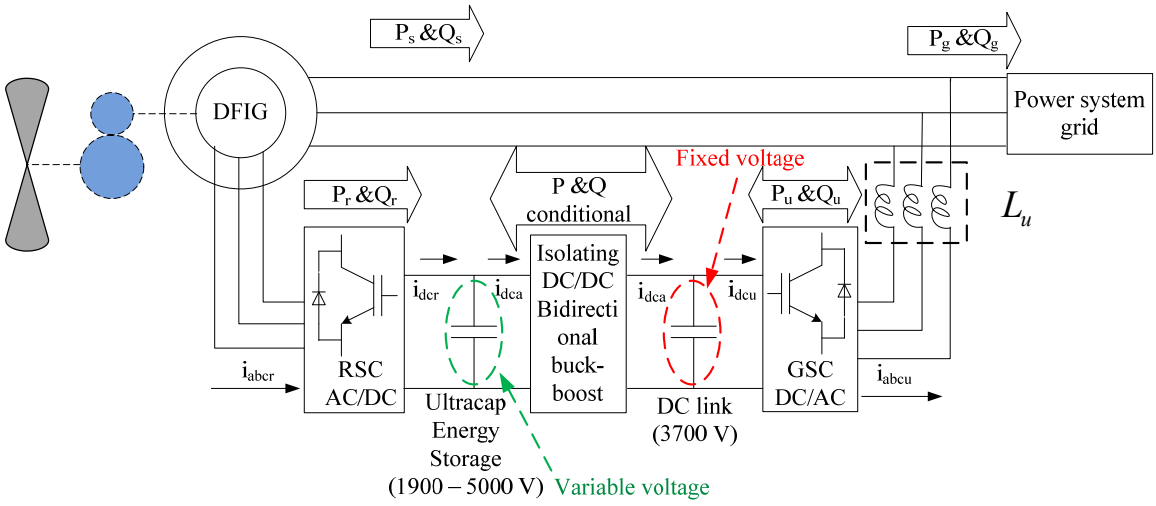

Figure 4.5. Configuration of DFIG WTG with integrated UC ESS.

The dc-dc converter is modeled as illustrated in Figure 4.6. Here d is the switching duty ratio, v_{uc} is the ultra-capacitor voltage and v_{dc} is the dc-link voltage.

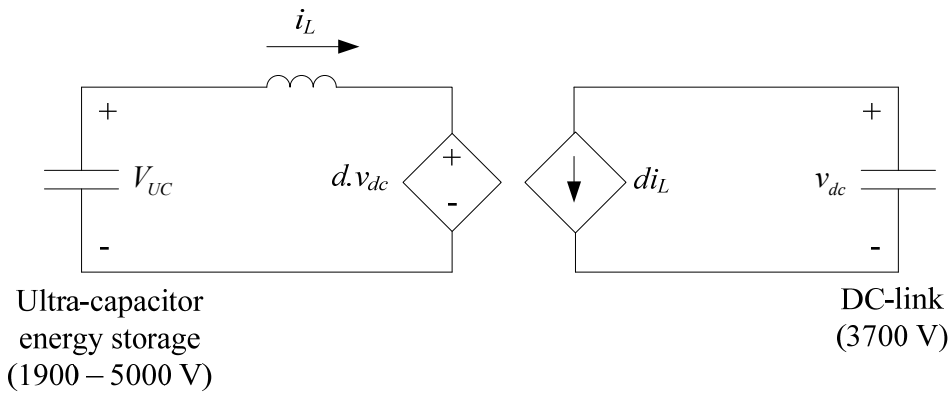

Figure 4.6. Modeling of dc-dc converter.

4.3.2. System Operation. The operation of a conventional DFIG system is illustrated in Figure 4.7. During the sub-synchronous mode of operation, a fraction of the stator energy goes back into the machine through the power electronic converters. Whereas, in super-synchronous mode of operation, the rotor starts generating power which adds up with the stator power to become the total generated power. These modes of operations are known as the conventional modes.

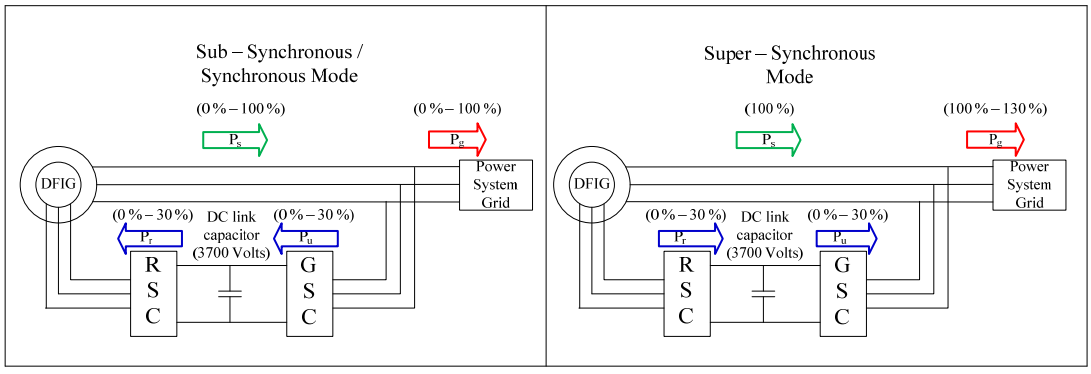

Figure 4.7. Operation modes in conventional DFIG.

In the new scheme with addition of UCESS and a bi-directional dc-dc converter the operation becomes more complicated and has 4 different modes of operation as illustrated in Figure 4.8.

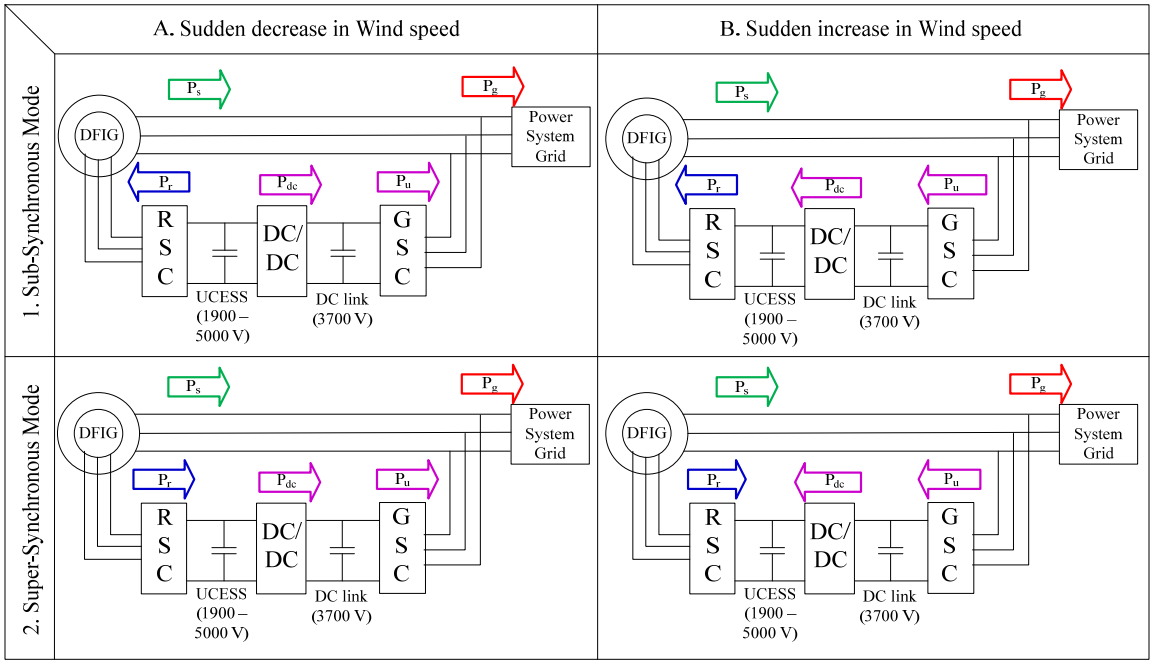

Figure 4.8. Modes of operation for the new scheme.

In Figure 4.8, four different hybrid modes of operation are shown. During this 4 hybrid modes of operation, it is assumed that the UCESS is not hitting any of its upper or lower limits. The new scheme starts operating in conventional modes of operation if UCESS hits any of its boundary limits. The detailed description regarding the different hybrid modes is as follows:

Mode 1A. In this mode, the UCESS is supplying the required rotor power to the machine as well as to the grid to compensate for the reduction in the wind power.

Mode 1B. The UCESS is supplying the required rotor power since it is the sub-synchronous speed operation and the grid-side converter is supplying power to the UCESS in order to smooth out the increase in the generated wind power.

Mode 2A. During this mode, the machine is producing power through the stator as well as the rotor. Therefore, the UCESS is getting charged but due to the reduction in the wind speed power has to be supplied to the grid from ESS.

Mode 2B. In this mode, the UCESS gets charged from both sides since it is super-synchronous mode of operation and because of sudden increase in the wind power, the grid-side converter is injecting power into ESS.

4.3.3. Developing Control for the New Scheme. The main purpose of developing controls is to smooth out the variations in the wind power with respect to the changes occurring in the wind speed as shown in Figure 4.2. In the conventional DFIG scheme the rotor power (P_r) and the utility/grid side converter power (P_u) were the same but in the new scheme with integrated UCESS they are different except when the UC voltage hits its boundary conditions. The new scheme enables control over the utility side converter power (P_u). So the control scheme will decide depending upon the variations of the stator power to whether inject P_u or absorb P_u. The output or the grid power can be controlled in various ways depending on the purpose of the control scheme. Herein, a simple control scheme is designed to smooth out the fluctuations in the output power of the WTG. Figure 4.8 illustrates the wind speed profile for 22:30 hours of a day in blue and the profile in red is after the rate limiter which smoothes out the large fluctuations in the wind speed. In addition, depending upon the rate of the change of actual wind speed the control decides whether to inject power into the grid or absorb it. For example during area A shown in Figure 4.9 when the actual wind speed drops instantaneously the desired wind speed is commanding the UC ESS to inject power through the dc-dc converter and during area B when the wind speed suddenly increases the dc-dc converter is storing energy in UC from the grid. The appendix describes the sizing of the ultra-capacitor energy storage system for wind turbine applications.

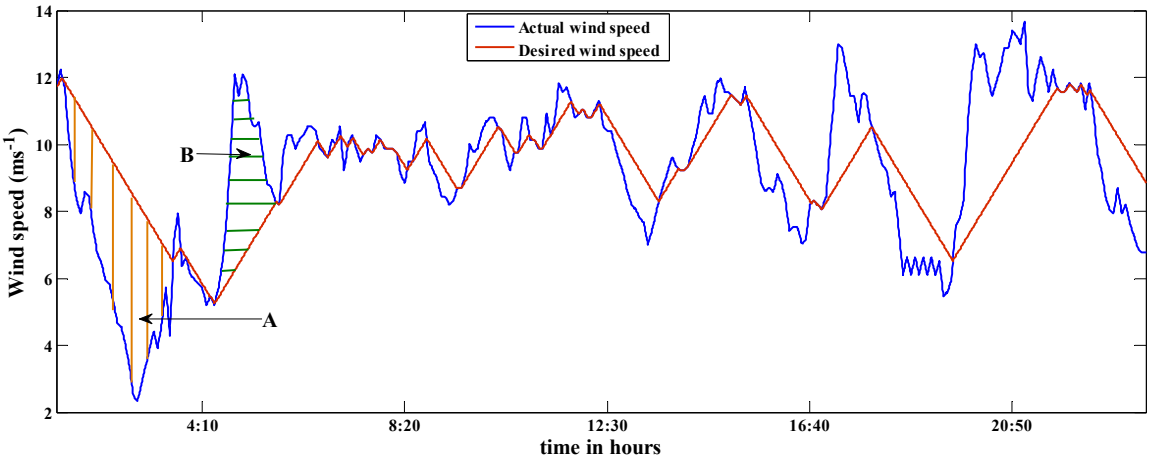

Figure 4.9. Comparing the actual wind speed with desired wind speed.

Figure 4.10 illustrates the control developed for the UCESS. The difference between P_{actual} and $P_{desired}$, i.e., P_u is injected/absorbed by the dc-dc converter into/from the grid. GSC power P_u is then added to rotor power P_r to form total power P_{UC} which is either delivered to or absorbed from the UCESS.

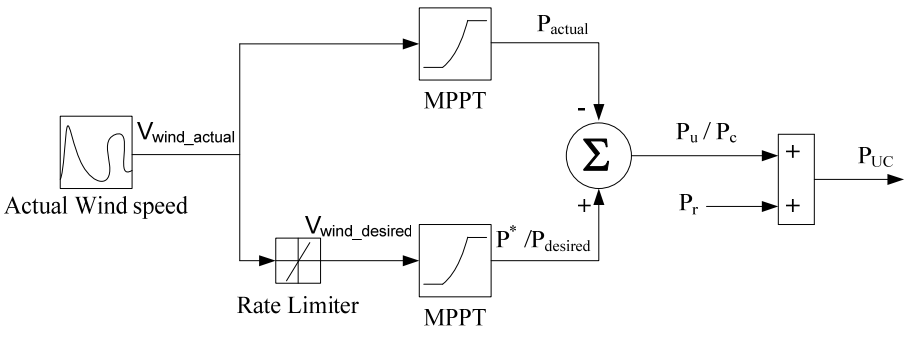

Figure 4.10. Control scheme for the UC ESS.

4.3.4. Simulation Results for the New DFIG Scheme. The control scheme illustrated in Figure 4.10 is implemented. Figure 4.11 illustrates the simulation result for a particular wind profile. The simulation result shows operation in different hybrid modes.

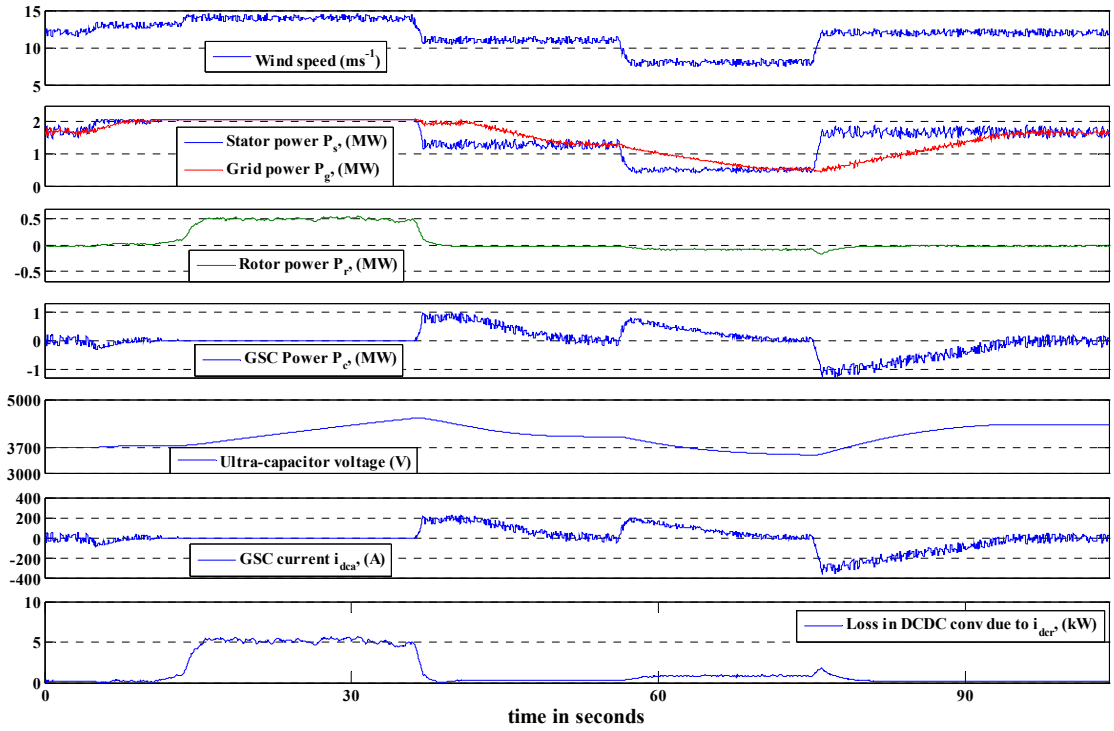

Figure 4.11. Simulation result for DFIG with integrated UC ESS.

The first 35 seconds is mode 2B when the storage system gets charged from both, the rotor as well as the grid-side converter. From 35 seconds till 70 seconds, it is mode 1A where the operation is at sub-synchronous speed and there is a sudden decrease in the wind speed. It can be seen that from 70 second onwards it is operating in mode 1B when the UC gets charged from grid while it is supplying power to the rotor. The first trace is the wind speed which goes from 14 m/s to 8 m/s along with the noise on top of it. The

second trace shows the step change in the stator power due to changes in the wind speed whereas the grid power is a smooth curve. During the super-synchronous speed operation the rotor starts generating power which is shown in the third trace. The amount of power transferred through the dc-dc converter is shown in the forth trace. The fifth and the sixth trace show the variations in the UC voltage and GSC current respectively.

To simulate the entire wind profile of a day, a fast calculation-based model was developed which includes the wind turbine model along with the control scheme illustrated in Figure 4.10. Also to verify the accuracy of the model, the similar wind profile illustrated in Figure 4.11 was simulated. The simulation results are shown in Figure 4.12. These results match with the detailed model simulation.

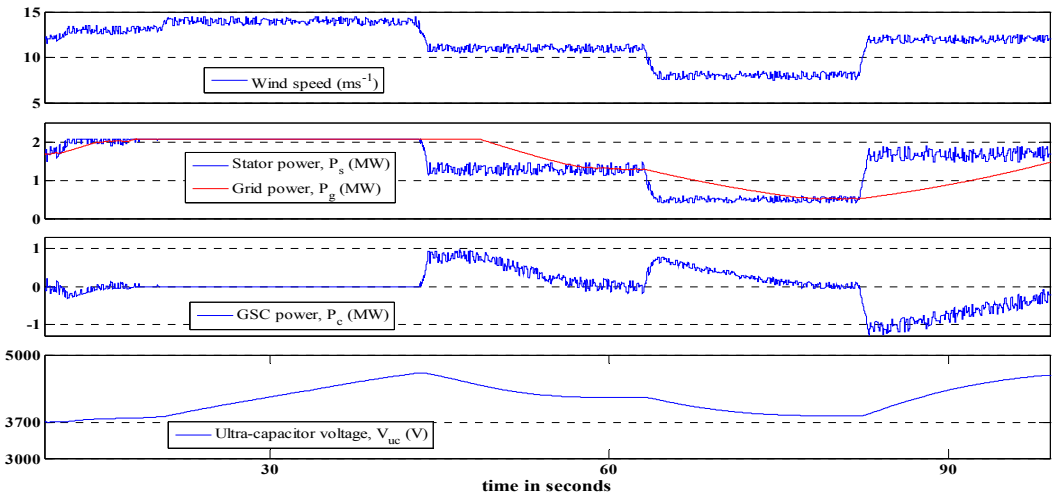

Figure 4.12. Simulation result using calculation-based model.

Once the calculation-based model was successfully developed and tested, a realistic wind scenario illustrated in Figure 4.1 was simulated to see the long-term effects of incorporating the UC ESS in the DFIG system. The simulation results are illustrated in Figure 4.13 and Figure 4.14 respectively. In Figure 4.13, the first trace is the wind speed

(m/s), the second and third traces are the stator and grid power respectively. Figure 4.14 compares the stator power with the grid/total power of the DFIG system.

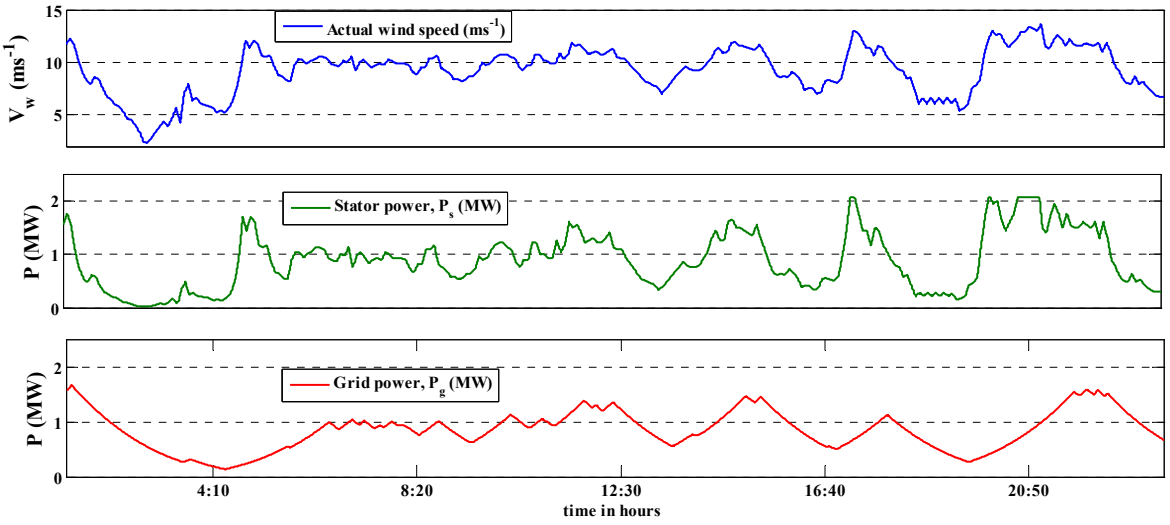

Figure 4.13. Simulation result for DFIG with integrated UC ESS.

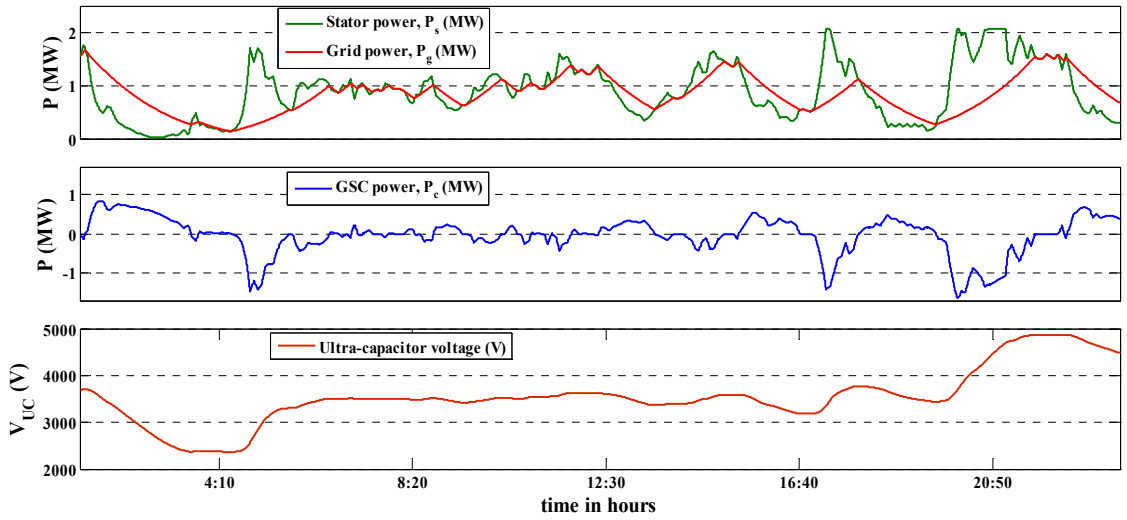

Figure 4.14. Simulation result for DFIG with integrated UC ESS.

In Figure 4.14, the stator power is compared with the grid/total power. The smoothening of the wind power fluctuations can be seen in the first trace. The second trace shows the amount of real power to be injected through grid-side converter to smooth the fluctuations in total output power. The third trace shows the UC ESS voltage fluctuations. The UC voltage reduces when high amount of real power is injected through the GSC and it increases when GSC injects real power into the UC.

4.4. COMPARISION WITH THE OTHER TOPOLOGIES

The topology suggested by few other authors is illustrated in Figure 4.15 [5-6]. The drawbacks associated with this topology are discussed in this subsection. In this particular topology, there are always losses occurring in the dc-dc converter whenever there is power transfer from or to the ESS. These losses become significant when the machine enters super-synchronous mode since most of the power coming from the rotor goes to the ESS.

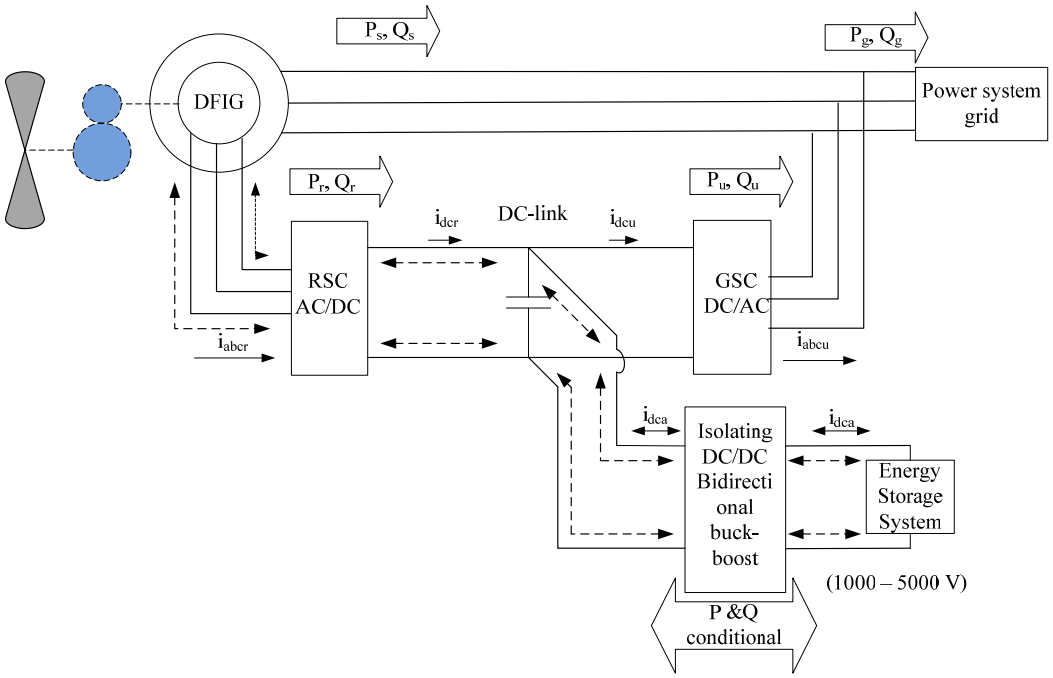

Figure 4.15. DFIG with integrated ESS in parallel with the dc link.

The dotted line in the Figure 4.15 shows the path of energy flow which leads to losses in dc-dc converter and is the major difference between the topology suggested in this thesis. The final trace in Figure 4.11 shows the amount of losses occurring in dc-dc converter due to the power transfer between the rotor and UC ESS during the super-synchronous speed. A loss model was developed using the data illustrated in Table 4.1 for the dc-dc converter shown in figure 4.15. The parameters in Table 4.1 are coming from IGBT chopper module manufactured by Dynex.

Table 4.1. Parameters for dc-dc converter.

V_{CES}	$V_{CE(sat)*}$	$I_{C(max)}$	$I_{C(pk)}$	$V_{CE\text{-}test}$	$L_{dc\text{-}dc}$
4500 V	2.9 V	300 A	600 A	2250 V	10 mH
E_{ON}	E_{OFF}	E_{REC}	V_f	$I_{C\text{-}test}$	$R_{L(dc\text{-}dc)}$
0.9 J	0.75 J	0.3 J	3 V	300 A	0.03 Ω

The loss model was simulated for different wind speeds assuming a switching frequency of 3 kHz and a constant duty cycle. Figure 4.16 illustrates the results of simulation at different wind speeds. It can be observed that losses in the dc-dc converter become significant at super-synchronous speeds. Hence this topology cannot be used for harvesting energy from wind gusts. However, there are no such losses occurring in the topology suggested in this thesis (Figure 4.5) since the power coming from rotor is directly stored in the UC ESS. Here P_{losses} includes the conduction losses occurring in transistor and diode, the switching losses in transistor and losses occurring in the inductor. Thus the losses occurring in the DFIG system are dynamic and they vary with the wind speed.

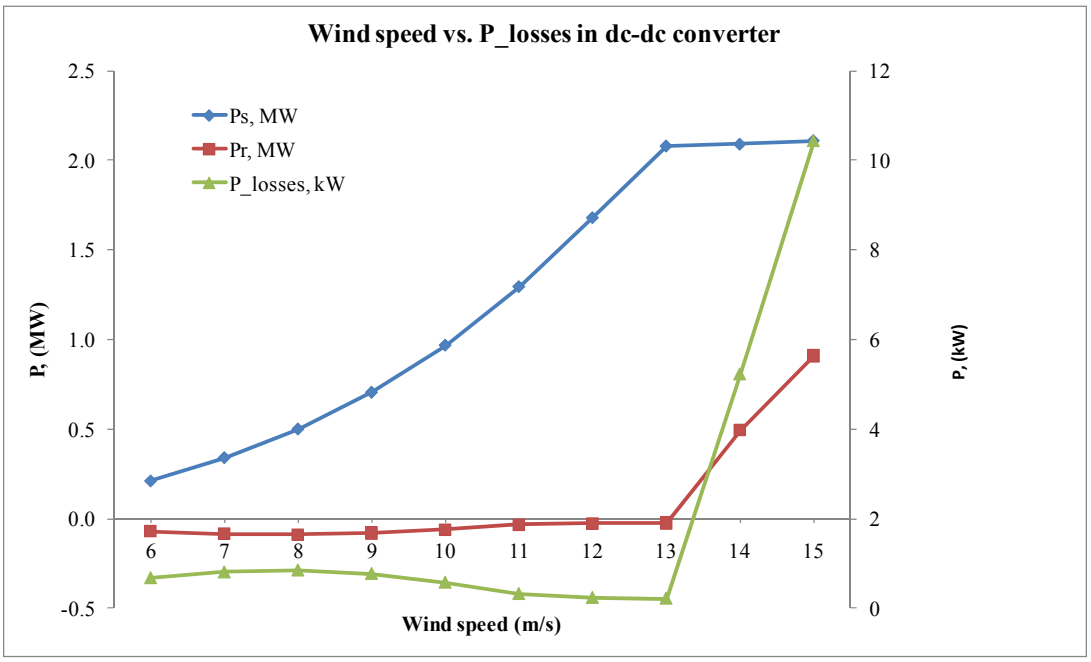

Figure 4.16. Wind speed vs. P_{losses}.

4.5. SUMMARY

This section describes the disadvantage of conventional DFIG scheme and suggests a new scheme with integrated ESS. The detailed study on DC link is done to determine the working range of the UCESS. Different operating modes of this scheme are explained in detail and compared to the conventional scheme. The control for the modified scheme is described in detail. The simulation results show the successful working of the modified new scheme with integrated storage system. Finally the performance of the new scheme is compared with the topology suggested by other authors.

5. ADVANCED APPLICATION OF WTGs: HARMONIC ELIMINATION USING DFIG WITH THE HELP OF MRFSE IN PSCAD

5.1. INTRODUCTION

The primary objective of the electrical utilities is to supply their customers with a sinusoidal voltage of constant frequency and magnitude. On the other side, the customers are also expect to draw ideal sinusoidal currents. The generators that produce electric power, generate a very close approximation to a sinusoidal signal. However, there are loads and devices on the system which have non linear characteristics and result in the harmonic distortion of both the voltage and current signals [13]. As more and more non linear loads are introduced into the system, these waveforms get more distorted as illustrated in Figure 5.1.

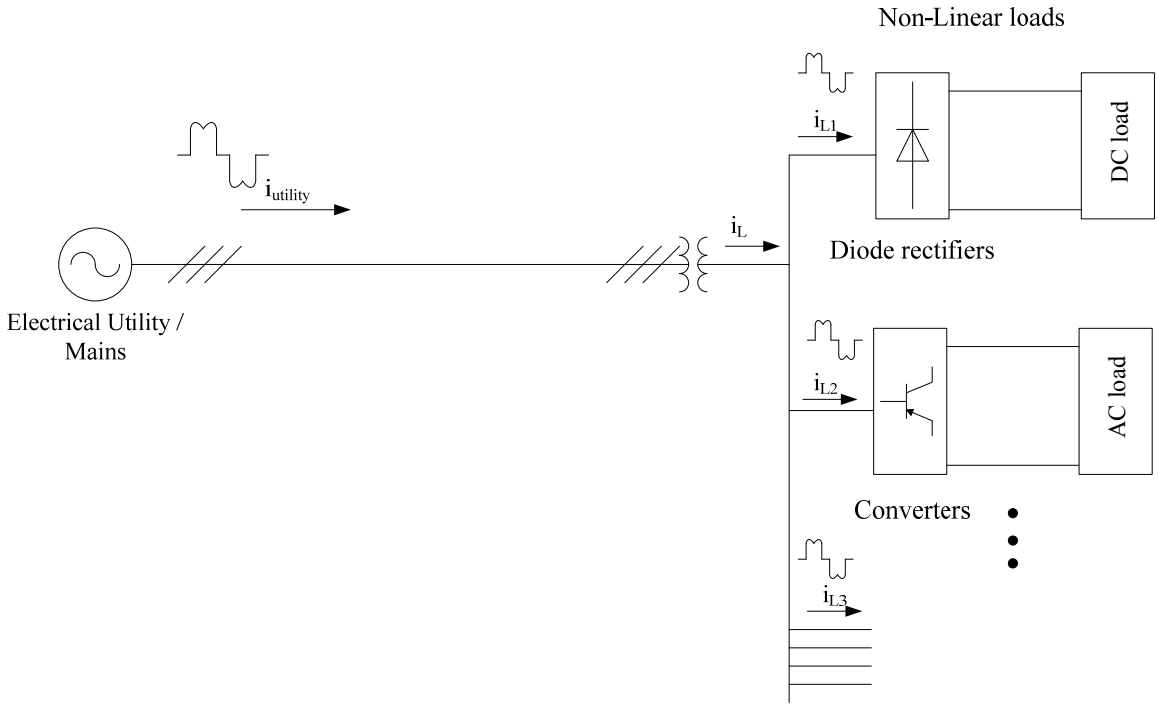

Figure 5.1. Cause for harmonic injection into the power system network.

A majority of the non-linear loads include diode or thyristor front-end rectifiers. These loads inject high amount of current harmonics in today's transmission and distribution networks. They are responsible for causing voltage distortion which depends on the line impedance, additional losses in the transformers and line capacitors, and malfunction of sensitive electronic equipment.

Shunt passive *LC* filters, often called harmonic trap filters, are traditionally used to avoid the flow of harmonics into the power system network. This is a simple and low cost solution but its performance mainly depends on the source impedance and can lead to unwanted parallel resonance with the network. For this reason a shunt active power filter (APF) is considered as an effective solution for low to medium power applications to reduce the current harmonics within the acceptable limits. They are also capable of compensating load unbalance and reactive currents as well. A digitally controlled APF represents a versatile power conditioning tool since different compensation tasks can be modified by changing the software of the digital controller.

Modern high power wind turbines such as DFIGs already have two bi-directional converters. As described in earlier sections, the RSC supplies the required power to the rotor and the GSC acts as an active rectifier maintaining the dc link voltage at a constant level. In this section active filtering capability has been added to the controls of GSC which now acts as shunt active filter apart from being an active rectifier. A multiple reference frame synchronous estimator (MRFSE) is used to pick $6k \pm 1$ harmonics. A new control strategy has been developed to eliminate those harmonics.

Figure 5.2 illustrates the schematic in which the utility is expected to supply purely sinusoidal current to the non-linear load and the harmonics required by the non-linear loads are supplied by the GSC of the DFIG wind turbine. Hence, this wind turbine serves multiple purposes such as supplying real power (*P*), reactive power (*Q*) as well as harmonics required by the load [10-12][36]. This kind of scheme will not only help in reducing losses on the grid but stress will also be reduced resulting in increased life of transmission and distribution equipment.

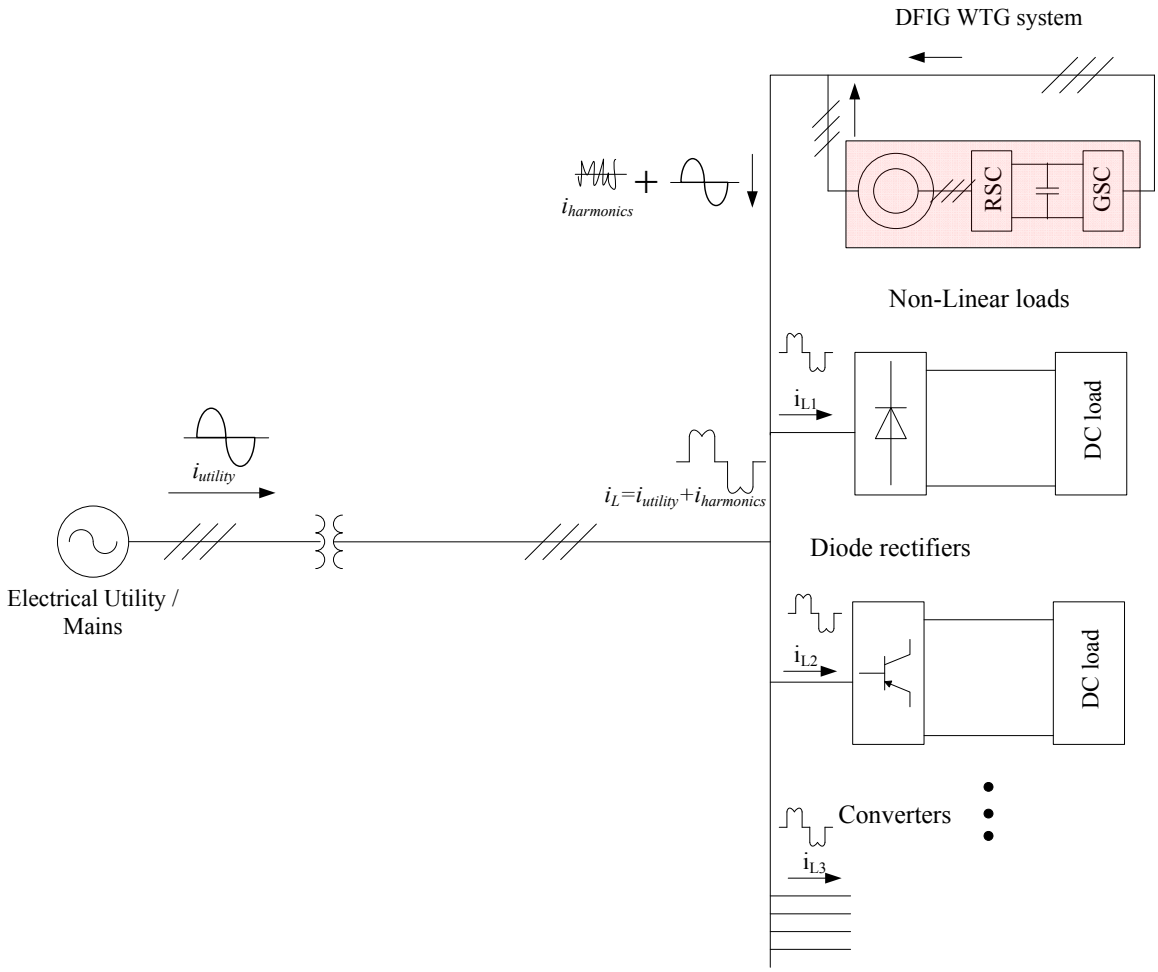

Figure 5.2. GSC of DFIG supplying harmonics required by the non-linear load.

5.2. DETAILED MODELING OF A DFIG IN PSCAD

The detailed model of DFIG was developed using software package PSCAD. Figure 5.3 illustrates the wound rotor induction machine connected to the diode clamped three-level rotor side and grid side converters. The parameters used here for the simulation of DFIG are similar to used in section 2 of this thesis. The dc link capacitor is pre-charged using an external source in series with a breaker. The external source disconnects at 2.5 seconds and GSC takes care of regulating the dc link voltage at 3700 volts. The utility side inductors (L_u) are sized at 250μH. DFIG is operated in the speed

control mode which is directly controlled. The reason for using the multi-level converter is to increase the number of steps in the output voltage. This reduces the stress on the power electronic switches as well as the switching losses. A resistance in connected in series with the dc link capacitor to regulate the dc link voltage. The machine can be operated in various modes such as sub-synchronous, synchronous and super-synchronous modes by controlling the speed input (W) of the induction machine.

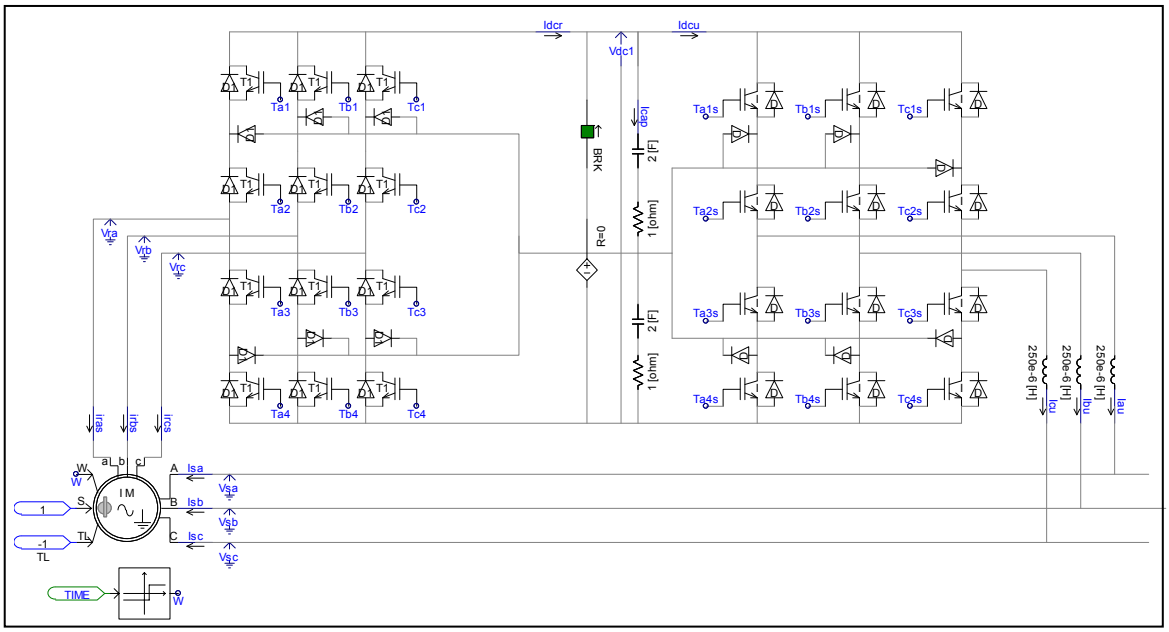

Figure 5.3. DFIG model in PSCAD

The rotor-side controller is developed as illustrated in Figure 5.4 similar to the controls described in section 3. The output of the control scheme is the commanded q-axis and d-axis voltages which produce switching signals using the sine-triangle PWM method. Figure 5.5 illustrates the control for the GSC. It is similar to the control scheme discussed in section 3.

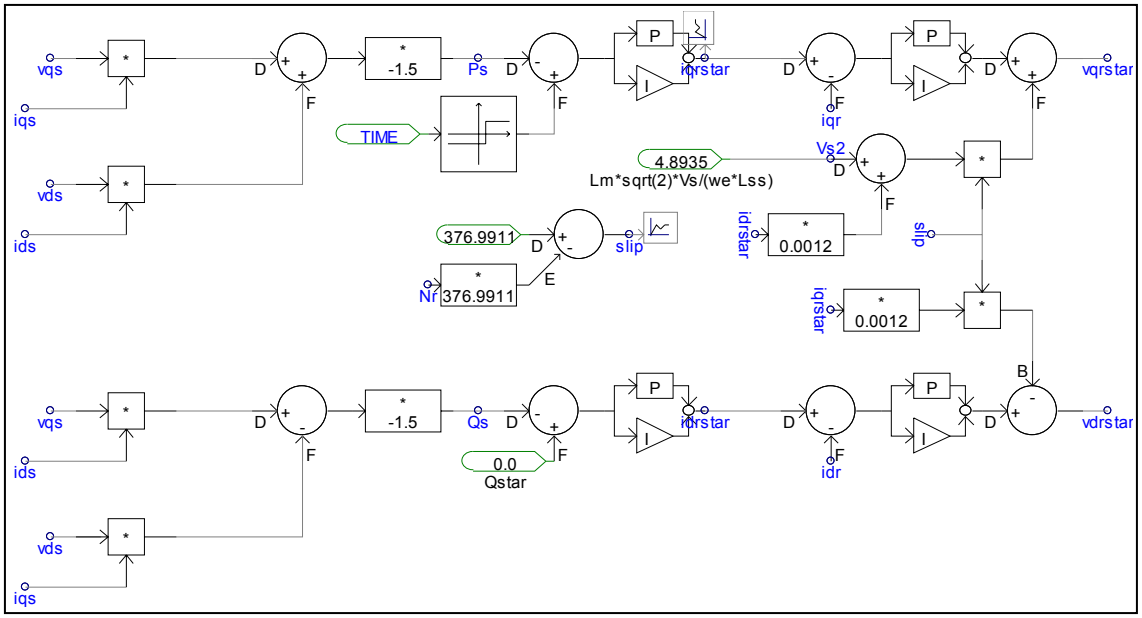

Figure 5.4. RSC control scheme

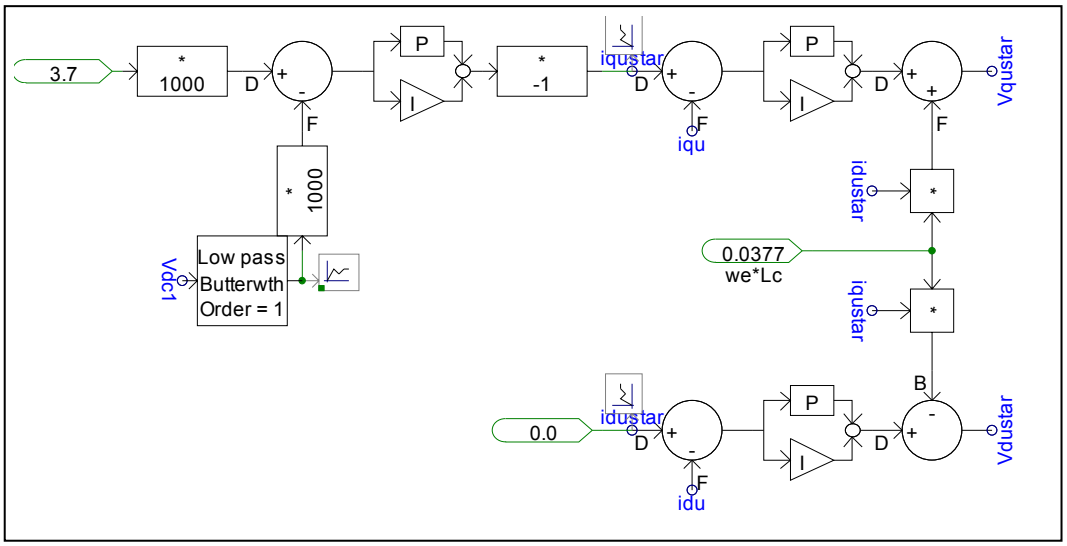

Figure 5.5. GSC control scheme

Sine-triangle modulation is used to produce the transistor gate signals for both the converters. Figure 5.6 illustrates the detailed schematic in PSCAD. The triangle carrier frequency is set to 3 kHz.

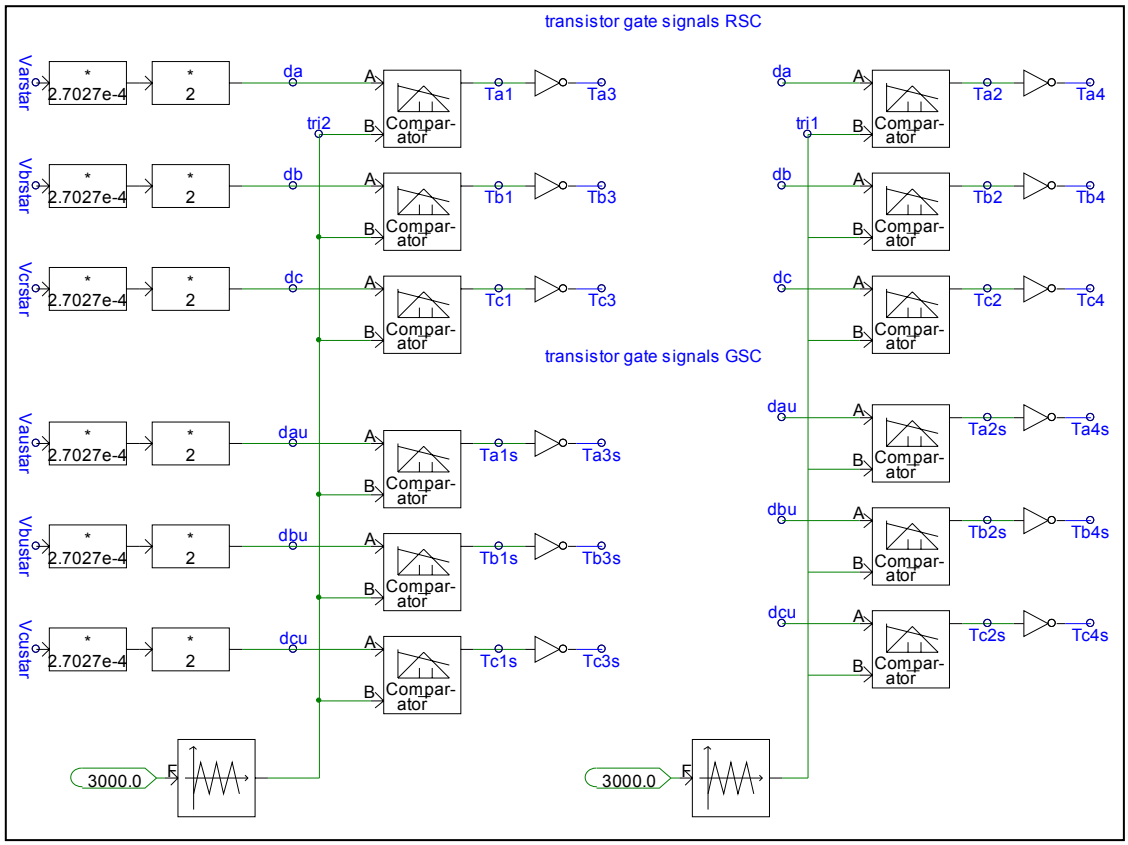

Figure 5.6. Transistor gate signals for RSC and GSC

5.3. SIMULATION RESULTS FOR DFIG IN PSCAD

The DFIG model developed in PSCAD is tested under three different operating conditions. The simulation results show real (P) and reactive (Q) power of the stator and rotor as well as the dc link voltage (V_{dc}) for all of the following three cases.

Case I: Synchronous speed ($N_S = 1800\,rpm$)

The simulation result shows that after 1 second the load on the DFIG is turned on. At synchronous speed the real power output of the stator (P_s) is at rated value (1.67 MWs) whereas the reactive power is commanded to be zero. Also, the rotor supplies slight amount of real power (P_r) to compensate for the machine losses and the reactive power (Q_r) input is negligible. The dc link voltage (V_{dc}) remains constant during the change in the load from zero to its rated value.

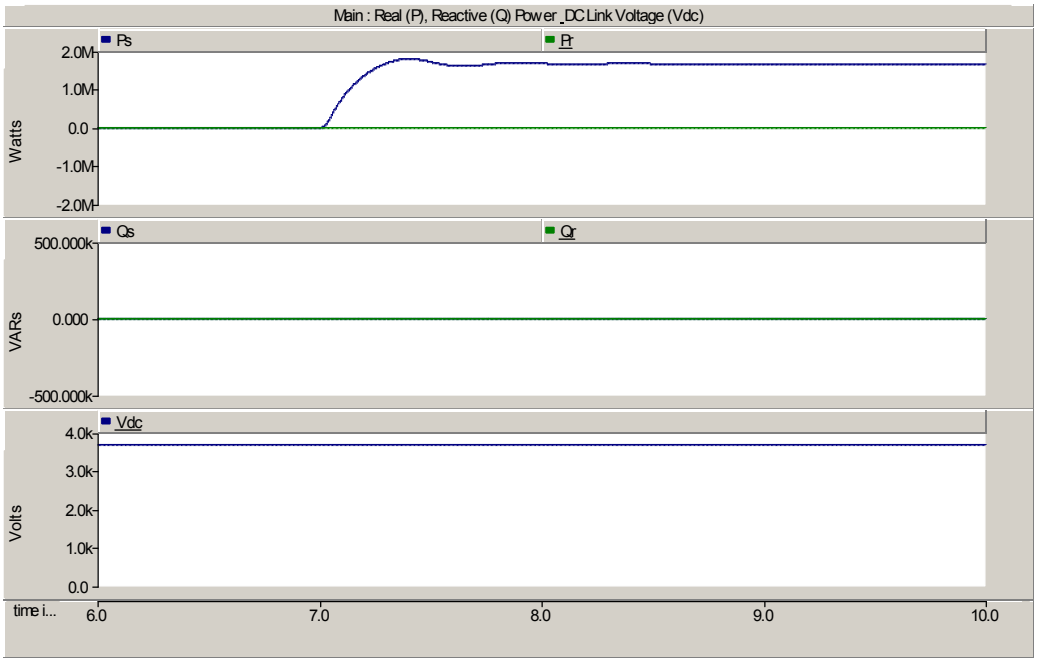

Figure 5.7. DFIG simulation at synchronous speed.

Case II: Sub-synchronous speed ($N_S = 1278\,rpm$)

At sub-synchronous speed to command the rated power out of the machine certain amount of real power has to be injected into the rotor. Also rotor consumes certain

amount of reactive power to maintain the stator power constant. The dc link voltage remains constant.

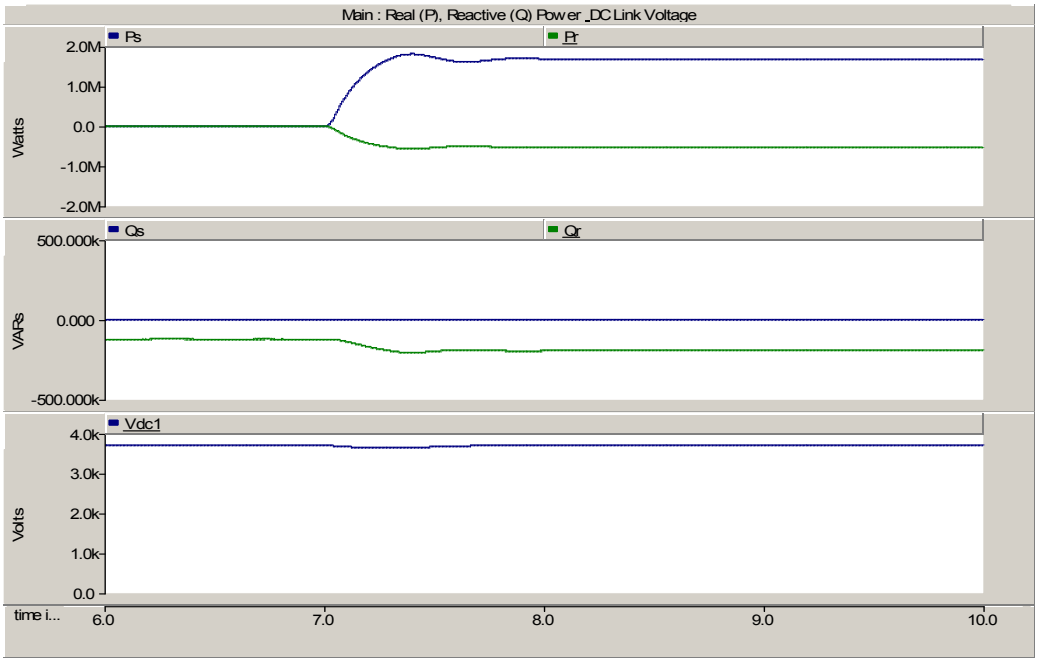

Figure 5.8. DFIG simulation at sub-synchronous speed.

Case III: Super-synchronous speed ($N_S = 2348\,rpm$)

At super-synchronous speeds, the rotor starts producing real and reactive power whereas stator real and reactive powers are as commanded. The dc link voltage remains constant during the transition of the load from zero to its rated value.

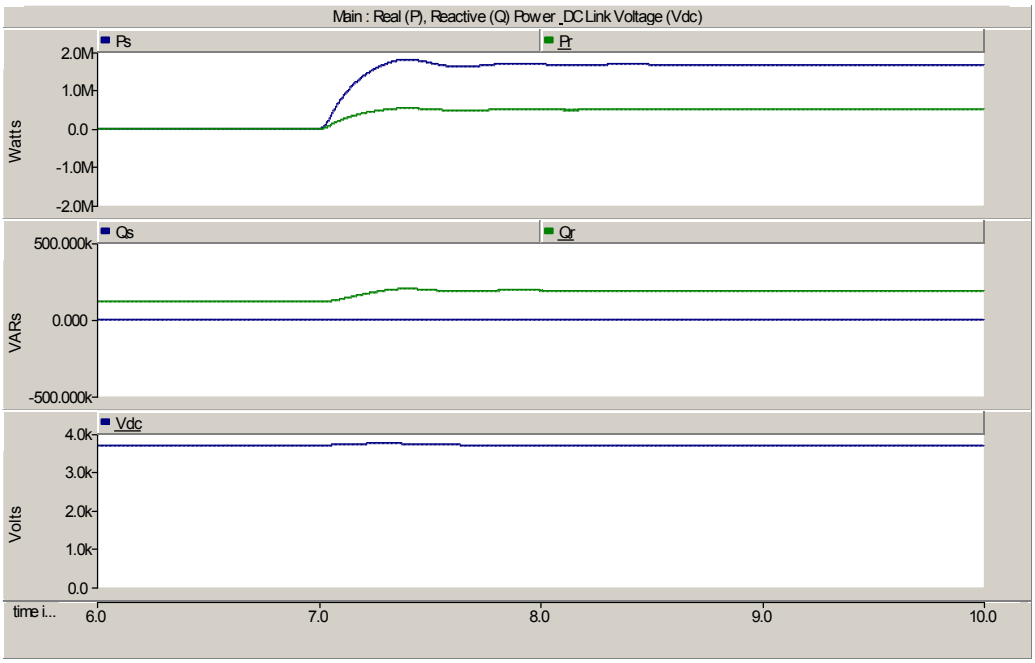

Figure 5.9. DGIG simulation at super-synchronous speed.

5.4. MULTIPLE REFERENCE FRAME SYNCHRONOUS ESTIMATOR (MRFSE)

Several power electronic converter control techniques are available that allow the designer to modify the control signal so that appropriate harmonics can be injected. However, these are normally based on an open-loop procedure that does not ensure that the desired operating point is achieved. In this section, multiple reference frame theory is used to formulate a synchronous estimator to ensure that harmonic contents are exactly tracked. In addition, the control technique is developed based on the estimator output to ensure that particular harmonics are eliminated from the system under consideration. This scheme has two parts, a multiple reference frame based estimator, which decomposes the measured grid currents to appropriate frames of reference, and an integral controller which forces the actual components to match their commands [27-28]. The proposed scheme is demonstrated using computer simulations.

The basis for the development of MRFSE is discussed in detail here. The phase variables f_a, f_b, and f_c, written in vector form as

$$f_{abc} = \left[f_a \; f_b \; f_c \right]^T \tag{65}$$

where f may represent a voltage or current. The component of these variables which is constant in a reference frame that rotates at 'x' times the fundamental frequency is defined as

$$f_{qd}^x = \left[f_q^x \; f_d^x \right]^T \tag{66}$$

The phase variable vector (65) may be approximately expressed in terms of the q- and d-axis variables as

$$f_{abc} = \sum_{x \in N} (K^x)^{-1} f_{qd}^x \tag{67}$$

where the rotational transformation, K^x, is given by

$$K^x = \frac{2}{3} \begin{bmatrix} \cos(x\theta_e) & \cos\left(x\left(\theta_e - \frac{2}{3} \right) \right) & \cos\left(x\left(\theta_e + \frac{2}{3} \right) \right) \\ \sin(x\theta_e) & \sin\left(x\left(\theta_e - \frac{2}{3} \right) \right) & \sin\left(x\left(\theta_e + \frac{2}{3} \right) \right) \end{bmatrix} \tag{68}$$

and where the pseudo inverse is defined as

$$\left(K^x \right)^{-1} \triangleq \frac{3}{2} \left(K^x \right)^T \tag{69}$$

In (67), N is the set of all reference frames considered, where each reference frame corresponds to exactly one harmonic present in the variable of (65). The set is formally defined as

$$N = \left\{\left\{3p+1\right\} \cup \left\{3q\right\} : P \in I, q \in N\right\} \cap \left\{r : i_{qd}^{r} \neq 0\right\} \tag{70}$$

where I is the set of integers, N is the et of natural numbers, and only non zero harmonics are considered as shown by the set on the right-hand side of the intersection. In (68), θ_e, is the electrical angle of the synchronous reference frame. The harmonics of interest in a balanced, symmetrical, power system are in the series $\{...-5,-2,1,4,7,...\}$. Since a wye-connected system is assumed, the triplen harmonics $\{3,6,9,...\}$ are zero. Notice that, for example, '-5' is considered and '5' is not since the 5th harmonic in a balanced symmetrical system exhibits a negative phase sequence.

The block diagram for MSRFE is depicted in Figure 5.10. In the block diagram α is the first reference frame considered and Ω is the last reference frame considered. Therein, it may be observed that the estimator consists of n branches , each of which estimates the current vector associated with one reference frame. The branches are interconnected in such a way that for any branch the estimated harmonics of all the other branches are subtracted from the measured current, $i_{abc.}$ In this way, the harmonic of interest to that branch becomes isolated in the steady state as the estimated currents from the other branches converge to the correct values. This is necessary since applying (68) directly to i_{abc} produces vector i_{qd}^{x} only as an average value. Vectors from reference frame other than 'x' contribute sinusoidally varying components to the average value and have amplitudes proportional to the magnitudes of the other harmonics. These sinusoidally varying components are difficult to filter since their amplitudes may be high compared with the average value of the signal. However, when the harmonic is isolated, utilizing the transformation K^{x} becomes effective since it extracts only i_{qd}^{x} and there are no sinusoidally varying components. Each branch then has an integral feedback loop that drives the estimated current exactly to the actual current in the steady-state.

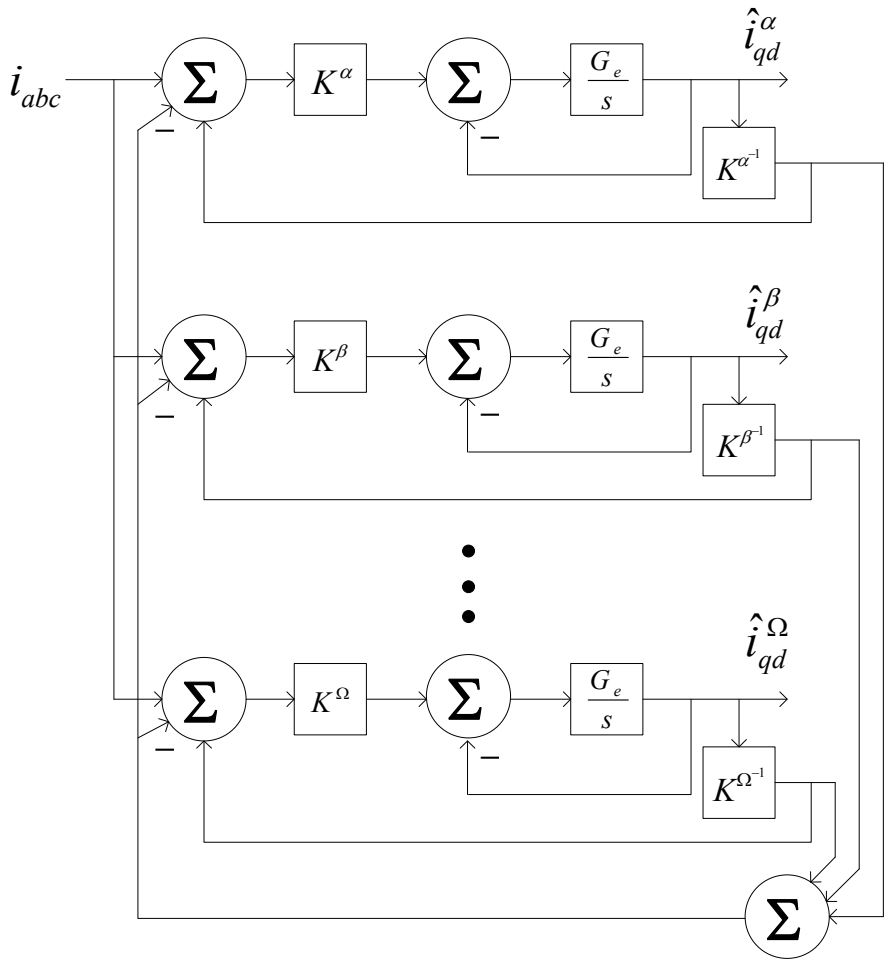

Figure 5.10. MRFSE estimator block diagram.

The mathematical justification of the estimator is given as

$$\frac{1}{G_e}\frac{d}{dt}\hat{i}_{qd}^{x} = K^{x}\left[i_{abc} + \left(K^{x}\right)^{-1}\hat{i}_{qd}^{x} - \sum_{m\in N}\left(K^{n}\right)^{-1}\hat{i}_{qd}^{m}\right] \tag{71}$$

Substituting equation (70) in above equation yields

$$\frac{d}{dt}\hat{i}_{qd}^{x} = G_e K^{x} \sum_{m\in N} \left(K^{m}\right)^{-1} \left[i_{qd}^{m} - \hat{i}_{qd}^{m}\right] \tag{72}$$

From which it will be shown that $i_{qd}^{x} \to \hat{i}_{qd}^{x}$ for all $x \in N$. First, let us assume that each i_{qd}^{x} is constant, since the objective here is to prove stability and convergence of the isolated estimator. As will be discussed later, this assumption does not restrict the use of the regulator to conditions in which each i_{qd}^{x} is constant. In practice it simply means that the estimator should be faster than the controller. Therefore, $\frac{d}{dt} i_{qd}^{x} = 0$ may be subtracted from the left side of (72).

$$\frac{d}{dt}\left[\hat{i}_{qd}^{x} - i_{qd}^{x}\right] = G_e K^{x} \sum_{m\in N} \left(K^{m}\right)^{-1} \left[i_{qd}^{m} - \hat{i}_{qd}^{m}\right] \tag{73}$$

If the error vectors are defined by $\Delta_{qd}^{x} = i_{qd}^{x} - \hat{i}_{qd}^{x}$ then (73) becomes

$$\left(K^{x}\right)^{-1} \frac{d}{dt} \Delta_{qd}^{x} = -G_e \sum_{m\in N} \left(K^{m}\right)^{-1} \Delta_{qd}^{m} \tag{74}$$

Since this equation is written for arbitrary '*x*', it may be written for each member of the set *N*. Adding all the *n* equation yields

$$\sum_{m\in N} \left(K^{m}\right)^{-1} \frac{d}{dt} \Delta_{qd}^{x} = -nG_e \sum_{m\in N} \left(K^{m}\right)^{-1} \Delta_{qd}^{m} \tag{75}$$

Each $\left(K^{x}\right)^{-1}$ is a sinusoidal function of θ_e. By considering multiple values of θ_e it can be seen that a solution of (75) must satisfy

$$\frac{d}{dt} \Delta_{qd}^{x} = -nG_e \Delta_{qd}^{x} \qquad \forall x \in N \tag{75}$$

The solution to this differential equation is a decaying exponential since $-nG_e$, is negative. Therefore, the error vectors, Δ_{qd}^{x}, approach zero exponentially as time increases. The conclusion is that with a constant input, the estimator output will converge to the correct value. Although constant current is assumed in this derivation, the estimator does not require that the physical variable to be constant in order to converge. It merely requires that the signal changes slowly with respect to the speed of the estimator.

5.5. MODIFIED CONTROLLER FOR GSC WITH ACTIVE FILTERING FEATURE

MRFSE is used to decompose the measured grid current to appropriate frames of reference as illustrated in Figure 5.11. Since the system is a three phase wye-connected balanced system the harmonics of interest are $6k\pm1$ where k is a natural number. The predominant harmonics of interest are 5th, 7th, 11th, and 13th.

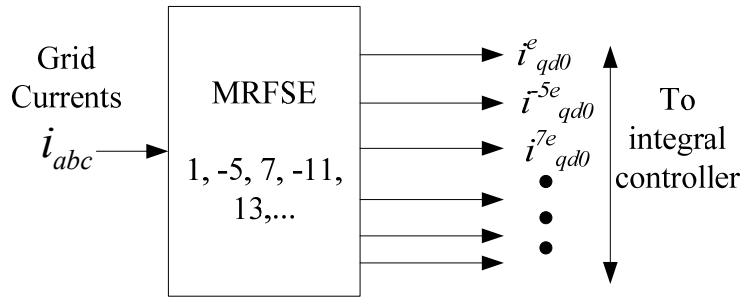

Figure 5.11. Output of MRFSE.

The output of the estimator is fed to the integral controller as shown in Figure 5.12. Each harmonic current has an individual controller loop to ensure that actual values track the commanded values.

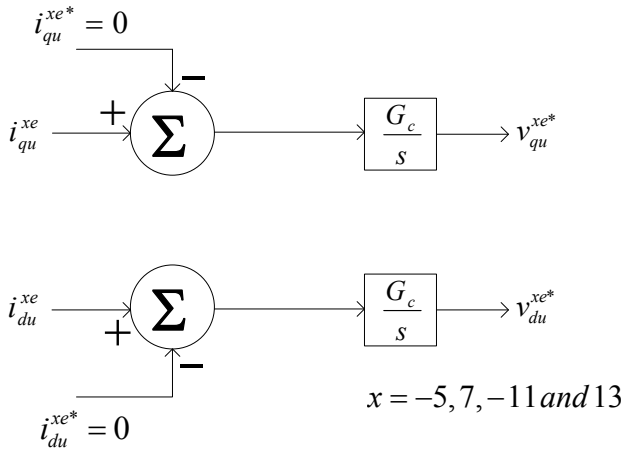

Figure 5.12. Integral controller for harmonic tracking

Finally the GSC control output and the integral controller outputs are transformed to abc frame and added as illustrated in Figure 5.13 to produce the commanded voltage signals for sine-triangle modulation control.

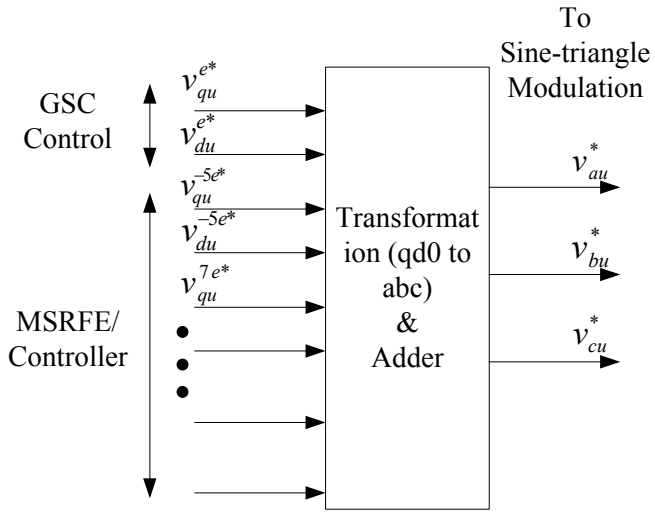

Figure 5.13. Schematic for producing the control signal

5.6. SIMULATION RESULTS WITH ACTIVE FILTERING FEATURE

The schematic in Figure 5.14 shows the DFIG wind turbine close to a non-linear load. The non-linear load is an uncontrolled diode rectifier supplying a RL ($R = 4\Omega \,\&\, L = 100\mu H$) load of 2.25 MW at 3000 V and 750 A. The non-linear load is assumed to be constant here as opposed to dynamically changing loads in an industry.

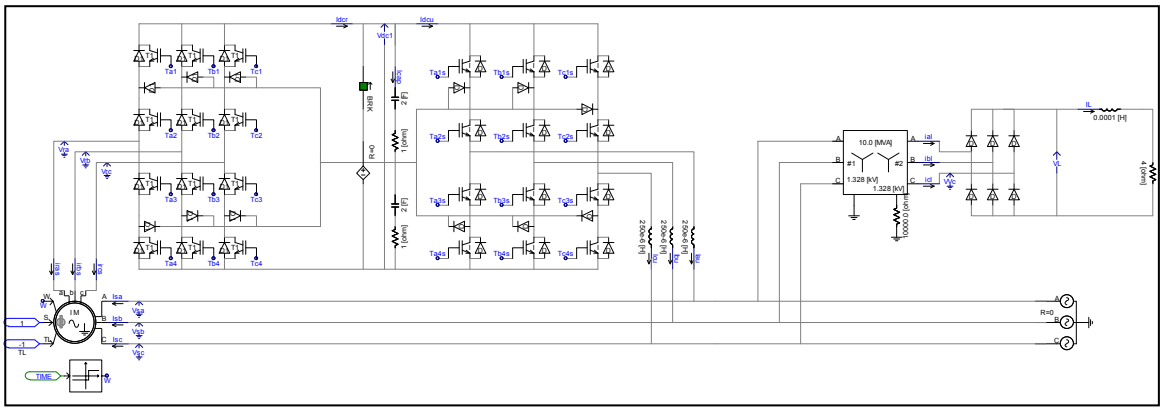

Figure 5.14. DFIG connected to a non-linear load.

The system illustrated in Figure 5.14 is simulated and analyzed using the MRFSE. Figure 5.15 shows the load currents and grid currents without active filtering feature. It can be seen that load currents are square waves as predicted and grid currents are distorted due to high content of $6k \pm 1$ harmonics. The total harmonic distortion (THD) in the grid currents was measured and found 16.7% considering only first 15 harmonics since they are dominant. As per IEEE standard 519 the THD of 16.7% is too high for the considered non-linear load. In this situation it is important for an industry to minimize the amount of harmonics absorbed from the power system. For this reason the concept of MRFSE is used in this thesis to analyze the selective harmonics.

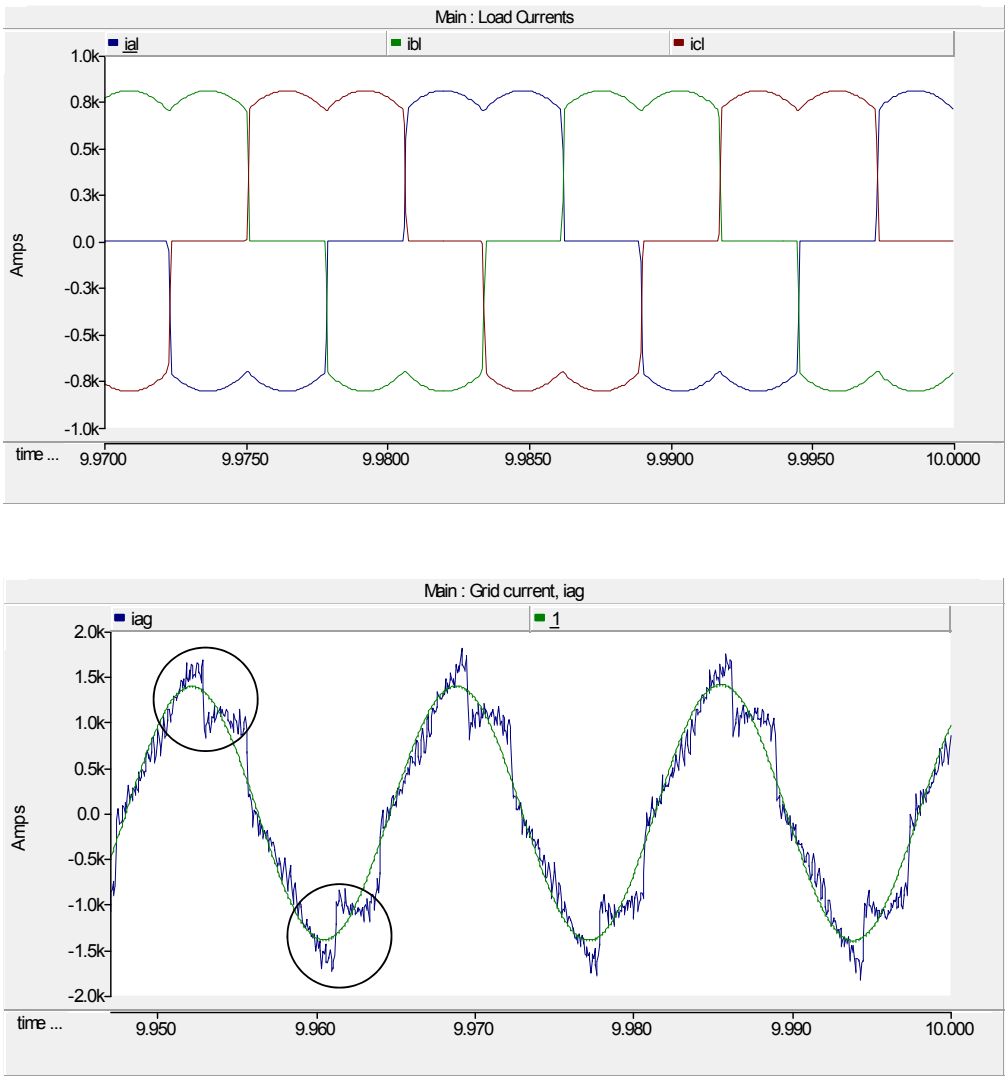

Figure 5.15. Load currents and grid currents without harmonic compensation.

The MRFSE illustrated in Figure 5.10 is used to analyze the system without harmonic compensation. The estimator is used to track only the important harmonics which includes 5^{th}, 7^{th}, 11^{th}, and 13^{th}. Figure 5.16 illustrates the harmonics in their appropriate frame of reference. It can be observed that estimator is able to track the dynamically changing $6k \pm 1$ harmonics.

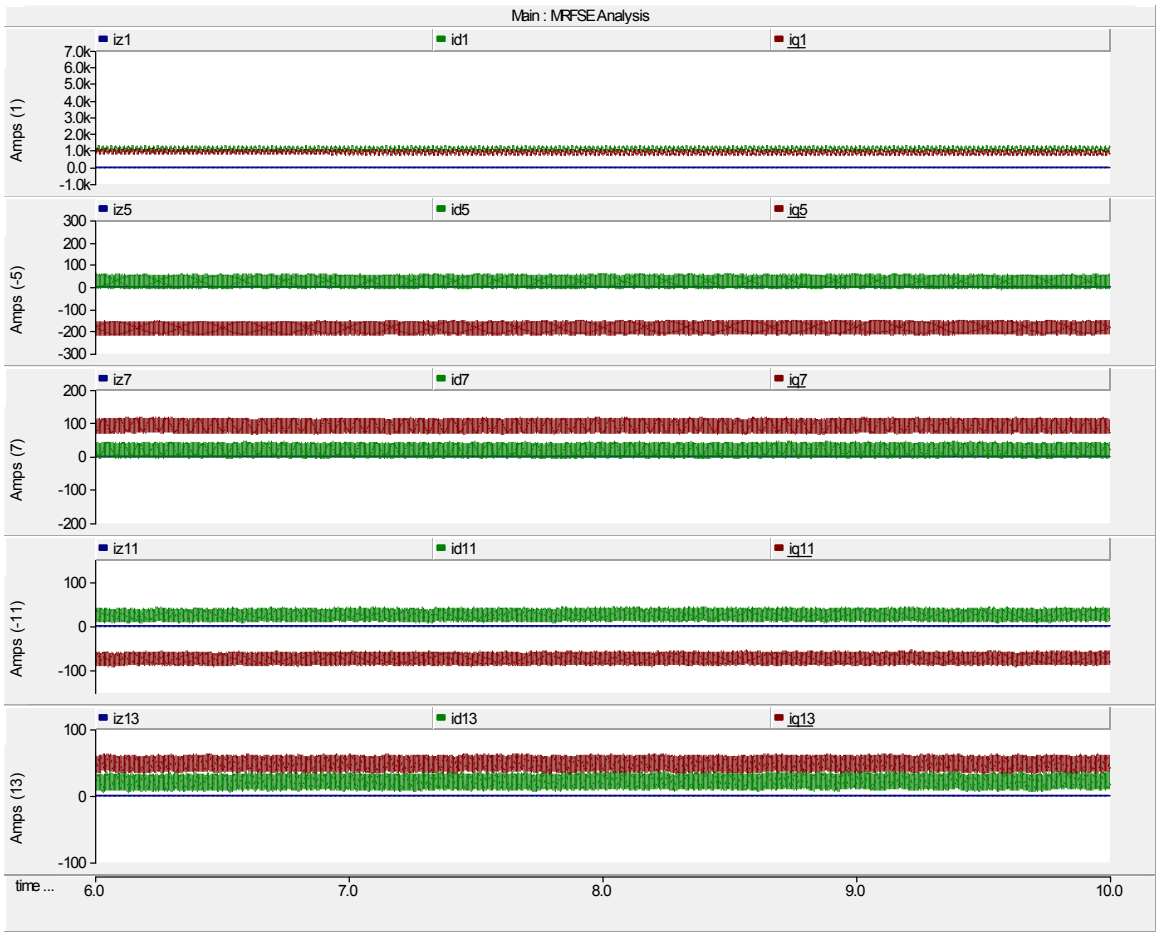

Figure 5.16. Harmonic analysis of the uncompensated system.

The controller illustrated in Figure 5.12 is implemented. The commanded value for each harmonic is specified as zero. The estimator gain is selected such that it is faster in performance as compared to the controller. Figure 5.17 illustrate the grid currents with harmonic compensation. The THD after eliminating the selected harmonics reduces down to 2.5% from 16.7%. Also Figure 5.18 illustrates the MSRFE analysis after the harmonic compensation. It can be observed from the analysis that all $6k \pm 1$ harmonics under consideration except the fundamental component are tracked and reduced to zero.

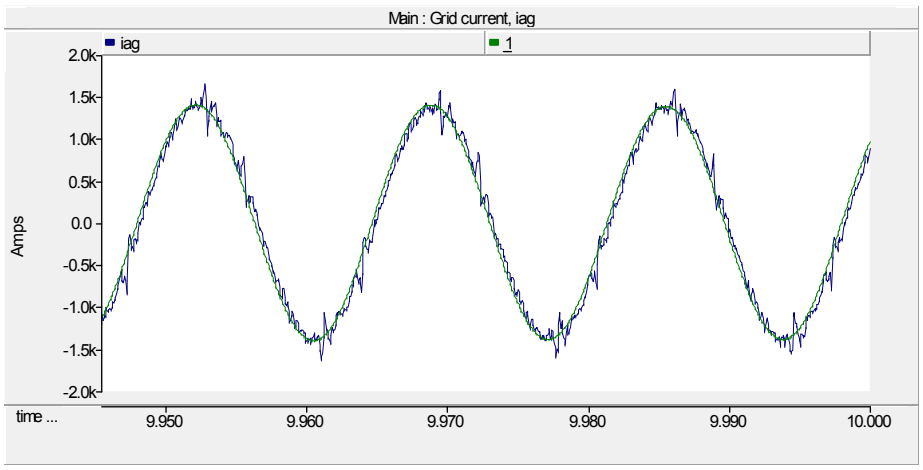

Figure 5.17. Grid currents with harmonic compensation

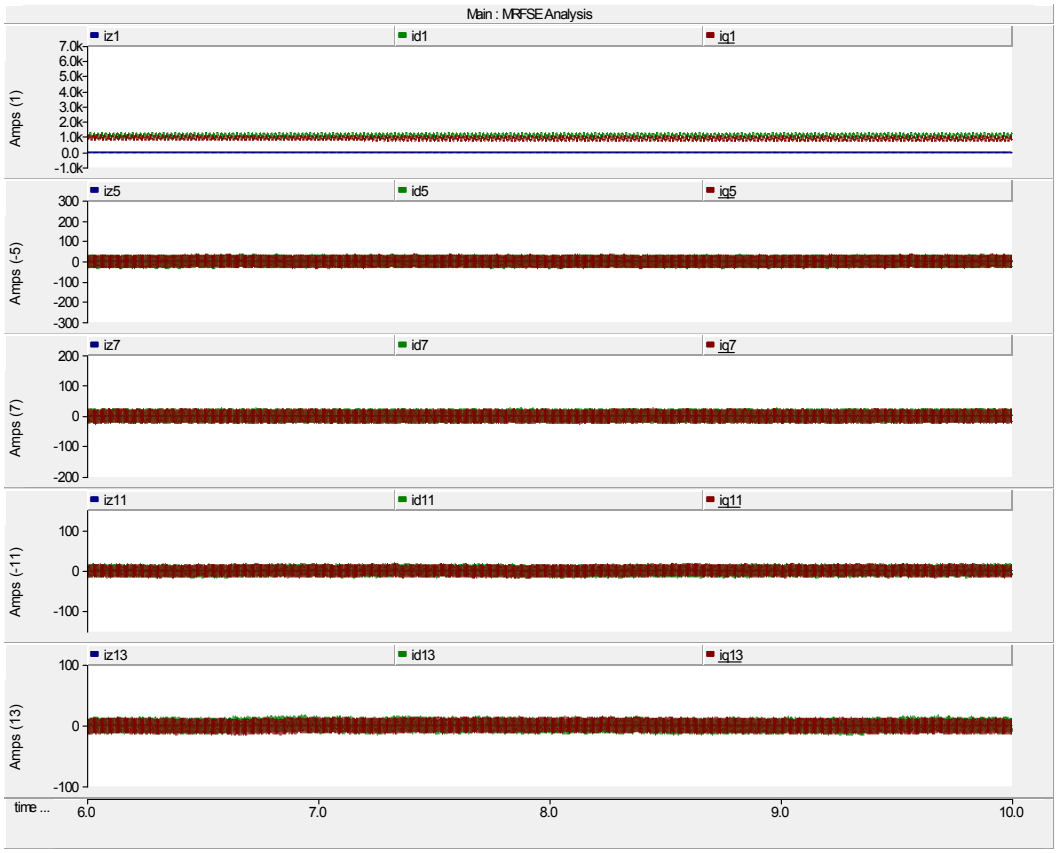

Figure 5.18. MRFSE analysis after harmonic compensation

A harmonic analysis is done as illustrated in Figure 5.19 to show that the MRFSE controller works well under different operating conditions. Table 5.1 shows the detail of the harmonic analysis under three different conditions of compensation. The first case is without compensation and so for this reason it has high total harmonic distortion (THD). The 2nd and 3rd case are with 5th, 7th and 5th, 7th, 11th, and 13th harmonic compensation respectively. Only first 15 harmonics are considered for the analysis.

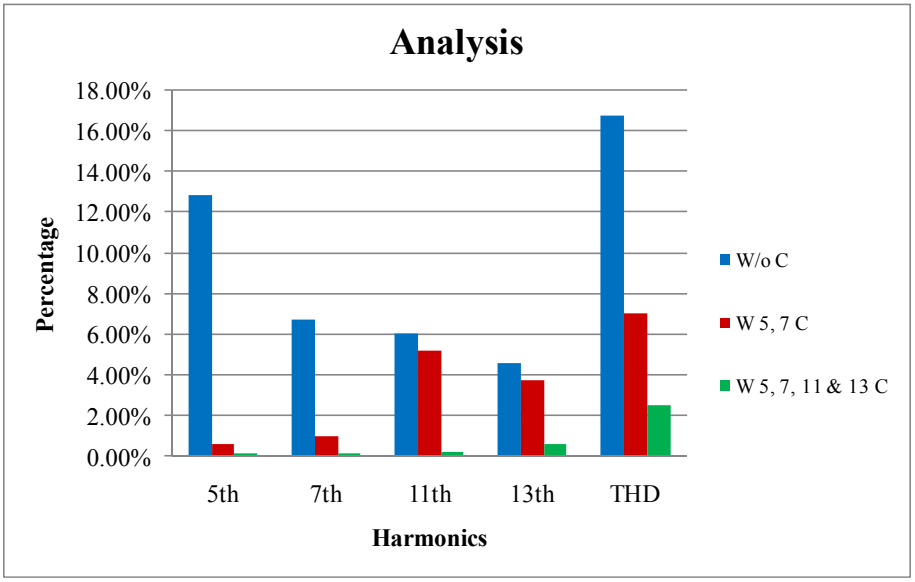

Figure 5.19. Harmonic analysis.

Table 5.1. Harmonic analysis.

Harmonics	Without Compensation	With 5th, 7th compensation	With 5th, 7th, 11th and 13th compensation
5th	12.81%	0.64%	0.14%
7th	6.70%	1.00%	0.18%
11th	6.05%	5.20%	0.21%
13th	4.61%	3.78%	0.64%
THD	17%	7.00%	2.50%

5.7. SUMMARY

First, a detailed model of DFIG was developed in PSCAD and simulated under different operating conditions to verify the correct operation. Then a non-linear load was added close to the DFIG system and harmonic current injection by the load was verified by the simulation results. MRFSE was used to analyze the harmonic injected by the load. The simulation results verify that the estimator is able to track the harmonics. Integral controller was developed to inject the harmonics using GSC and so the harmonics from the grid currents are eliminated. The simulation results verify the harmonic elimination from the grid currents.

Finally harmonic analysis details are shown to verify that the THD of the grid currents is reduced compared to the case where there is no compensation. The main advantage of the system is that it tracks the harmonics in real time and eliminates them dynamically. It also reduces the filtering impact on the DFIG system.

6. CONCLUSION

In this thesis the characteristics of different energy storage systems are compared with the requirements for the power system and renewable energy systems. ESS requirements for power systems and renewable systems are summarized in a tabular format. From the review done on various available energy storage systems in Section 2 it is clear that no energy storage is able to suffice all power system requirements. Combining two or more storage systems with complimentary feature turns out to be a good solution.

The DFIG model is developed using software package Matlab/Simulink. The characteristics of DFIG are studied by performing different tests on the machine model. The result of the test helps in determining the control for the integrated energy storage scheme. The per-unit model of the wind turbine is also discussed in Section 3.

In Section 4 the developed model of a DFIG system is simulated for a realistic wind scenario. The results verify that the changes in the wind speed causes fluctuation in the output power of the wind turbine generator system. A new scheme with integrated ultra-capacitor energy storage system is defined in which the UC in series with a bi-directional dc-dc buck-boast converter is placed in between the RSC and DC link. The control scheme and different operational modes of the new scheme are discussed in detail. The simulations are carried out for the same real life wind scenario. The simulation results verify the correct operation of the new scheme. The new scheme is successful in reducing the output power fluctuations as well as it can also be used for load/power shifting. The duration of the load shifting depends on the size of the energy storage. Further research is required in this area to find the correct sizing of the energy storage system. Finally, the simulation results were compared with the existing topologies with integrated energy storage system. It was concluded that the amount of losses occurring in the bi-directional dc-dc converter can be eliminated by placing the energy storage in series with the RSC and DC link.

The simulation results also verify that the adding of the energy storage system not only reduces the fluctuations in output power but also provides reliability to the power

system grid by providing more time for the spinning reserves to start during sudden reduction in the wind speed.

The detailed model of the DFIG system is simulated in PSCAD with active filtering feature using MRFSE/Controller in Section 5. MRFSE decomposes the fundamental component in the required frames of reference and so only $6k\pm1$ harmonics are tracked to reduce the filtering impact on the GSC of DFIG. Also by using the GSC the injection of high frequency currents in the stator and rotor is eliminated. The MRFSE tracks the dynamic harmonics in the grid current due to the non-linear load and integral controller starts injecting harmonics using the GSC. This reduces the pollution in the grid currents. The GSC does dual function of active rectifier by charging the dc link capacitor as well as active filter by injecting harmonics required by the nearby non linear loads. The simulation results verify the correct operation of the estimator and controller. The harmonic analysis done on the system also verifies that the controller is successful in reducing the harmonics from the power system network. Thus the DFIG does not only act as source of real and reactive power but also as power conditioner by supplying the harmonics required by the non-linear load.

APPENDIX

Ultra-Capacitor Sizing for Wind Turbine Applications

From (59-60) we can write,

$$P_{wind} \propto v_{wind}^3$$

If at time, $t = 0$ instant the wind velocity drops to zero then the output wind power will also drop down to zero. Figure 1A illustrates this condition. The ultra-capacitor can be sized depending upon how long the power system takes to stabilize itself.

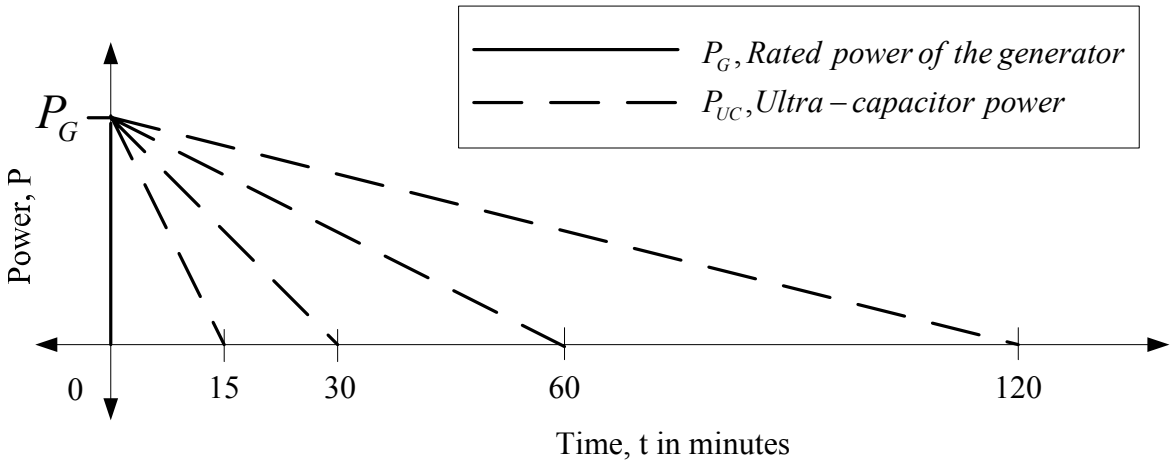

Figure A.1. Sizing of ultra-capacitor for wind application

Here, if *t* is the time for which ultra-capacitor is suppose to provide support, then the energy required from ultra-capacitor is given by,

$$E_1 = \frac{1}{2}.P_G.t$$

The total energy required from ultra-capacitor is given by,

$$E_{total} = E_1 + E_2$$

where,

$$E_2 = \frac{1}{2}.C.V_{\min}^2$$

Here, $V_{\min}$ is the minimum voltage required by the rotor side converter. Now, the size of the ultra-capacitor can be found from,

$$E_{total} = \frac{1}{2}.C.V_{dc}^2$$

Here, V_{dc} is the dc-link voltage. Similar calculation was performed for the system studied in this thesis and to hold for 20 *mins* the ultra-capacitor value required was 3.6 Farads.

For the energy storage, Maxwell ultra-capacitor for wind application is considered in this thesis. Maxwell ultra-capacitor is rated at 94 F, 75 Volts. So the number of capacitors required to support the system for 20 *mins* are given by,

$$No.s\,of\,ultra-capacitor = \frac{3700}{75} \approx 50$$

$$Capacitor\,value = \frac{94}{50} \approx 1.8\,F$$

So two legs in parallel, each made up of 50 capacitors in series are required for the system under consideration.

BIBLIOGRAPHY

[1] WWEA, "World wind energy report 2009," WWEA, Bonn, GermanyMarch 2010.

[2] DOE, "20% Wind Energy by 2030 - Increasing Wind Energy's contribution to U.S. Electricity Supply " July 2008.

[3] T. Ackermann, *Wind Power in Power Systems*: John Wiley and Sons Ltd January 2005.

[4] R. Pena*, et al.*, "Doubly fed induction generator using back-to-back PWM converters and its application to variable-speed wind-energy generation," *Electric Power Applications, IEE Proceedings,* vol. 143, pp. 231-241, 1996.

[5] Q. Liyan and Q. Wei, "Constant Power Control and Fault-Ride-Through Enhancement of DFIG Wind Turbines with Energy Storage," in *Industry Applications Society Annual Meeting, 2009. IAS 2009. IEEE*, 2009, pp. 1-8.

[6] J. Zhenhua and Y. Xunwei, "Modeling and control of an integrated wind power generation and energy storage system," in *Power & Energy Society General Meeting, 2009. PES '09. IEEE*, 2009, pp. 1-8.

[7] M. Aktarujjaman*, et al.*, "Control Dynamics of a doubly fed induction generator under sub- and super-synchronous modes of operation," in *Power and Energy Society General Meeting - Conversion and Delivery of Electrical Energy in the 21st Century, 2008 IEEE*, 2008, pp. 1-9.

[8] L. Haihua*, et al.*, "Modeling and control of DFIG based wind turbine/storage system in islanded operation," in *Sustainable Power Generation and Supply, 2009. SUPERGEN '09. International Conference on*, 2009, pp. 1-6.

[9] M. Marinelli*, et al.*, "Modeling of DFIG Wind Turbine and Lithium Ion Energy Storage System," in *Complexity in Engineering, 2010. COMPENG '10.*, 2010, pp. 43-45.

[10] M. T. Abolhassani*, et al.*, "A sensorless integrated doubly-fed electric alternator/active filter (IDEA) for variable speed wind energy system," in *Industry Applications Conference, 2003. 38th IAS Annual Meeting. Conference Record of the*, 2003, pp. 507-514 vol.1.

[11] E. Tremblay*, et al.*, "Grid-side converter control of DFIG wind turbines to enhance power quality of distribution network," in *Power Engineering Society General Meeting, 2006. IEEE*, 2006, p. 6 pp.

[12] A. Gaillard, *et al.*, "Active filtering capability of WECS with DFIG for grid power quality improvement," in *Industrial Electronics, 2008. ISIE 2008. IEEE International Symposium on*, 2008, pp. 2365-2370.

[13] R. I. Bojoi, *et al.*, "Current control strategy for power conditioners using sinusoidal signal integrators in synchronous reference frame," *Power Electronics, IEEE Transactions on,* vol. 20, pp. 1402-1412, 2005.

[14] P. J. Binduhewa, *et al.*, "Ultracapacitor energy storage for MicroGrid micro-generation," in *Power Electronics, Machines and Drives, 2008. PEMD 2008. 4th IET Conference on*, 2008, pp. 270-274.

[15] L. Wei and G. Joos, "Comparison of Energy Storage System Technologies and Configurations in a Wind Farm," in *Power Electronics Specialists Conference, 2007. PESC 2007. IEEE*, 2007, pp. 1280-1285.

[16] E. Spahic, *et al.*, "Wind Energy Storages - Possibilities," in *Power Tech, 2007 IEEE Lausanne*, 2007, pp. 615-620.

[17] J. D. Boyes and N. H. Clark, "Technologies for energy storage. Flywheels and super conducting magnetic energy storage," in *Power Engineering Society Summer Meeting, 2000. IEEE*, 2000, pp. 1548-1550 vol. 3.

[18] S. S. Choi, *et al.*, "Energy storage systems in distributed generation schemes," in *Power and Energy Society General Meeting - Conversion and Delivery of Electrical Energy in the 21st Century, 2008 IEEE*, 2008, pp. 1-8.

[19] S. C. Smith, *et al.*, "Advancement of energy storage devices and applications in electrical power system," in *Power and Energy Society General Meeting - Conversion and Delivery of Electrical Energy in the 21st Century, 2008 IEEE*, 2008, pp. 1-8.

[20] J. P. Barton and D. G. Infield, "Energy storage and its use with intermittent renewable energy," *Energy Conversion, IEEE Transactions on,* vol. 19, pp. 441-448, 2004.

[21] T. Siostrzonek, *et al.*, "Energy storage systems the flywheel energy storage," in *Power Electronics and Motion Control Conference, 2008. EPE-PEMC 2008. 13th*, 2008, pp. 1779-1783.

[22] T. Ise, *et al.*, "A hybrid energy storage with a SMES and secondary battery," *Applied Superconductivity, IEEE Transactions on,* vol. 15, pp. 1915-1918, 2005.

[23] P. F. Ribeiro, *et al.*, "Energy storage systems for advanced power applications," *Proceedings of the IEEE,* vol. 89, pp. 1744-1756, 2001.

[24] M. Lafoz*, et al.*, "Energy Management in solar photovoltaic plants based on ESS," in *Power Electronics and Motion Control Conference, 2008. EPE-PEMC 2008. 13th*, 2008, pp. 2481-2486.

[25] K. Strunz and E. K. Brock, "Hybrid plant of renewable stochastic source and multilevel storage for emission-free deterministic power generation," in *Quality and Security of Electric Power Delivery Systems, 2003. CIGRE/PES 2003. CIGRE/IEEE PES International Symposium*, 2003, pp. 214-218.

[26] P. C. Krause*, et al.*, *Analysis of Electric Machinery and Drive Systems*, 2 ed.: John Wiley & Sons, 2002.

[27] P. C. Krause and C. H. Thomas, "Simulation of Symmetrical Induction Machinery," *Power Apparatus and Systems, IEEE Transactions on,* vol. 84, pp. 1038-1053, 1965.

[28] Q. Wei*, et al.*, "Real-Time Implementation of a STATCOM on a Wind Farm Equipped With Doubly Fed Induction Generators," *Industry Applications, IEEE Transactions on,* vol. 45, pp. 98-107, 2009.

[29] S. Heier, *Grid Integration of Wind Energy Conversion Systems*: John Wiley & Sons Ltd, 1998.

[30] P. L. Chapman and S. D. Sudhoff, "A multiple reference frame synchronous estimator/regulator," *IEEE Transactions on Energy Conversion,* vol. 15, pp. 197-202, 2000.

[31] S. J. Lee and S. K. Sul, "A harmonic reference frame based current controller for active filter," in *Applied Power Electronics Conference and Exposition, 2000. APEC 2000. Fifteenth Annual IEEE*, 2000, pp. 1073-1078 vol.2.

[32] EPRI-DOE Handbook of Energy Storage for Transmission and Distribution Applications, Reference 1001834, December 2003. Available from www.epri.com.

[33] S. M. Schoenung, *Characteristics and Technologies for Long-vs. Short Term Energy Storage, SAND2001-0765, March 2001*, Sandia National Laboratories, Albuquerque, NM, USA.

[34] S. M. Schoenung and W. Hassenzahl "Long vs. short-term energy storage: sensitivity analysis," SAND2007-4253 July 2007 July 2007 Sandia National Laboratories, Albuquerque, NM, USA.

[35] K. Strunz, "Computer system design analogies for synthesis of sustainable distributed generation systems," *CIGRE Symposium on Power Systems with Dispersed Generation*, Athens, Greece, April 2005.

[36] M. T. Abolhassani, *et al.*, "An electromechanical active harmonic filter," in *Electric Machines and Drives Conference, 2001. IEMDC 2001. IEEE International*, 2001, pp. 349-355.

[37] Q. Wei, *et al.*, "Real-Time Implementation of a STATCOM on a Wind Farm Equipped with Doubly Fed Induction Generators," in *Industry Applications Conference, 2006. 41st IAS Annual Meeting. Conference Record of the 2006 IEEE*, 2006, pp. 1073-1080.

VITA

Nishant Swaraj Chouhan was born on August 7th, 1984. He obtained his B.E. degree in Electrical Engineering from Maharaja Sayajirao University of Baroda (M. S. University) in October 2006. From July 2006 to July 2008 he worked in the Automation and Drives (A&D) Division, Siemens as an Executive Engineer, Technical Support-Marketing. He received his Master of Science degree in Electrical Engineering from Missouri University of Science & Technology in December of 2010. His research interests include Electric Machine Analysis, Electric Drives, Power Electronics Applications in Power Systems and Renewable Energy Systems.